4.1.4 FT-Rheology at low strain amplitudes and extension of van Gurp-Palmen method

For strain sweeps conducted at low γ_0, one can conclude that the measured $\Phi_3(\gamma_0)$ remains stable for low strain amplitudes. The relative phase Φ_3 at low strain amplitudes is sensitive to the presence of LCB. For γ_0 = 0.5, the noise level is still low enough for an accurate detection and quantification of non-linearity. This happens despite the fact that the measurement is performed approximately in the linear regime, if it is defined as the regime where G' and G'' are not yet affected beyond the reproducibility of rheological measurements, e.g. less than 10% change in moduli values. In this work we consider the measurement to be performed in the linear regime when $I_{3/1} < 1\%$. It is worth mentionning that purely linear rheology is an approximation, albeit highly accurate and in fact, materials will always respond in a non-linear fashion. FT-Rheology offers the advantage to quantify the occurring non-linearity at an early stage.

As seen in strain sweep measurements, in most cases $\Phi_3(\gamma_0)$ for polyethylenes reaches a plateau value of 150° -170° at high γ_0 when strain sweeps are preformed, as illustrated in fig. 4.6-4.10. This could suggest that Φ_3 is more appropriate for differentiating topologies at small strain amplitudes, e.g. $\gamma_0 < 1$. Furthermore, $\Phi_3(\gamma_0)$ levels off for $0.5 < \gamma_0 < 1$, where γ_0 = 0.5 is the lowest strain amplitude for which our optimised setup can still quantify reproducible non-linearities for the specific samples. Taking advantage of this lower plateau value Φ_3 measured at low strain is extrapolated to zero strain amplitude. In this limit Φ_3^0 ($lim_{\gamma_0 \to 0} \Phi_3 = \Phi_3^0$) can be an effective quantity for "fingerprinting" LCB.

The van Gurp-Palmen method consists of performing a frequency sweep in the linear regime and plotting δ (strain -stress phase lag in linear rheological regime) against the magnitude of the complex modulus, $\mid G^*(\omega) \mid$, normalized to the plateau modulus, G_N^0 [Trinkle 02]. This method is extended to include the non-linear information and the phase of the third harmonic at vanishing strain amplitude, Φ_3^0. Measurements are performed with the ARES rheometer, for a range of complex modulus $\mid G^* \mid$, and are displayed in fig. 4.16. When Φ_3^0 is plotted against $\mid G^*(\omega) \mid / G_N^0$, there is a clear discrimination between linear polyethylenes and LCB. Linear polyethylenes exhibit a Φ_3^0 lower than LCB for $\mid G^*(\omega) \mid / G_N^0$ up to 0.1. For higher moduli (or higher excitation frequencies) linear samples can exhibit a higher Φ_3^0. The same trends are shown also for samples of higher polydispersity (*PDI* of 5-8), in fig. 4.17. The measured Φ_3^0 plotted against Deborah number is displayed in fig. 4.18. Within this chapter, the Deborah number is defined as $De = \omega \lambda_T$, where ω is the angular frequency and λ_T is the characteristic relaxation time, defined by the lowest frequency where tan δ = 1. This characteristic time corresponds to the lowest inverse frequency ω_c where tan δ = 1, referred to as τ_d in chapter 1. The results are found to be reproducible (= $\pm$ 10°) for all sets of linear and branched samples.

Due to the importance of detecting LCB in PE, it is worth identifying the experimental conditions to obtain a maximum contrast between linear and LCB polyethylene towards the LAOS response. Long-chain branched polyethylenes present higher non-linearities for fre-

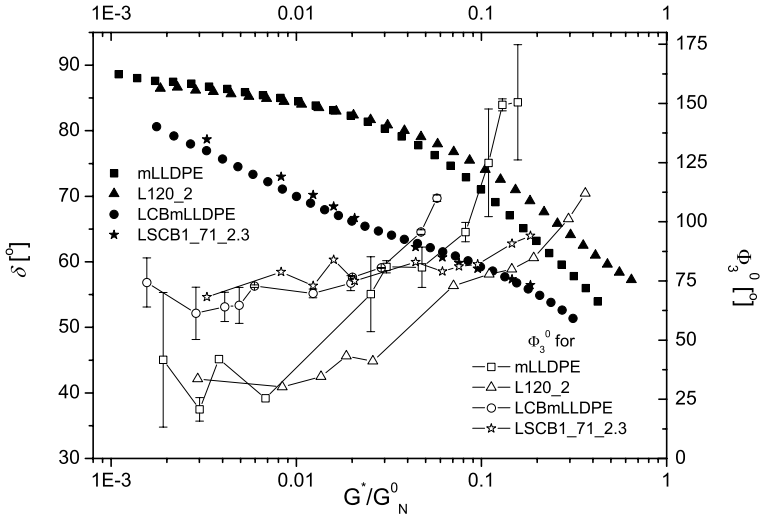

Figure 4.16: *Extended van Gurp-Palmen plot. Phase lag δ and zero-shear relative phase of 3rd harmonic, Φ_3^0, as a function of complex modulus normalized to plateau modulus, $|\ G^*\ |/G_N^0$, for LCB and linear polyethylenes of samples with PDI ≈ 2. G_N^0 values used: for mLLDPE 0.60 MPa, for L120_2 0.54 MPa, for LCBmLLDPE 0.59 MPa and for LSCB1_71_2.3 0.37 MPa.*

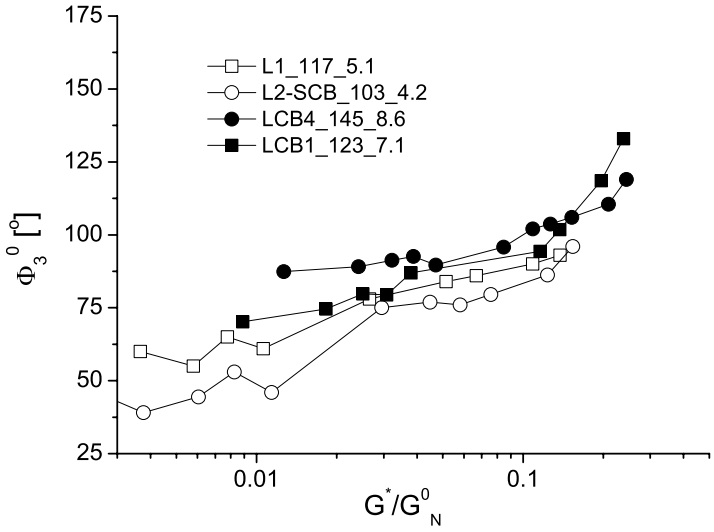

Figure 4.17: *Φ_3^0 as a function of complex modulus normalized by plateau modulus $|\ G^*\ |/G_N^0$, at T = 180 °C, for polyethylenes with PDI ≈ 5-8. G_N^0 values used: for L1_117_5.1 0.31 MPa, for L2-SCB_103_4.2 0.44 MPa, for LCB4_145_8.6 0.3 MPa and for LCB1_123_7.1 0.25MPa.*

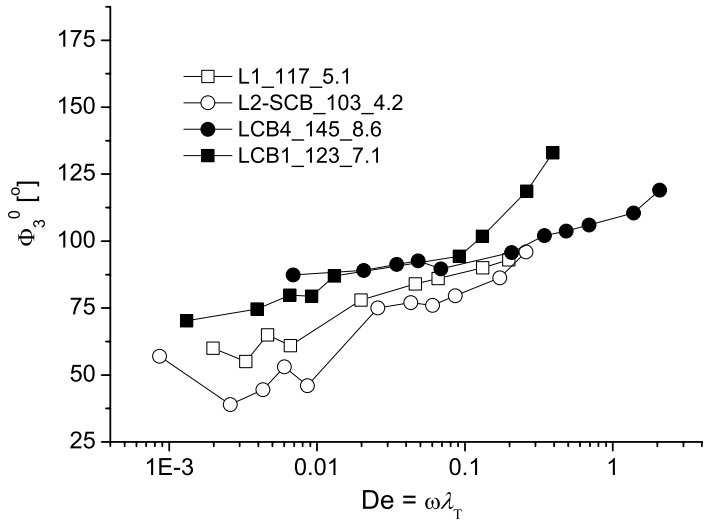

Figure 4.18: Φ_3^0 *at T = 180 °C versus Deborah number (*$De = \omega\lambda_T$*), for linear and LCB PE with PDI* $\approx$ *5-8.*

quencies and temperatures corresponding to the terminal zone of the linear spectrum as can be seen in fig. 4.19. This is also confirmed by measuring branched and linear samples at different tan δ. Results for two samples are presented in fig. 4.20. For increasing tan δ the $I_{3/1}$ of the LCB polyethylene exceeds that of the linear polymer and the difference between $I_{3/1,LCB}$ and $I_{3/1,linear}$ is larger.

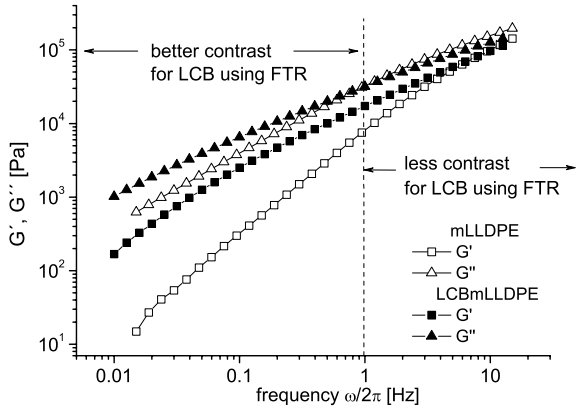

Figure 4.19: *Storage and loss moduli, G′ and G″ from dynamic mechanical measurement at T = 180 °C, for linear and branched polyethylenes, mLLDPE and LCBmLLDPE.*

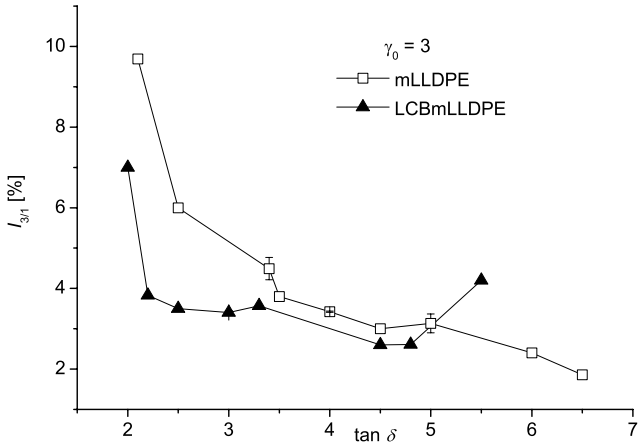

Figure 4.20: *$I_{3/1}$ for mLLDPE and LCBmLLDPE, γ_0 = 3, at different tan δ in the linear regime. Measurements performed with the RPA2000 rheometer.*

4.1.5 Influence of molecular weight and molecular weight distribution

It is well known that molecular weight and molecular weight distribution have a strong influence in the rheological properties of PE. According to Vega et al. [Vega 98] and Wood-Adams and Dealy [Wood-Adams 00], the effects of LCB on the rheological response can be masked by polydispersity and molecular weight. This statement is also true for the non-linear regime and the measured non-linearities via FT-Rheology, as already seen in chapter 3. Thus, it is crucial to separate the effects of an increased M_w and *PDI* from that of an increasing LCB content, with respect to $I_{3/1}$ and Φ_3.

Analyzing the non-linear behaviour of the linear and SCB samples, it is clear that higher M_w leads to higher non-linearity. It can also be seen that a broader molecular weight distribution (as quantified by *PDI*) leads also to an increased $I_{3/1}(\gamma_0)$ and $\Phi_3(\gamma_0)$. From eq. 4.2 with parameters M_w and *PDI* and assuming linear topology, $I_{3/1}(\gamma_0)$ can be predicted for all linear samples. The validity of this approach is demonstrated by the prediction of $I_{3/1}(\gamma_0)$ for two polydisperse linear polyethylenes (fig. 4.14).

When branching topology is introduced as a variable, the separation of the contributions of high molecular weight species and LCB structures in the non-linear behaviour becomes complicated. In order to overcome this, the samples are sorted and compared according to their *PDI* and M_w. Results show a predictable effect of M_w in the development of non-linearities (fig. 4.6-4.10). When the molecular weight and the distribution is known (i.e. M_w, *PDI*) and comparable for a set of investigated samples, LCB leads to an additional increase of $I_{3/1}(\gamma_0)$ and $\Phi_3(\gamma_0)$ at low frequencies (fig. 4.11, 4.12). The extended van Gurp-Palmen plot including Φ_3^0 can be used as another method to isolate the influences of LCB and molecular weight distribution (fig. 4.16 - 4.18). It must be noted that the experimental setup of the

RPA2000 allows reliable LAOS measurements of high molecular weight samples (up to M_w = 234 kg/mol with PDI up to ∼20 in our case) at large γ_0 where normal forces are prominent. The ability to minimize the effect of the resulting normal forces with the closed cavity in the RPA rheometer has a significant impact on the applicability of this method to high molecular weight materials.

4.1.6 Detection of LCB and correlation between NMR and FT-Rheology

The "fingerprinting" and characterization of LCB polyethylenes is a challenge which requires information obtained from several techniques and methods. For this reason, FT-Rheology results are correlated with ^{13}C melt-state NMR measurements. However, if the investigated polymer contains short-chain branches incorporated as comonomer, or formed by the catalyst, NMR may overestimate the degree of LCB. This is due to the fact that SCB of more than 6 carbons and LCB may not be distinguished in the resulting NMR spectra and their intensity sums up. Due to this inability of NMR to estimate whether a side-branch of more than 6 carbons is short ($M_{branch} < M_e$) or long ($M_{branch} > M_e$), the values obtained are related to the maximum possible degree of LCB only. This is illustrated by sample LSCB1_71_2.3 with 18.9 LCB/1000 CH_2. It is short-chain branched because of the presence of co-octene and the actual number of LCB could be significantly lower (see fig. 4.13). Another example involves samples with the same measured LCB/1000 CH_2 content (i.e. LCB2_234_15.6 and LCB3_199_19) which present different non-linear behaviour, as shown also in fig. 4.13. They have various low amounts of branching with more than 6 carbons. Thus, the actual LCB/1000 CH_2 may differ between them.

An additional parameter is the distribution and variation of branching in a LCB polyethylene, which cannot be directly measured with melt-state NMR or rheology. It is one of the key factors in the rheological behaviour [Lohse 02] and gives an additional possible explanation to differences in $I_{3/1}$ and Φ_3 observed between polyethylenes with the same measured LCB/1000 CH_2 content. Another example is L2-SCB_103_4.2 which has no rheologically detected LCB, but via NMR is found to have a high degree of co-butene incorporation (SCB). However, whether the comonomer affects the chemical reaction of LCB formation in the system is under discussion [Stadler 05].

Long-chain branching increases the non-linearity, as quantified by $I_{3/1}$ and Φ_3. However, for a branching level above a specific LCB/1000 CH_2 we can expect that non-linearities are decreasing. This could follow the behaviour described theoretically [Bersted 85] and experimentally [Vega 98, Vega 99] for the case of zero-shear viscosity. For LCB contents above a specific level, the effect from the decrease in radius of gyration becomes dominant and the side-arms act as plasticizers. In a similar way, a maximum in the non-linear behaviour for a LCB level can be observed experimentally, beyond which $I_{3/1}$ decreases. This can therefore be explained as the result from the above competing factors. It is possible that

polyethylenes of $M_w \approx 100$ kg/mol with an average LCB higher than 0.8 LCB/1000 CH_2 can exhibit a less pronounced non-linear behaviour. A similar observation is concluded for higher molecular weight LCB materials ($M_w \approx 200$ kg/mol) for an average degree of 0.5 LCB/1000 CH_2.

4.1.7 Optimized LAOS measurement conditions for differentiating LCB

Schlatter et al. [Schlatter 05] performed LAOS at constant Deborah numbers, using extremely low frequencies (ω_1 = 0.193 rad/s or $\omega_1\lambda_c$ = 0.07, where λ_c = 1/ω_c and ω_c was defined as the frequency for which the Cole-Cole diagram reaches a maximum) and at a temperature of 150 °C using solely an ARES rheometer. An open-rim cone-plate geometry was utilized, with a maximum strain amplitude of γ_0 = 4. Within this thesis, it is shown that $I_{3/1}$ of LCB polyethylenes deviates strongly from the one measured for linear and SCB samples, at strain amplitudes $3 < \gamma_0 < 7$. Above these deformations, the differences in $I_{3/1}(\gamma_0)$ and $\Phi_3(\gamma_0)$ of different topologies are not always significant (e.g. fig 4.12). For $\gamma_0 < 3$, the RPA2000 is not sensitive towards the detection of the higher harmonics, especially for low molecular weight samples. With the use of the ARES open-rim geometry, there are stability issues originating from the open plate geometry and the increasing normal forces, especially at $\gamma_0 > 2$ and $\omega_1/2\pi$ = 0.1 Hz. Within this work, we apply a strain amplitude $0.5 < \gamma_0 < 10$ by combining results from both rheometers, at two temperatures 140 °C and 180 °C, with the frequency varying between 0.01 Hz and 5 Hz, to obtain an optimised contrast between linear and LCB polyethylenes.

The zero-shear phase of the third harmonic, Φ_3^0, deduced from measurement of non-linearities at low strain amplitudes is another promising method to discriminate LCB from linear polyethylenes. This particular phase analysis is applied to compare samples of different topology separating the effect of LCB from that of molecular weight distribution on the rheological behaviour. This "fingerprint" of linear and LCB-polyethylenes can be easily presented by extending the van Gurp-Palmen plot to include the non-linear rheological behaviour (fig. 4.16, 4.17, 4.18).

Results shown in fig. 4.15 - 4.18 suggest that low frequencies are more appropriate for discriminating the non-linear rheological behaviour of LCB and linear polyethylenes. Large amplitudes are needed for a better discrimination between linear and branched polyethylenes on the basis of $I_{3/1}$. Considering all the above factors, a strain amplitude γ_0 = 2 - 4 and a typical frequency of $\omega_1/2\pi$= 0.1 Hz at 180 °C, are currently seen as the best empirical conditions towards the differentiation between LCB and linear polyethylenes using FT-Rheology.

The presented results in fig. 4.16, 4.17, 4.18 are in agreement with those shown in fig. 4.15, and suggest that the effect of LCB is more pronounced in the terminal zone (high tan δ). This can be understood if one considers that the characteristic time of the measurement should be such that the effects of branches of a macromolecule are probed. When LAOS is

applied at frequencies $\omega_1 > \omega_c$ (equivalently at low tan δ), the investigated length scale can be smaller than the distance between branches of the polyethylene macromolecules. LCB non-linearities increase with increasing tan δ. At higher tan δ values, the $I_{3/1}$ and Φ_3 curves for linear and LCB exhibit a crossover point. For tan δ larger than the crossover value (for the case in fig. 4.20 crossover tan $\delta \approx 5$), $I_{3/1,LCB}$ is higher than $I_{3/1,linear}$ as can be seen in fig. 4.15 - 4.18. Thus, the effect of LCB is reduced in this frequency range and the difference between LCB and linear polyethylenes is not pronounced. The investigated polyethylenes possess characteristic relaxation time of the order of $\tau = 1/\omega_{crossover}$ = 10^{-2} s - 10^{-3} s and exhibit a weak temperature dependence. In order to extend the study at very high Deborah numbers, high frequencies are needed. However, LAOS at frequencies $\omega_1 > 5$ Hz is not possible with the current experimental devices.

In the case of polyethylenes with no LCB detected, the molecular weight and the molecular weight distribution are considered as the only parameters affecting their non-linear behaviour. Consequently, $I_{3/1}(\gamma_0)$ for the linear and SCB polyethylenes is predicted from corresponding M_w and *PDI* using eq. 4.2. Using the molecular weight distribution, the non-linear behaviour of a polydisperse polyethylene with linear topology can be predicted (see fig. 4.14) and lead to a developement of a more elaborated equation which includes topological features of the polymer.

4.2 Application of FT-Rheology towards blends of linear and LCB industrial polyethylenes

With the use of FT-Rheology and the correlation with ^{13}C NMR results as introduced in the above paragraphs, it is shown that a "fingerprint" of the non-linear rheological behaviour of LCB PE materials can be obtained. Sparse LCB and SCB of a degree as low as $\sim$ 0.1 LCB + SCB/1000 CH_2 can be detected. However, this estimated branching degree is an average value for all the species included in the PE melt. A polydisperse industrial material may consist of macromolecular chains with topologies varying from linear to species of a high branching degree. Within this paragraph, the limits of detectable LCB PE material in a polydisperse (in molecular weight and in topology) PE melt are studied by applying FT-Rheology. For this purpose, blends of industrial polyethylene consisting of a linear and a LCB component of similar M_w and *PDI* have been specifically prepared. The concentration of the LCB containing component varies from 1.5 wt % to 94.5 wt %. As it is presented below, a very low concentration of LCB material to a linear PE melt can be detected (1-5 wt %) via the use of LAOS and FT-Rheology.

A similar approach was presented by Stange et al. [Stange 05] for quantifying LCB in polypropylene. The authors blended linear PP and LCB PP samples and applied size exclusion chromatography (SEC) coupled with multi-angle laser light scattering (MALLS)

using the mean square radius of gyration as a parameter to detect LCB. Rheological measurements where also undertaken and specifically oscillatory shear and extension experiments. A logarithmic mixing rule was applied to predict blend zero shear viscosity, η_0, as a function of the volume fractions and of η_0 of the two blend components.

Blends of linear or SCB with LCB polyethylenes have been extensively studied in the past, with respect to their thermal, rheological and mechanical properties [Yamaguchi 99]. Rheological methods, namely: Cole-Cole plots (loss viscosity, η'', versus storage viscosity, η', loss modulus, G'', versus storage modulus, G' plots and melt complex viscosity, $|\eta^*(\omega)|$, plotted against blend composition were undertaken by Kwag et al. [Kwag 00]. The authors combined the results with morphological studies and examined the miscibility of mPE and high-density polyethylene (HDPE) blends. Perez et al. [Pérez 05] applied rheological techniques to study blends of metallocene linear low-density polyethylene (mLLDPE) and low density polyethylene (LDPE), focusing in their miscibility and processing features. Thermal and rheological properties of mLLDPE/LDPE blends were also investigated by Fang et al. [Fang 05]. The authors used dynamic scanning calorimetry (DSC) and oscillatory shear measurements. The miscibility of mLLDPE materials containing different types of comonomer with LDPE of broad molecular weight distribution was determined. For this purpose, the zero shear viscosity of the blend and the complex viscosity were used, along with the calculated relaxation spectrum. The applicability of a logarithmic mixing rule was also examined. The majority of the samples followed this empirical rule, nevertheless deviations for some blends were found and were attributed to the thermo-mechanical history of the specific materials.

In the present paragraph, the quantities used to analyze the non-linear behaviour of the melt sample are the relative intensity of the 3^{rd} harmonic, $I_{3/1}$, and the relative phase of the 3^{rd} harmonic, Φ_3. A quantification of the LCB content is presented via parameters derived from fitting $I_{3/1}$ as a function of strain amplitude, γ_0, at a fixed excitation frequency, $\omega_1/2\pi$. The thermal stability of the blends is also examined. Taking into account the work of Kwag et al. [Kwag 00], as well as previous papers [Han 87, Xu 01, Hameed 02, Liu 00, Hussein 03, Hussein 04, Pérez 05], the miscibility of the two blended systems at various LCB-PE concentrations is complementary investigated using rheological techniques.

4.2.1 Investigated blends

Sixteen blends generated out of four pure components, two linear and two LCB samples, (see Table 4.1) are investigated. The first blended system is based on mPEmix0 as a linear component and LCBmLLDPE as the LCB part of varying concentration, with both samples being metallocene-catalyzed PE of similar narrow molecular weight distribution. The second blended system consists of the linear L1_117_5.1 and the LCB1_123_7.1, where the LCB

Samples	% wt. LCB-PE	Samples	% wt. LCB-PE
mPEmix0	0	Lmix0(L1_117_5.1)	0
mPEmix1	1.5	Lmix1	1.5
mPEmix2	5.5	Lmix2	5.5
mPEmix3	10	Lmix3	10
mPEmix4	30	Lmix4	30
mPEmix5	50	Lmix5	50
mPEmix6	70	Lmix6	70
mPEmix7	90	Lmix7	90
mPEmix8	94.5	Lmix8	94.5
mPEmix9(LCBmLLDPE)	100	Lmix9(LCB1_123_7.1)	100

Table 4.3: *Polyethylene blends. Samples mPEmix are blends from mLLDPE/LCBmLLDPE mixtures and Lmix are from L1_117_5.1/LCB1_123_7.1 mixtures. For each batch the % wt. content of LCB sample is given. The branching content of the pure components can be found in Table 4.1.*

PE component varies in weight fraction and both are LDPE ofsimilar broad molecular weight distribution. Details for the pure components concerning their linear and non-linear rheological behaviour, as well as their molecular weight distribution are given in Tables 4.1 and 4.2. Sample mPEmix0 corresponds to LLDPE11 in the work of Stadler et al. [Stadler 05]. It is a linear metallocene-catalysed LDPE, with M_w = 135 kg/mol, PDI = 2.0 and it contains octene as comonomer, resulting in a degree of 66.3 SCB/1000 CH_2, as determined via melt-state NMR.

The samples are blended using a Brabender Plasticizer. The chamber is cleaned before each mixing process and filled with 20 g of material. Each blend is mixed at 180 °C for 5 min. For measurements on the ARES rheometer, melt sample discs of 13 mm diameter and 1 mm thickness are pressed, at 150 °C and 20 bars in a Weber hydraulic press under vacuum. All measurements are performed under a nitrogen atmosphere to prevent sample oxidation. The names of each batch and the weight fractions are given in Table 4.3.

4.2.2 Characterization of blend components

The first set of the investigated blends consists of mPEmix0 and LCBmLLDPE varying the weight ratios. The LCB sample has been extensively investigated in previous publications using GPC and creep-recovery measurements [Gabriel 99], by FT-Rheology, melt-state NMR and simulations using the double-convected Pom-pom model (DCPP) in Vittorias et al. [Vittorias 06] and within the present thesis (paragraph 4.1.1). The linear mPEmix0 was analytically and rheologically characterized in Stadler et al. [Stadler 05]. Both samples are metallocene-catalyzed low density industrial polyethylenes. They have similar molecular

weights and distributions ($M_w \approx$ 100kg/mol and *PDI* $\approx$ 2) and both contain SCB from using octene as comonomer. Linear sample mPEmix0 has a higher degree of SCB, which is found to suppress LCB incorporation [Stadler 05]. In the case of LCBmLLDPE, no accurate number of LCB can be given. Melt-state NMR is not able to estimate whether a side-branch of more than 6 carbons is short ($M_{branch} < M_e$) or long ($M_{branch} > M_e$) and the values obtained are the sum of SCB and LCB. Thus, the value of 25.2 LCB + SCB/1000 CH_2 given for this specific sample corresponds to the sum of SCB (from co-ocetene) and LCB incorporated in the polyethylene chain.

All the above mentioned methods conclude that mPEmix0 is a linear polyethylene with SCB and LCBmLLDPE contains SCB and LCB. Following the analysis presented in this chapter and considering the measured $I_{3/1}(\gamma_0)$ and $\Phi_3(\gamma_0)$ for both species, we suggest that LCBmLLDPE has a very low degree of LCB/1000 CH_2, nevertheless detectable by FT-Rheology and approximately 0.1 LCB/1000 CH_2. This is also in qualitative agreement with the results of Gabriel et al. who studied the same material [Gabriel 98, Gabriel 99, Gabriel 02]

The Lmix blends consist of components already presented in paragraph 4.1.1. These samples are highly polydisperse (*PDI* = 5.1 for the linear and 7.1 for the LCB sample). Both have comparable M_w($\sim$ 120 kg/mol). Melt-state NMR measurements confirm the absence of comonomer and no SCB is present in both polyethylenes. Hence, the given value of 0.2 LCB/1000 CH_2 for the LCB1_123_7.1 is considered to be a good estimation for the LCB content (see Table 4.1).

4.2.3 Effect of LCB PE content in blends via SAOS and FT-Rheology

Dynamic mechanical measurements are performed at very low strain amplitudes (SAOS) in the linear regime, using typically γ_0 = 0.1, in order to obtain linear viscoelastic properties of all samples, specifically G', G'' and $|\eta^*(\omega)|$. The results are presented in fig. 4.21 and 4.22 for the mPEmix blends and in fig. 4.23 and 4.24 for the Lmix blends. In the mPEmix blends, the LCB component has a very low LCB content and M_w and PDI similar to the linear component. The LCB sample for the Lmix has a higher relative branching degree and a higher PDI compared to L1_117_5.1. This is the reason for the difference in the discrimination between the mPEmix and the Lmix blends, with respect to their moduli.

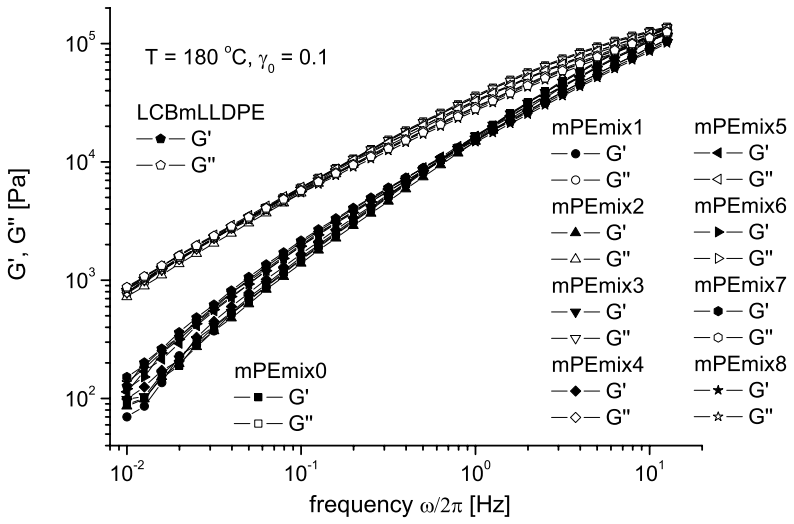

Figure 4.21: *Storage and loss moduli, G' and G'', for linear polyethylene mPEmix0, LCB sample LCBmLLDPE and the mPEmix blends at T = 180 °C with γ_0 = 0.1*

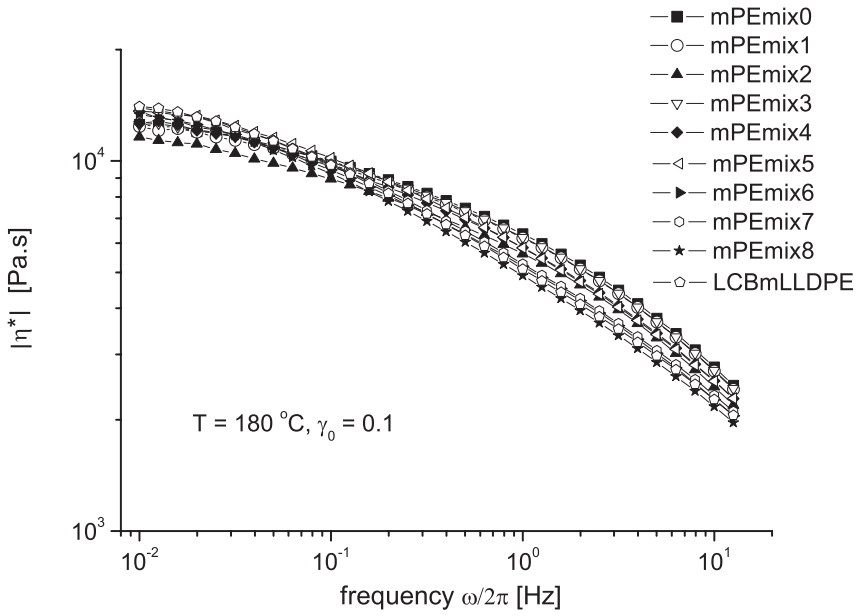

Figure 4.22: *Absolute complex viscosity, $|\eta^*(\omega)|$, at T = 180 °C with γ_0 = 0.1, for mPEmix blends (see Table 4.3).*

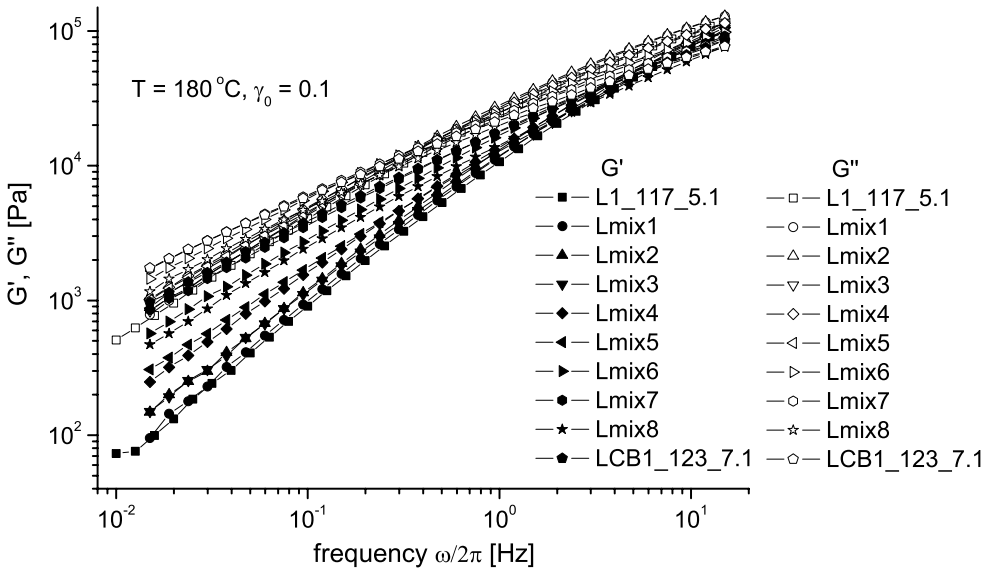

Figure 4.23: *Storage and loss moduli, G' and G'', for linear polyethylene L1_117_5.1, LCB sample LCB1_123_7.1 and the Lmix blends at T = 180 °C with γ_0 = 0.1 (see Table 4.3).*

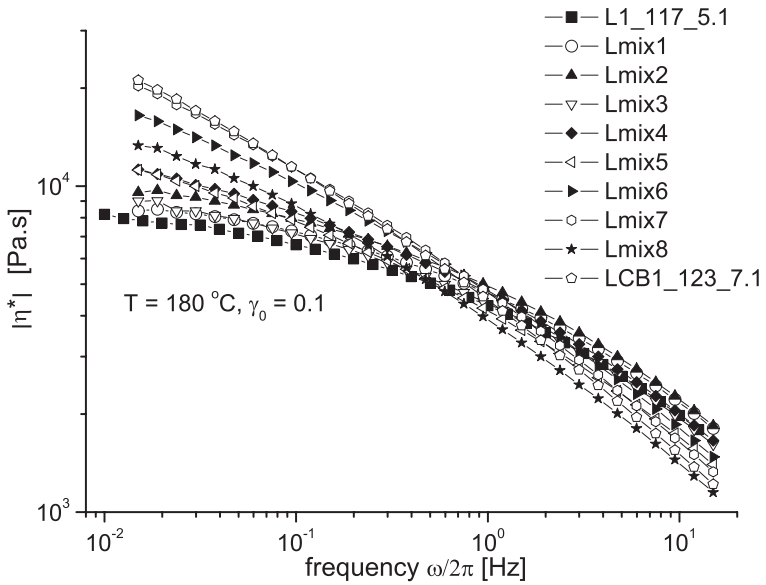

Figure 4.24: *Complex viscosity, $|\eta^*(\omega)|$, for the Lmix blends at T = 180 °C with γ_0 = 0.1.*

Large amplitude oscillatory shear is subsequently applied in order to study the non-linear rheological regime. Strain sweep measurements are performed for each sample at 0.1 Hz, 180 °C and for a strain amplitude range of $0.1 < \gamma_0 < 10$. This is achieved by combining results from measurements undertaken in the ARES and in the RPA rheometer. The resulting stress response is analyzed via FT-Rheology. The relative intensity $I_{3/1}$ and the relative phase Φ_3 as a function of strain amplitude (γ_0) of each mPEmix batch, for strain sweep measurements is presented in fig. 4.25 and fig. 4.26. The $I_{3/1}(\gamma_0)$ and $\Phi_3(\gamma_0)$ for the same LAOS measurements of the Lmix blends is depicted in fig. 4.27 and 4.28. The shape of the $\Phi_3(\gamma_0)$ curve in fig. 4.28, for γ_0 = 1.5-2.5 reflects the stability problems of the ARES geometry at these high strain amplitudes and the instabilities that occur.

As discussed in paragraph 1.5.3, the resulted $I_{3/1}(\gamma_0)$ curves are fitted using eq. 1.47

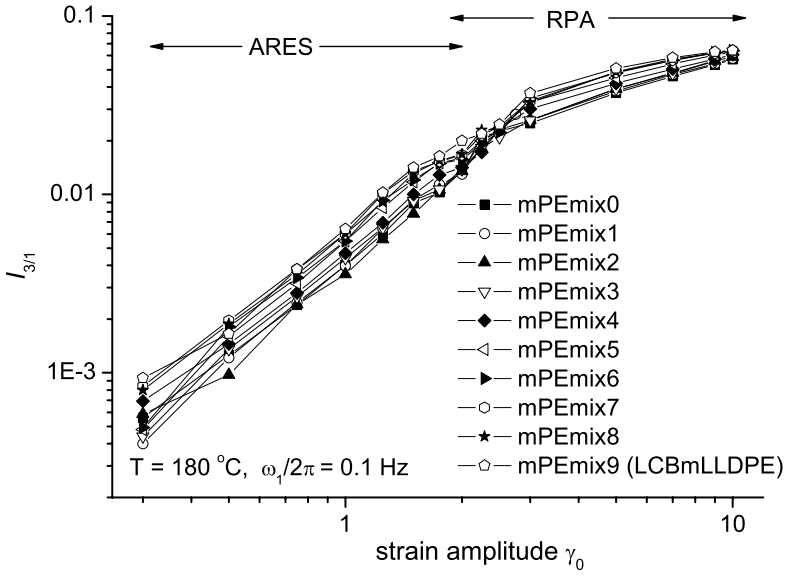

Figure 4.25: *$I_{3/1}$ as a function of strain amplitude γ_0, at T = 180 °C and $\omega_1/2\pi$ = 0.1 Hz, for mPEmix blends. $I_{3/1}$ up to γ_0 = 2.5 (ARES data) shifted to correspond to cone-plate measurements of RPA2000.*

and the parameters *A, B* and *C* derived from this fit are presented in fig. 4.29 for the mPEmix and Lmix blends. The non-linearity plateau value, *A*, and the inverse critical strain amplitude, *B* (=1/γ_0, where $I_{3/1}$ = *A*/2), are increasing with increasing LCB concentration, for both blended systems.

The use of eq. 1.47 to fit $I_{3/1}(\gamma_0)$ requires available data in a broad range of strain amplitudes. In order to have a realistic value for parameter *C*. One needs enough accurate data at low γ_0 (eq. $0.1 < \gamma_0 < 2$). Parameter *A* can be estimated by fitting data at very high strain amplitudes (for PE typically $\gamma_0 > 7$). However, these limits are not always experimentally reachable, as discussed in previous paragraphs. Hence, eq. 1.51 can be used, as for the case

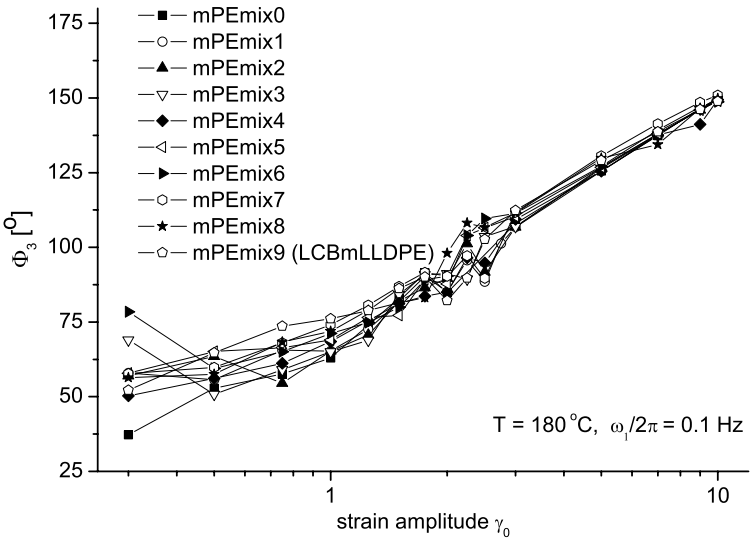

Figure 4.26: Φ_3 *as a function of strain amplitude* γ_0*, at T = 180 °C and* $\omega_1/2\pi$ *= 0.1 Hz, for mPEmix blends. For* $\gamma_0 < 0.5$*, experimental errors are significant.*

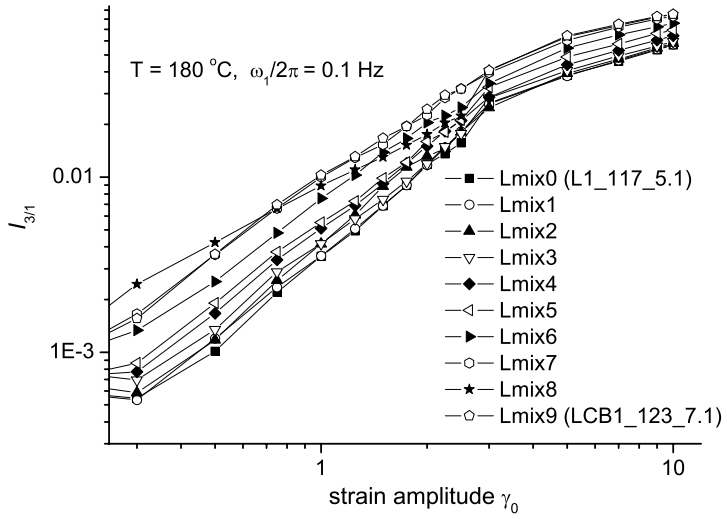

Figure 4.27: $I_{3/1}$ *as a function of strain amplitude* γ_0*, at T = 180 °C and* $\omega_1/2\pi$ *= 0.1 Hz, for Lmix blends.* $I_{3/1}$ *up to* γ_0 *= 2.5 (ARES data) shifted to correspond to cone-plate measurements of RPA2000.*

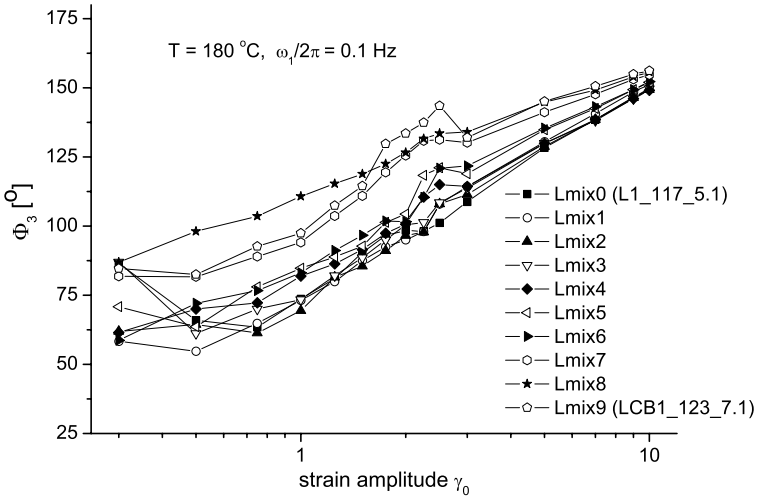

Figure 4.28: *Φ_3 as a function of strain amplitude γ_0, at T = 180 °C and $\omega_1/2\pi$ = 0.1 Hz, for Lmix blends. The shape of $\Phi_3(\gamma_0)$ for γ_0 = 1.5-2.5 is due to flow instabilities at these deformations that occur with the ARES geometry.*

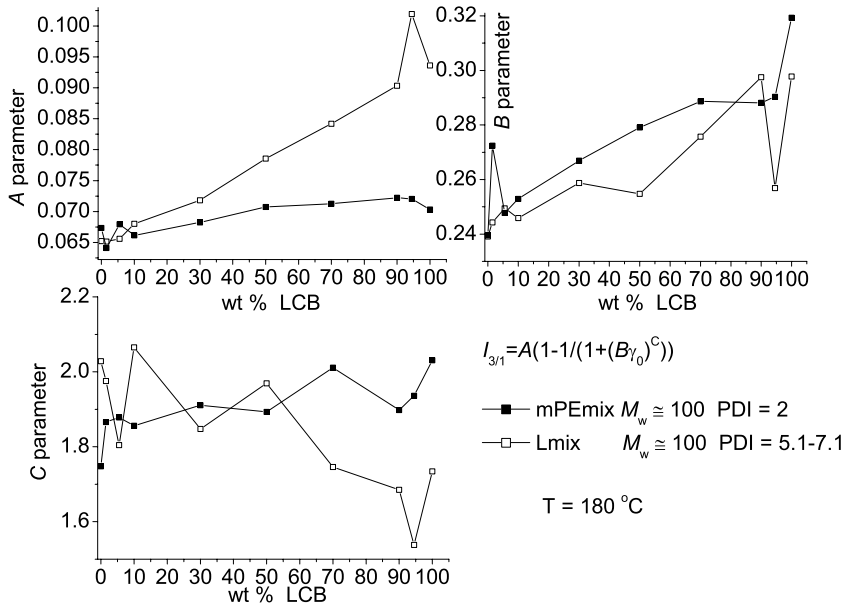

Figure 4.29: *A, B, and C values derived from fitting $I_{3/1}(\gamma_0)$ at 180 °C and 0.1 Hz with eq. 1.47, for both blended systems, as a function of wt % content of LCB sample.*

of model PS samples, for γ_0 up to 2, at 180 °C, for both blend groups. In fig. 4.30 and 4.31 parameters *D* and *C* are depicted, as a function of LCB PE weight concentration. Fittings are performed either by adjusting both parameters, or using *D* as the only adjustable parameter, and *C* as derived from eq. 1.47. Parameter *D* displays a continuous change between the two pure systems, while this is not clear for parameter *C*. The latter is however confined in fit values between the predicted values for the pure components (see table 4.2) and in any case near the theoretically expected values of 1.7-2 [Neidhöfer 03b, Pearson 82].

In both blend series one can observe that an increasing LCB species content increases

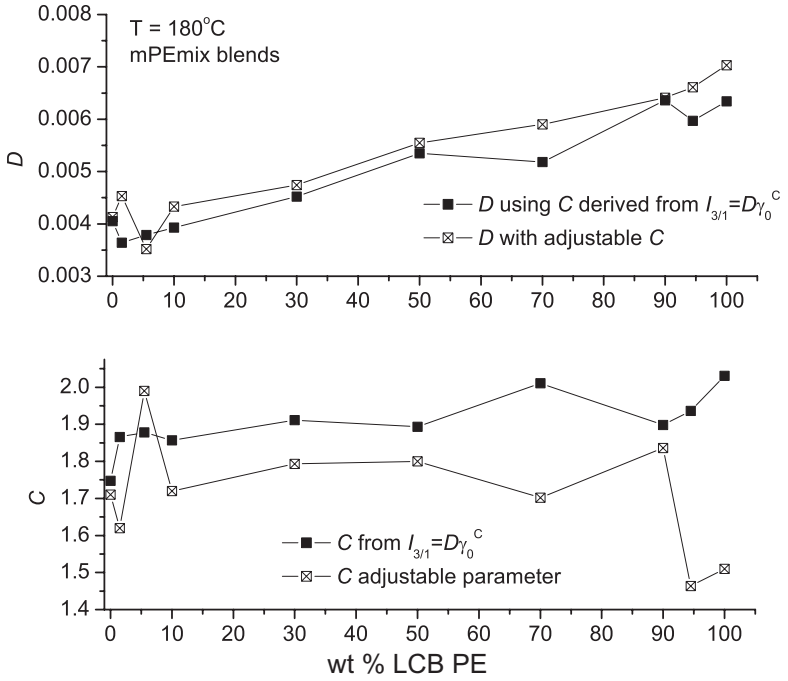

Figure 4.30: *D and C values derived from fitting $I_{3/1}(\gamma_0)$ at 180 °C and 0.1 Hz with eq. 1.51, for mPEmix systems, as a function of wt % content of LCB sample.*

monotonically the measured $I_{3/1}(\gamma_0)$ and $\Phi_3(\gamma_0)$, as reflected in parameters *A*, *B* and *D* (fig. 4.29 - 4.31). The non-linearity plateau (*A*) and the inverse critical strain (*B*) increase with increasing ratios of LCB / linear chains in the blend. The slope of $\log I_{3/1}$-$\log(\gamma_0)$ at low strains (*C*) remains between the values of the linear and the LCB polyethylene samples, and close to values theoretically predicted, *C* = 1.7-2 [Neidhöfer 03b, Pearson 82]. It should be noted that if there is enough data available at very large γ_0, one can calculate a more accurate value of *A*, thus making the determination of a *C* with less errors possible. In the absence of data near the $I_{3/1}(\gamma_0)$ plateau, the derived values of parameter *C* may vary depending on the estimation of *A*. Since there is a theoretical estimation for *C*, we can fit $I_{3/1}$ at low and medium γ_0 by adjusting only parameter *D*. This is done while keeping *C* values in a close agreement with theory, i.e. $\sim$2. The fitting procedure is also performed using both *D* and *C* as adjustable parameters and only small differences in the derived values of *D* are found

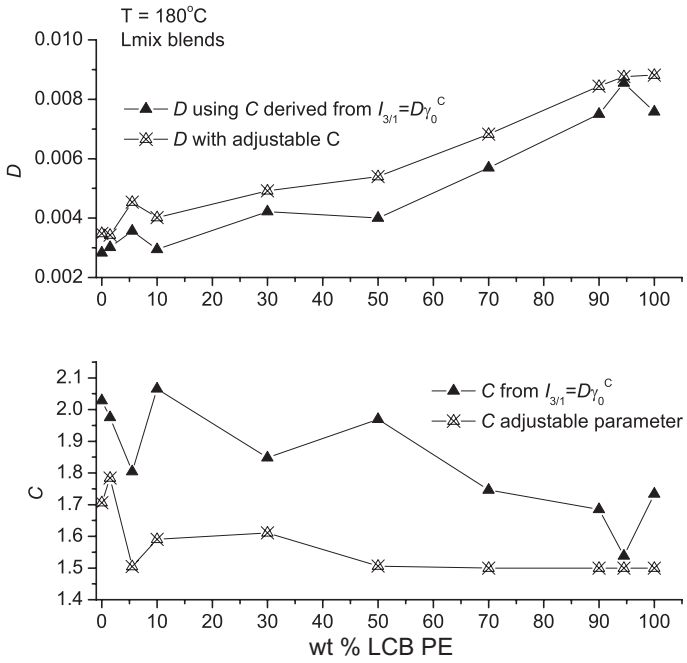

Figure 4.31: *D and C values derived from fitting $I_{3/1}(\gamma_0)$ at 180 °C and 0.1 Hz with eq. 1.51, for Lmix systems, as a function of wt % content of LCB sample.*

(fig. 4.30, 4.31). Generally, there is a weak dependence of *C* on topology and molecular weight distribution and slopes of 1.7 - 2.5 for LCB polyethylenes are expected.

4.2.4 Extended van Gurp-Palmen method for PE blends

In paragraph 4.1.4 the relative phase of the 3^{rd} harmonic at very low strain amplitudes, Φ_3^0 ($lim_{\gamma_0 \to 0}\Phi_3 := \Phi_3^0$) is introduced as a potential new parameter for LCB detection. The same method is applied to the studied polyethylene blends of known LCB PE concentration. For all samples, Φ_3^0 is measured for a frequency range of 0.01 Hz - 5 Hz, at 180 °C. First, the phase lag δ plotted against the complex modulus for all samples is depicted in fig. 4.32 and 4.33. The relative phase of the 3^{rd} harmonic at very low strain for mPEmix blends is shown in fig. 4.34. It can be concluded that an optimum discrimination between linear and LCB topologies can be achieved at low excitation frequencies (e.g. $\omega_1/2\pi$ = 0.02 Hz-0.3 Hz). For the case of mPEmix samples the the discrimination between the blends is simpler with the van-Gurp plot than with the extended Φ_3^0 at higher moduli values. Hence, results are presented from a complex modulus range corresponding to low excitation frequencies for several Lmix blends, where the differences between blends of chaging LCB component concentration is more pronounced (fig. 4.35).

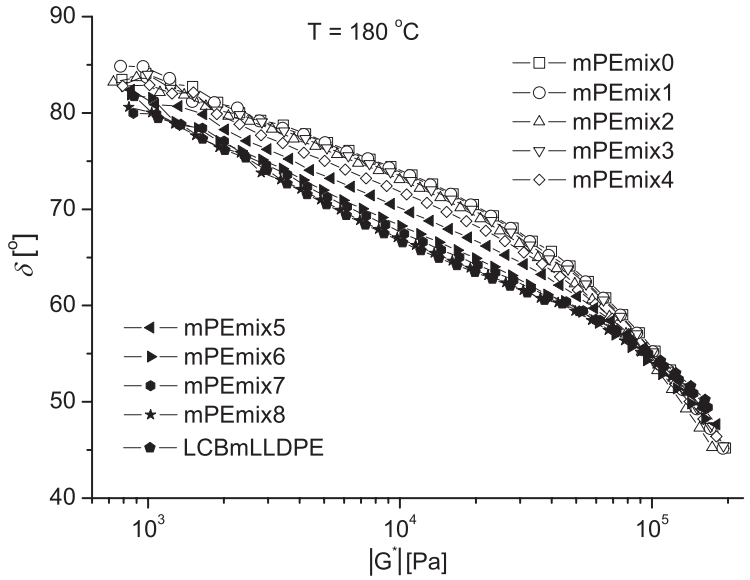

Figure 4.32: *Van Gurp-Palmen plot. Phase lag δ as a function of complex modulus, $|G^*(\omega)|$, for mPEmix blends at 180 °C.*

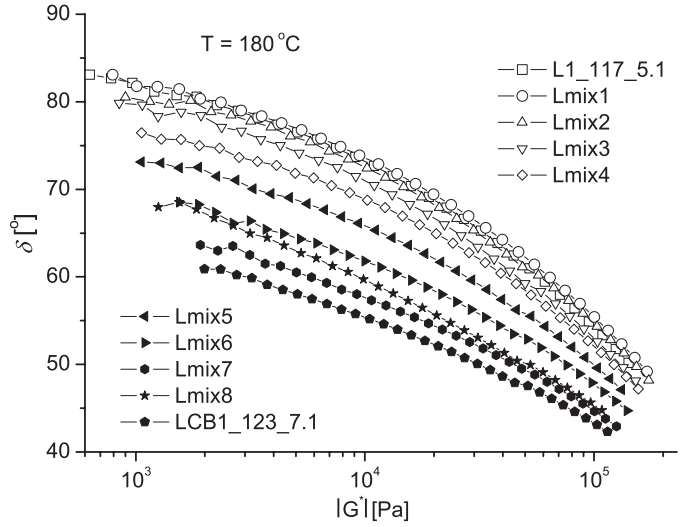

Figure 4.33: *Van Gurp-Palmen plot. Phase lag δ as a function of complex modulus, $|G^*(\omega)|$, for Lmix blends at 180 °C.*

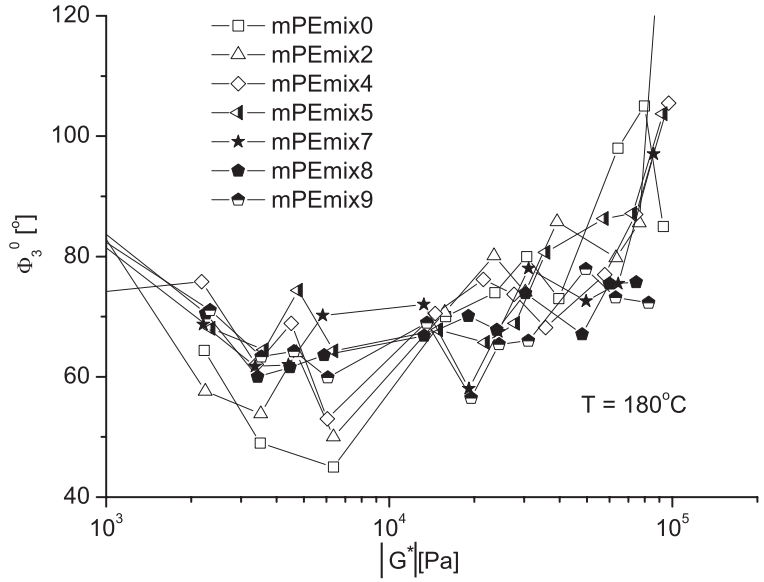

Figure 4.34: *Extended Van Gurp-Palmen plot. Relative phase of 3rd harmonic at low strains (γ_0=0.5), Φ_3^0, as a function of complex modulus, $|G^*(\omega)|$, for mPEmix blends at 180 °C. For $|G^*(\omega)| > 2{\times}10^4$, no discrimination can be achieved between the specific blends.*

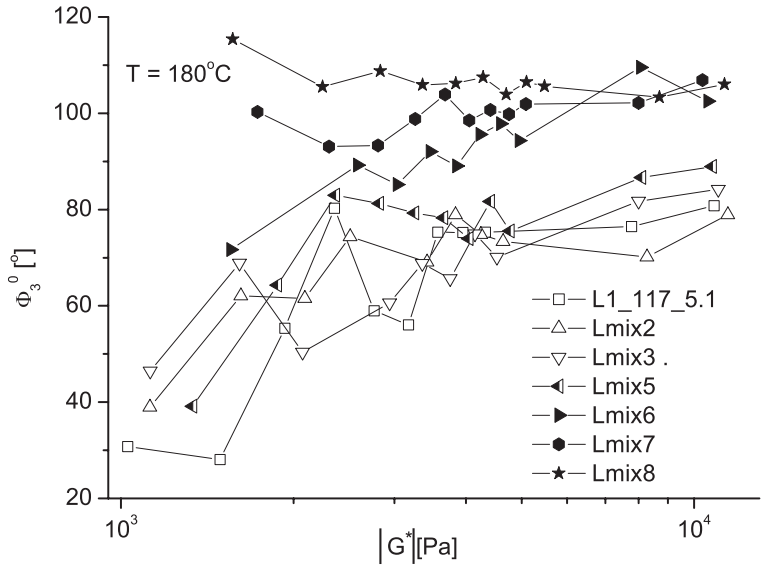

Figure 4.35: Φ_3^0 *as a function of* $|G^*(\omega)|$*, measured at low frequencies,* $\omega_1/2\pi$ *= 0.02 Hz - 0.3 Hz, for Lmix blends at 180 °C.*

4.2.5 Mixing rules for predicting non-linearity of linear/LCB blends

Stange et al. [Stange 05] studied the rheological behaviour of blends with linear and LCB polypropylene. The authors applied a logarithmic mixing rule between the two blend components to follow the zero-shear viscosity. In our case a linear mixing rule is applied to predict $I_{3/1}(\gamma_0)$ of each blend:

$$I_{3/1,blend}(\gamma_0) = \phi_{(1)} I^{(1)}_{3/1}(\gamma_0) + \phi_{(2)} I^{(2)}_{3/1}(\gamma_0) \tag{4.3}$$

where ϕ is the mass fraction of each component. A second effort is also presented for predicting the non-linear behaviour of the binary blends by a logarithmic mixing rule [Stange 05]:

$$log(I_{3/1,blend}(\gamma_0)) = \sum_{i=1}^{n^{th}component} \phi_{(i)} log(I^{(i)}_{3/1}) \tag{4.4}$$

and specifically for the studied binary blends:

$$log(I_{3/1,blend}(\gamma_0)) = \phi_{(1)} log(I^{(1)}_{3/1}(\gamma_0)) + \phi_{(2)} log(I^{(2)}_{3/1}(\gamma_0)) \tag{4.5}$$

Results for LCB concentrations of 10 wt %, 50 wt % and 90 wt % are shown in fig. 4.36 for mPEmix blends. In fig. 4.37 the results for all Lmix blends are depicted. For the majority of the blends, both mixing rules describe in a satisfactory way the blend $I_{3/1}(\gamma_0)$. However for some cases, e.g. for very large LCB PE weight fractions, the linear mixing rule is in slightly better agreement with experimental data. In fig. 4.36 the small difference between the predicted $I_{3/1}$ with eq. 4.3 and 4.5, is not clear due to the small difference of the non-linearities between the two components and the logarithmic scale used.

The non-linear behaviour as quantified by $I_{3/1}$ is a function of the LCB concentration. Thus, it can be expected to be described by a blend mixing rule. An empirical mixing rule is supposed to predict the blend non-linearity from the known $I_{3/1}(\gamma_0)$ of the pure components and the weight fractions, since they have similar molecular weight distribution (see eq. 4.3 and 4.5). The logarithmic rule gives better predictions for the Lmix blends and for some cases of the mPEmix. The linear mixing equation performs better for blends with high LCB PE weight fractions. However, both mixing rules do not describe successfully the non-linearities of all the investigated blends. In previous works this has been interpreted

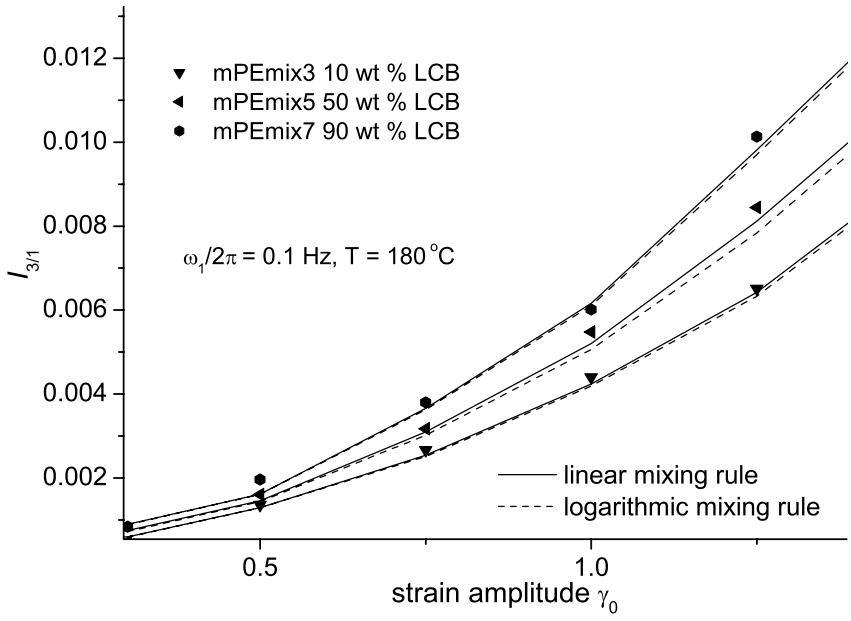

Figure 4.36: *Comparison of experimental $I_{3/1}(\gamma_0)$ and predicted from linear and logarithmic rule, for mPEmix blends at 180 °C at low and medium strain amplitudes.*

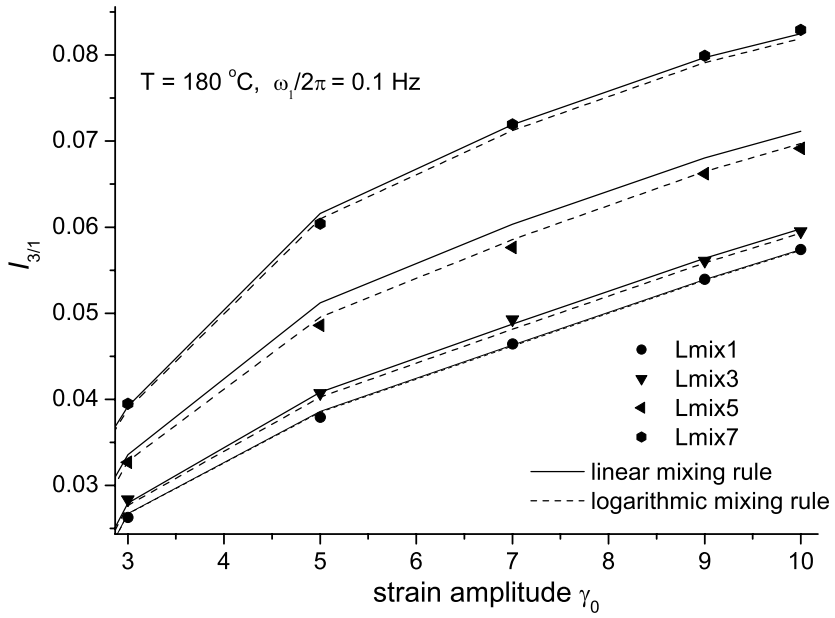

Figure 4.37: *Comparison of experimental $I_{3/1}(\gamma_0)$ and predicted from linear and logarithmic rule, for Lmix blends at 180 °C. Results for $\gamma_0 > 3$.*

as an indication of blend immiscibility [Kwag 00]. However, one must be aware that these are empirical rules with no theoretical basis and thus, they cannot support stringent conclusions about material behaviour. The failure to describe rheological properties (linear and non-linear) could be overcome with the use of more elaborated and theory based mixing rules.

4.2.6 Limits of LCB PE content detectable via FT-Rheology

Polyethylenes of the mPEmix group with an LCB sample mass fraction lower than 10 wt % do not present significant differences in the linear spectrum. However, for large strain amplitudes ($\gamma_0 > 3$) even sample mPEmix1 (1.5 wt % LCBmLLDPE) presents a slightly higher $I_{3/1}$. For example at γ_0 = 5, mPEmix1 has a slightly higher non-linearity value compared to that of the linear pure component, mPEmix0 ($I_{3/1}$ = 3.8% and 3.7% respectively). Such small differences in the non-linear behaviour are close to the limits of the reproducibility of the measurement, nevertheless it can be detected and quantified with the optimized experimental setup at large amplitudes (see chapter 2). Concerning the LCB sample, an addition of 5.5 wt % of linear chains, is adequate to change the non-linear behaviour from that of a 100 wt % LCBmLLDPE. This is also reflected in the parameters *A, B, C,* and *D* (fig. 4.29 - 4.31).

For the Lmix blends the lowest detectable LCB component concentration is 5.5 wt % and the lowest detectable linear component weight fraction is also found to be 5.5 wt %. The higher sensitivity of FT-Rheology for the Lmix series can also be explained by the different and high polydispersity between the two blend components. Higher polydispersity generally results in higher $I_{3/1}(\gamma_0)$ and $\Phi_3(\gamma_0)$ values (see chapter 3 and paragraph 4.1.1). Hence, adding a very small weight fraction (e.g. 1-5 wt %) of a sample with a higher PDI into a linear PE will cause an additional increase of non-linearity, via the broadening of the molecular weight distribution. This increase of $I_{3/1}(\gamma_0)$ and $\Phi_3(\gamma_0)$ is thus attributed not only in the presence of more LCB chains but also in the presence of larger macromolecules, as discussed in the paragraph 4.1.1 and in chapter 3. One additional factor may be that the chains in the high molecular weight tail ($M > 300$ kg/mol) of the distribution for the LCB1_123_7.1 can contain a higher relative branching degree. Hence, a relatively small amount of this component (1-5 wt %) is enough to induce a different non-linear rheological behaviour under LAOS conditions as recorded by FT-Rheology. as a comparison, the analysis of the moduli measured in the linear regime with SAOS is sensitive to LCB PE for concentrations higher than 30 wt % for mPEmix and higher than 10 wt % for the Lmix blends.

4.2.7 Melt stability and miscibility of the studied blends

Within the blend analysis, only rheological techniques are used in order to check the miscibility and stability of the blends. Anaylisis via differential scanning calorimetry (DSC) [Fang 05] or scanning electron microscopy (SEM) [Kwag 00] is not presented. It has to be taken into consideration that all four blend pure components are industrial samples and contain stabilizers and no degradation is observed during the experiments. Large amplitude oscillatory shear tests performed at low frequencies $\omega_1/2\pi$ = 0.01 Hz and at test temperature of 180 °C show that the samples mPEmix0, mPEmix9, Lmix0 and Lmix9 are stable towards their moduli and non-linear properties ($I_{3/1}$, Φ_3), for more than 2h (typical duration of LAOS measurements).

The homogeneity of the blends is initially examined by monitoring the resulting torque in the Brabender mixer as a function of time. In fig. 4.38 the torque is plotted against the mixing time for two blends, mPEmix5 and Lmix5. We can conclude that the mixing time is adequate to achieve a homogeneous blend.

Furthermore, linear properties (G', G'', tan δ) of each blend are measured with frequency

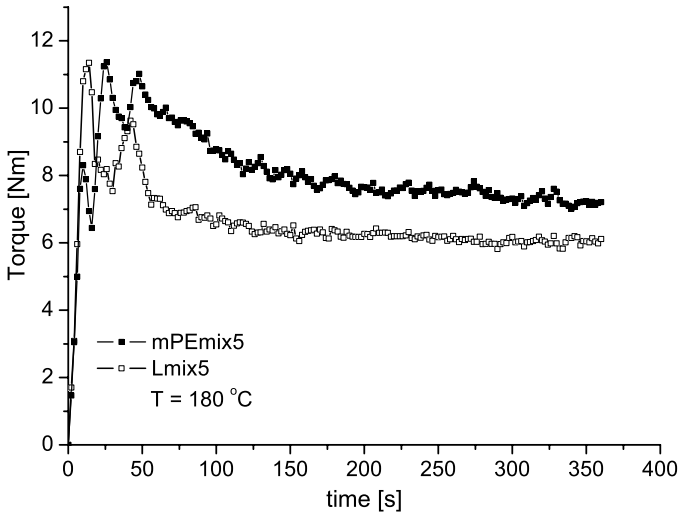

Figure 4.38: *Torque measured in the Brabender plasticizer as a function of mixing time, for blends mPEmix5 and Lmix5 at 180 °C.*

sweeps using low strain amplitudes (typically γ_0 = 0.1) before and after each non-linear measurement and within reproducibility no differences are found in the linear rheological spectrum, which is a strong evidence of blend stability at the specific experimental conditions. Finally, for each strain sweep at LAOS conditions ($I_{3/1}(\gamma_0)$ and $\Phi_3(\gamma_0)$ measurements) and for each frequency sweep for $\Phi_3^0(\omega)$ measurements, new samples are used.

The miscibility of the blends is investigated by applying LAOS for more than 2h, at T = 180 °C, $\omega_1/2\pi$ = 0.1 Hz, with γ_0 = 0.5. The complex modulus, $|G^*(\omega)|$, normalized to the

initial complex modulus $|G^*(\omega)|_0$ (at t = 0 sec) and $I_{3/1}$ recorded is presented in fig. 4.39 for sample Lmix5. The increase of $|G^*(\omega)|$ is negligible ($< 5\%$) and the relative intensity of the 3^{rd} harmonic is also quite stable ($0.16 \pm 0.01\%$). This suggests that no phase separation takes place, at least during the time needed for a series of SAOS (measurement of G', G'', tan δ), LAOS strain and frequency sweep measurements. The studied blends are stable at the specific conditions [Stange 05].

In order to further verify the miscibility of all blends via rheological techniques in

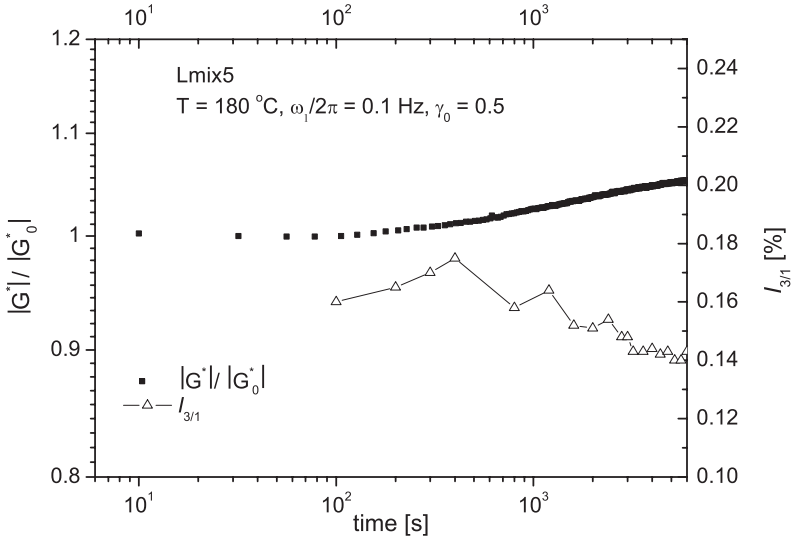

Figure 4.39: *Blend stability. Complex modulus normalized to complex modulus at time t = 0, $|G^*(\omega)|$ / $|G^*(\omega)|_0$ and relative intensity $I_{3/1}$ as a function of time for LAOS at 180 °C, $\omega_1/2\pi$ = 0.1 Hz and γ_0 = 0.5.*

fig. 4.40 and 4.41, the Cole-Cole plots and the G'' plotted against G', for all blends are presented, following the approach of Kwag et al. [Kwag 00]. The mPE blends show a semi-circular relationship and the same slope of G'' versus G', which according to Kwag et al. [Kwag 00] and Han and Kim [Han 87] indicate miscibility. The Lmix blends show deviations from this behaviour. For the case of the mPEmix blends, the resulting Cole-Cole and G'' against G' plots reinforce the argument of miscibility for these specific mixtures. The loss viscosity, η'', plotted against the storage viscosity, η'', presents a semi-circular pattern for all mPEmix blends. The shift of the curve maximum can be attributed solely to the presence of LCB, since the components mPEmix0 and LCBmLLDPE have similar molecular weight distributions [Schlatter 05]. Immiscibility could be considered for the case of the Lmix blends by solely observing their specific Cole-Cole and G'' versus G' curves (fig. 4.42 and 4.43). However, Kwag et al. [Kwag 00] and Schlatter et al. [Schlatter 05] suggest that this can also be attributed to the combination of high polydispersity and the presence of LCB.

Furthermore, taking into account the monitored moduli and non-linearity of fig. 4.39, the spread of the curves observed in fig. 4.42 and 4.43, can be attributed to the combined

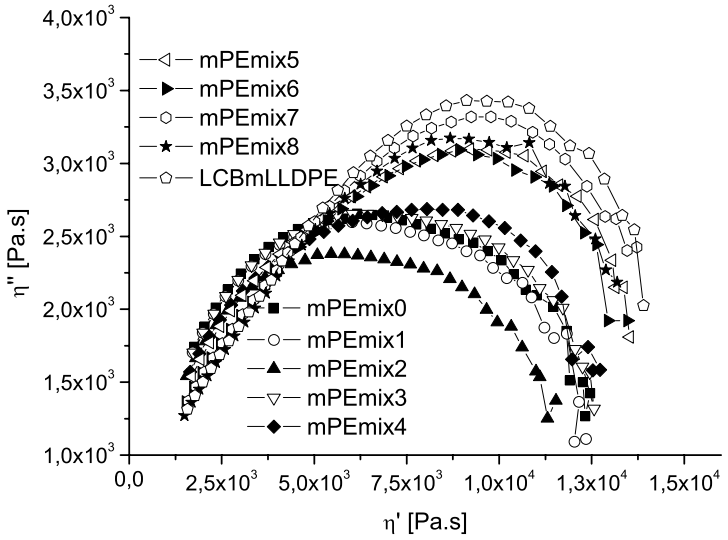

Figure 4.40: *Cole-Cole plot for mPEmix blends at 180 °C.*

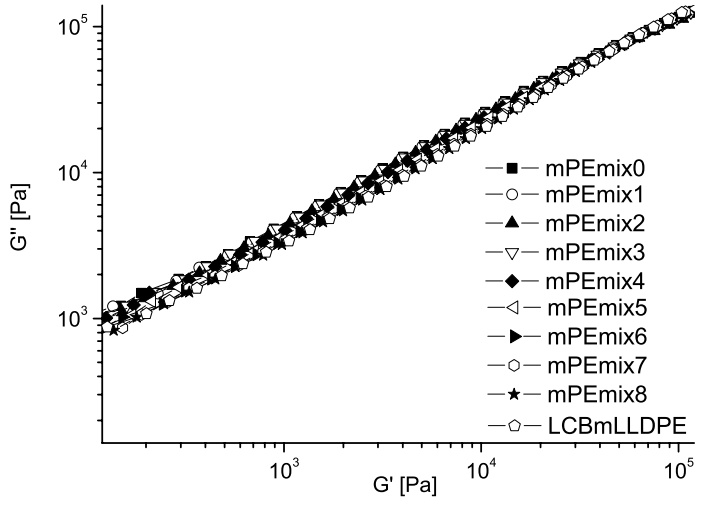

Figure 4.41: *Loss modulus versus storage modulus for the mPEmix at 180°C.*

high polydispersity and higher branching degree (LCB/1000 CH_2) of the samples (PDI $\approx$ 5-7). Additionally, the blend components have predominantly identical chemical structure and similar molecular weight distribution. Both mPEmix0 and LCBmLLDPE are produced with metallocene catalysts and contain co-octene. Samples L1_117_5.1 and LCB1_123_7.1 are homopolymers with no SCB. Linear L1_117_5.1 is produced by Ziegler-Natta method and LCB1_123_7.1 is synthesized with Cr as catalyst. Components of each blend system mainly differ only in the polymer topology (and small differences in M_w and *PDI*) and specifically in the existence of LCB (the SCB type is similar for each component pair). Hence, no separation between the two phases is expected, due to the similar Van der Waals interactions.

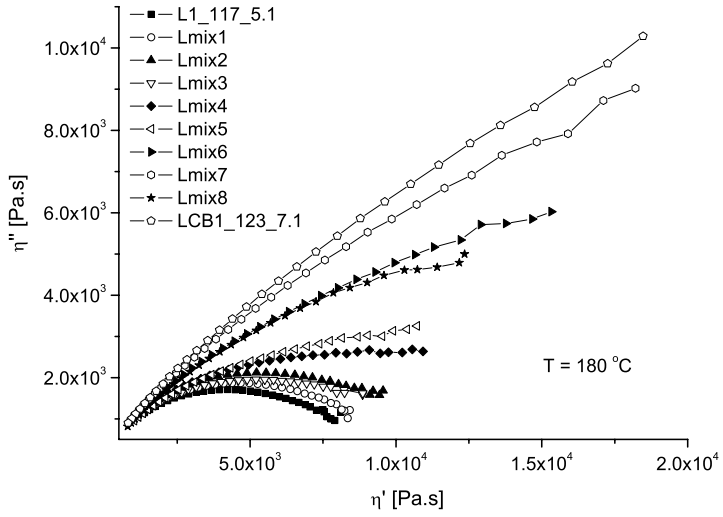

Figure 4.42: *Cole-Cole plot for Lmix blends at 180°C.*

4.3 LAOS simulations with the DCPP model for LCB industrial polyethylenes

4.3.1 Prediction of shear stress and non-linearities during LAOS

Large amplitude oscillatory shear flow is simulated for some of the investigated polyethylene melts, according to the method introduced in chapter 2 and already applied on PS branched model systems in chapter 3. The resulting stress response is analysed in the same way as the experimental torque signals, via FT-Rheology analysis. The linear parameters of the DCPP model, i.e. the relaxation time λ_i and the shear modulus of each mode G_i of each

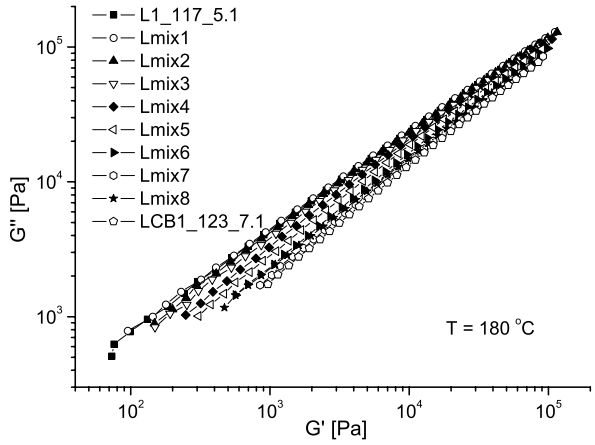

Figure 4.43: *Loss modulus versus storage modulus for the Lmix at 180°C.*

mode are identified by fitting experimental data of G', G'' and complex viscosity, $|\eta^*(\omega)|$. As an example, the fit of LCBmLLDPE with a 4-mode DCPP model is presented in fig. 4.44. Inkson et al. [Inkson 99] and Graham et al. [Graham 01] have indeed proposed the use of a multi-mode model to account for the complex architecture of a branched LDPE. The superposed "pom-pom macromolecules" of different relaxation times and arm number will account for the relaxation processes of the polydisperse macromolecules studied, that contain multiple irregularly spaced long-chain branches (see Table 4.1).

Simulations are performed at conditions corresponding to various tan δ as measured in the linear regime. In fig. 4.45 the relative intensities, $I_{3/1}(\gamma_0)$, predicted for both polyethylenes for selected values of non-linear parameters, q_i and λ_i/λ_{si} are displayed. Strain sweeps are simulated at conditions corresponding to tan δ = 2. In fig. 4.46 the predicted $I_{3/1}$ for mLLDPE and LCBmLLDPE for LAOS with γ_0 = 3, for a range of tan δ between 1.5 and 6.5 are presented. The predicted crossover between $I_{3/1,LCB}$ and $I_{3/1,linear}$ is close to the one measured experimentally.

An analysis of the effects of non-linear model parameters on the resulting non-linearity, i.e $I_{3/1}(\gamma_0)$ and $\Phi_3(\gamma_0)$, is performed. This correlation is needed for understanding the behaviour of different "pom-pom molecule blends" in the non-linear regime. Both non-linear parameters, *q* and λ_s, are found to affect the shape of the resulting $I_{3/1}(\gamma_0)$ and $\Phi_3(\gamma_0)$ curves. Simulation results of $I_{3/1}$ and Φ_3 for LCBmLLDPE at 0.04 Hz and 180 °C (where tan δ = 3.5 in the linear regime) are shown in fig. 4.47 and 4.48. Each curve corresponds to a different "blend of pom-pom molecules" chosen to decouple the non-linear behaviour of this LCBmLLDPE grade [Inkson 99].

The predicted $I_{3/1}(\gamma_0)$ is fitted by eq. 1.47. Parameters *A*, *B* and *C*, defining the shape of the resulting sigmoidal curve, are correlated to the non-linear parameters *q* and λ/λ_s. Equation 1.47 exhibits a good fit between experimental and predicted $I_{3/1}(\gamma_0)$ data for all

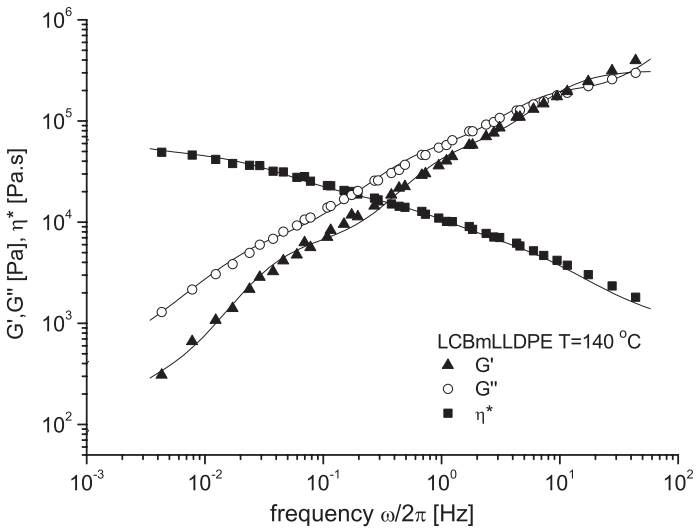

Figure 4.44: *Fit of linear rheological material properties of LCBmLLDPE, by a 4-mode differential DCPP model. Experimental data for G', G'' and $|\eta^*(\omega)|$ obtained by dynamic oscillatory shear at T = 140 °C.*

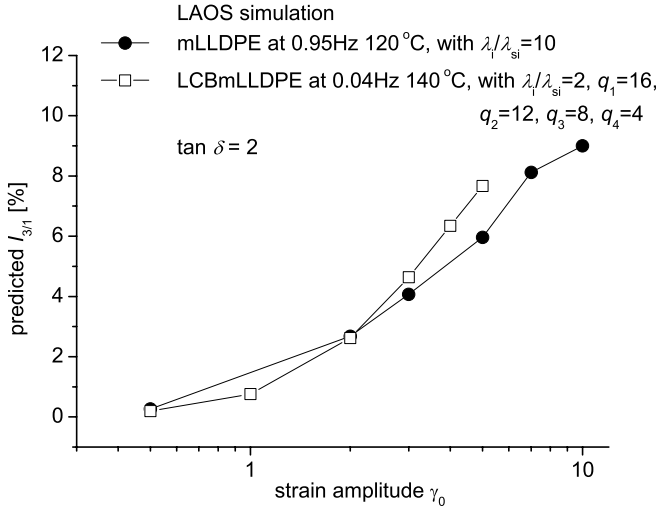

Figure 4.45: *Predicted $I_{3/1}(\gamma_0)$ from DCPP model, for mLLDPE and LCBmLLDPE samples at tan δ = 2.*

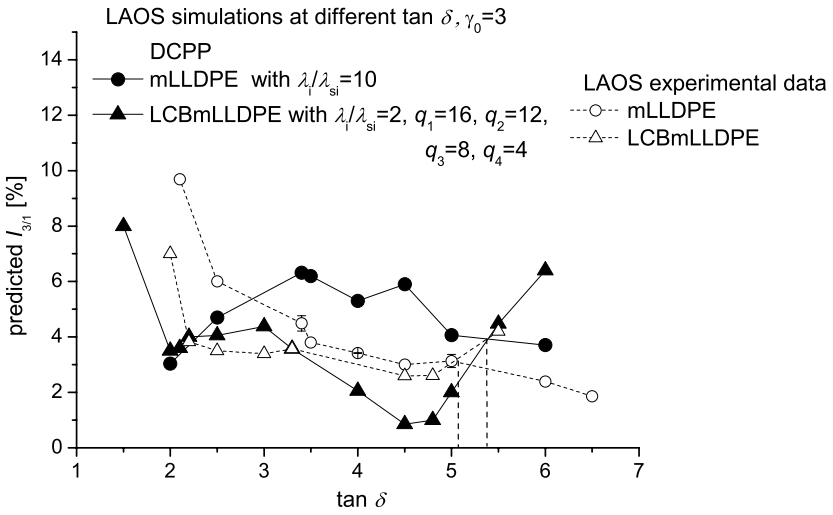

Figure 4.46: *Predicted $I_{3/1}$ using DCPP at conditions corresponding to different tan δ in the linear regime.*

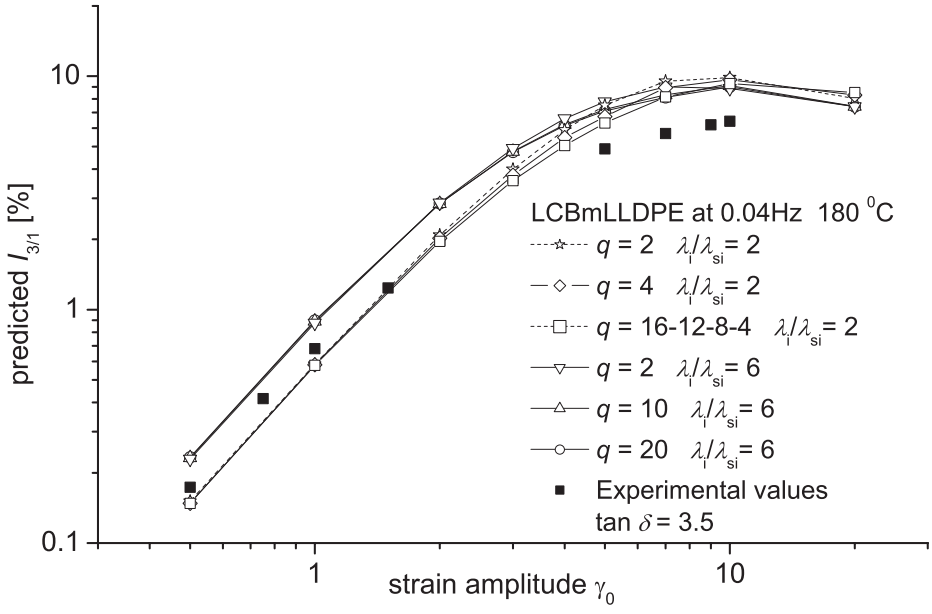

Figure 4.47: *Effect of non-linear parameters q_i and λ_i/λ_{si} on predicted $I_{3/1}$ for LCBmLLDPE at tan δ = 3.5*

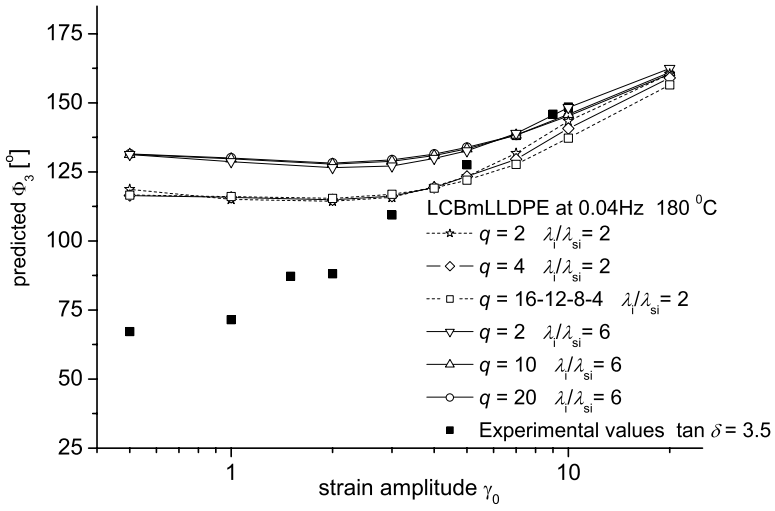

Figure 4.48: *Effect of non-linear parameters q_i and λ_i/λ_{si} on predicted Φ_3 for tan δ = 3.5 in the linear regime.*

cases in fig. 4.47, as demonstrated for an example in fig. 4.49.

Predictions for different combinations of q_i and λ_i/λ_{si} are fitted. We find that parameter *A* exhibits a very weak dependence on both non-linear parameters (A = 0.10 - 0.0002q - 0.0023λ/λ_s). Parameter *B* is very weakly dependent on number of side-arms (B = 0.25 - 0.00078q + 0.023λ/λ_s). Thus, to simplify our approach we neglect the q-dependent terms. The dependence of *A*, *B* and *C* with respect to molecular architecture for the DCPP model can be then described empirically as follows:

$$\begin{aligned} A &= 0.1 - 0.0023\lambda/\lambda_s \\ B &= 0.25 + 0.023\lambda/\lambda_s \\ C &= 2.92 - 0.02q + 0.018\lambda/\lambda_s \end{aligned} \tag{4.6}$$

An increasing number of arms causes a slight reduction on the non-linearity plateau (*A*), which can be considered as a dynamic dilution of the pom-pom molecule from its arms. Furthermore, a pom-pom with a large q has a small inverse critical strain, *B*, which means that higher deformations are needed to have $I_{3/1}$ = *A*/2 for this material. The parameter *C* is also reduced when increasing the number of arms. The ratio λ/λ_s is proportional to the number of entanglements (consequently to the total length) of the backbone chain in a pom-pom molecule (see eq. 2.19). Thus, one can conclude that pom-poms with large backbones (and hence short arms since the total molecular weight is constant) present low non-linearity plateau, high inverse critical strain and large log($I_{3/1}$)-log(γ_0) slopes. The non-linearity in a LAOS flow of the pom-pom chain with large λ/λ_s increases at smaller

deformations but reaches a lower plateau, compared with pom-poms with the same number of arms but of shorter backbone. Consequently $I_{3/1}$, as predicted from the DCPP model and the non-linearity of LCBmLLDPE can be empirically expressed as:

$$I_{3/1}(\gamma_0) = (0.1 - 0.0023\lambda/\lambda_s) \times (1 - \frac{1}{1 + ((0.25 + 0.023\lambda/\lambda_s)\gamma_0)^{(2.92-0.02q+0.018\lambda/\lambda_s)}}) \quad (4.7)$$

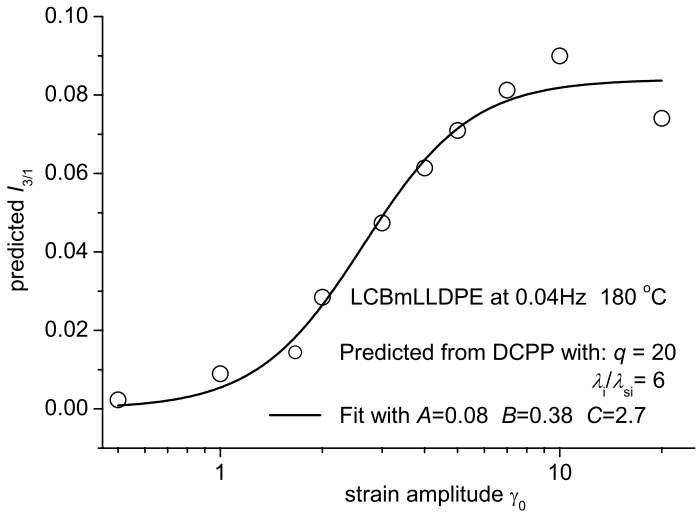

Figure 4.49: *Predicted $I_{3/1}$ for different strain amplitudes from DCPP with q_i = 20 and λ_i/λ_{si} = 6, and $I_{3/1}(\gamma_0)$ from eq. 1.47 for parameters A = 0.08, B = 0.38 and C = 2.7.*

A comparison between the *A, B* and *C* parameters derived from fitting the predicted $I_{3/1}(\gamma_0)$ and those calculated by eq. 4.6 is depicted in fig. 4.50, 4.51, and 4.52 respectively.

It is worth mentioning that the parameters *A* and *B* show a minor dependence with respect to *q* as compared to parameter *C*. However, although the rheology of the melt is described with a 4-mode model, it is remarkable that the predictions show a quite low deviation with respect to the experimentally estimated values.

In order to estimate the effect of the DCPP molecular parameters on $I_{3/1}(\gamma_0)$ and $\Phi_3(\gamma_0)$, a broad range of deformations is needed in the LAOS simulations. Within the present paragraph, LAOS with strain amplitudes $0.5 < \gamma_0 < 20$ is studied. Experimental results shown in fig. 4.11, 4.12 suggest that a correlation is not easily identified between increasing $I_{3/1}(\gamma_0)$ and branching levels. Thus, it is expected that a higher number of arms or a higher ratio of orientation/stretching relaxation times λ_i/λ_{si} do not result in monotonically

increasing intensities and phases for LCB polyethylene in the whole range of simulated γ_0.

The above conclusion is in contrast with Schlatter et al. [Schlatter 05]. However, in the present work LAOS flow is predicted using the DCPP model for a broader range of applied strain amplitudes and frequencies, while Schlatter could only apply strain amplitudes of up to γ_0 = 4. For most simulation cases, $I_{3/1}$ and Φ_3, are not sensitive with respect to *q* at low strain amplitudes ($\gamma_0 < 3$). Generally, at constant number of arms q_i, an increased ratio of λ_i/λ_{si} leads to a higher $I_{3/1}$. This ratio is proportional to the backbone length as suggested by McLeish and Larson [McLeish 98], and Inkson et al. [Inkson 99], who suggested that $\lambda \propto {M_b}^3$, $\lambda_s \propto {M_b}^2$ hence $\lambda/\lambda_s \propto M_b$. Consequently, higher non-linearity for a broad range of shear deformations suggests that the polymer melt behaves like a "blend of pom-poms" with longer backbones. Hence, the time-determining step of the stress relaxation is the orientation process (since $\lambda >> \lambda_s$). Furthermore, simulations show the same trend as the experimental FT-Rheology results. Under conditions corresponding to high tan δ in the linear spectrum, LCBmLLDPE has a higher predicted non-linear behaviour than mLLDPE. This result agrees qualitatively with experimental data for the whole range of investigated tan δ (fig. 4.46).

The relative phase Φ_3 is mainly affected by molecular architecture (*q*, λ_s), for LAOS simulation with strain amplitudes $\gamma_0 > 3$ (fig. 4.48). The DCPP model overestimates Φ_3 at low strains ($\gamma_0 < 2$) for this specific sample, which increases with increasing λ/λ_s and levels off for $\gamma_0 < 3$. This could suggest that a longer backbone introduces higher non-linearities ($I_{3/1}$), but with a higher phase value Φ_3 as compared to the main material response. Furthermore, higher number of side-arms results in lower Φ_3 for the same λ/λ_s ratios.

The behaviour of this "pom-pom material" in the non-linear regime depends on branching level and relaxation mechanism. From eq. 4.7 we could suggest that the plateau *A* of the non-linearity of a material (see eq. 1.47) has a weak dependence on both number of arms and relaxation mechanism. The inverse critical strain amplitude 1/*B* depends strongly only on the backbone length and consequently on the length of the arms (since M_{total} = $M_{backbone}$ + 2qM_{arms}). Parameter *C* depends on *q* and λ/λ_s and decreases with increasing number of arms and decreasing backbone length. Parameter *A* has a typical value of 0.1 $\pm$ 0.05 for LCB PE. For LCBmLLDPE modelled by DCPP, we find values of *A* between 0.08-0.1. Parameter *B* is typically 0.2, suggesting that a polyethylene "pom-pom" blend reaches the half-maximum non-linearity at around $\gamma_0 \approx 5$. Parameter *C* is generally approximately 2 [Neidhöfer 03b, Helfland 82, Pearson 82]. The DCPP model overestimates *C*, and predicts typical values around 2.9. In order to obtain a lower value of *C* we suggest that the LCBmLLDPE structure can be decoupled into a blend of "pom-pom" macromolecules with a high number of branches and shorter backbones. For the specific case of LCBmLLDPE, in order to minimize the deviation between experimental and predicted values of parameters *A*, *B*, *C*, we choose: λ_i/λ_{si} = 3, q_i = 30. In addition, Φ_3 will be lower for a large q_i and lower λ_i/λ_{si}, thus reducing the deviation between experimental FT-Rheology data and LAOS simulation results.

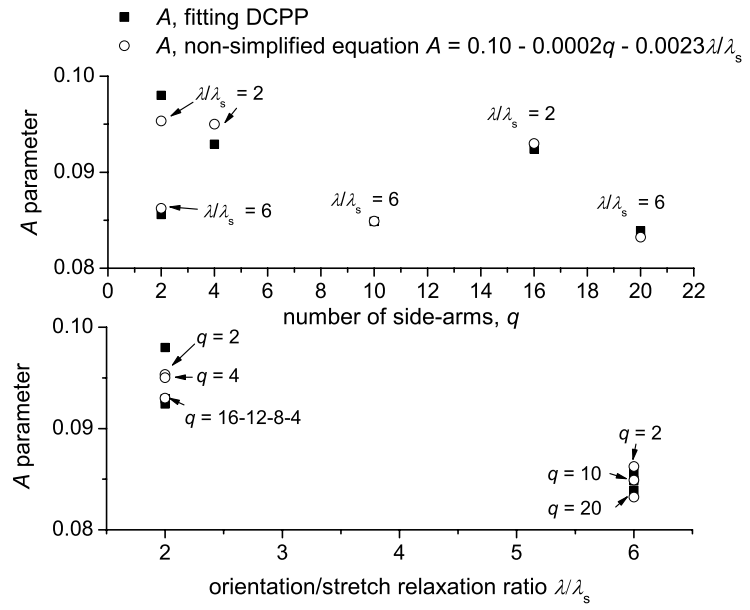

Figure 4.50: *Comparison between parameter A values derived from fitting predicted $I_{3/1}(\gamma_0)$ and empirical descriptive eq. 4.6. Both q_i and λ_i/λ_{si} are varied in all cases.*

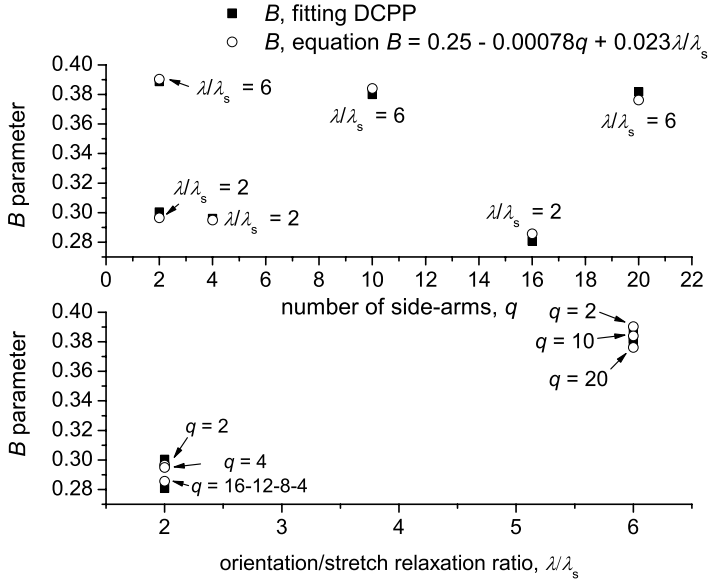

Figure 4.51: *Comparison between parameter B values derived from fitting predicted $I_{3/1}(\gamma_0)$ and empirical descriptive eq. 4.6. Both q_i and λ_i/λ_{si} are varied in all cases.*

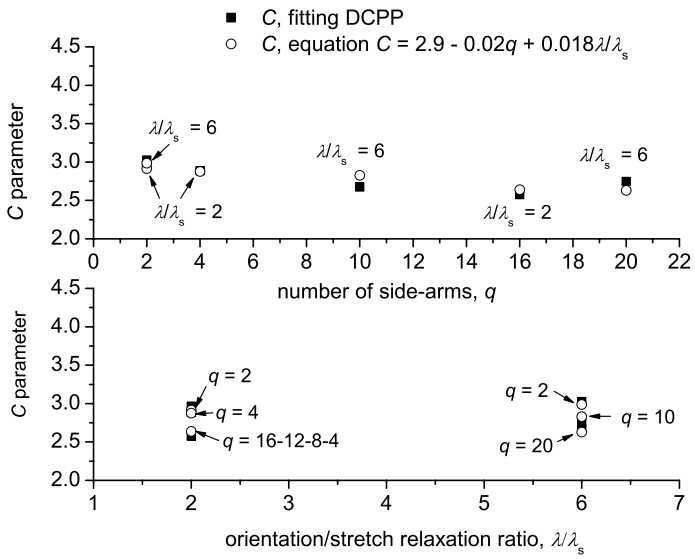

Figure 4.52: *Comparison between parameter C values derived from fitting predicted $I_{3/1}(\gamma_0)$ and empirical descriptive eq. 4.6. Both q_i and λ_i/λ_{si} are varied in all cases.*

4.3.2 Normal forces in LAOS flow simulation

As discussed above, from the LAOS flow simulation using the DCPP model the extra-stress tensor components can be predicted for the modelled polyethylenes. From T_{11} - T_{22} (or T_{xx} - T_{yy}) the first normal stress difference, N_1 is calculated. The predicted (and measured if experimentally possible) N_1 can be a promising quantity for discriminating branched topologies [Graham 01] and is investigated within this chapter. An example of the predicted N_1 during LAOS, for two LCB polyethylenes modeled via the DCPP, is shown in fig. 4.53.

The predicted shear stress is also shown in fig. 4.53 for both polyethylenes. The discrimination between the two LCB samples modeled via DCPP is more pronounced when studying the normal forces, even for a small change of the side-arms parameter q. One can differentiate between the two topologies using the N_1 time data, or the intensity of the higher harmonics from the corresponding FT spectrum. Three spectra for the studied samples are given in fig. 4.54, with a peak at 0 Hz (as expected due to the time data offset) and the highest harmonic at $2\omega_1/2\pi$ as predicted for normal forces in LAOS flow [Owens 02]. The intensity of the peaks at even multiples of the excitation frequency is similar for the two LCB materials modelled by DCPP. However, the intensities for the case of a linear PE as modelled with the DCPP are significantly lower, demonstrating the applicability of N_1 time data from LAOS

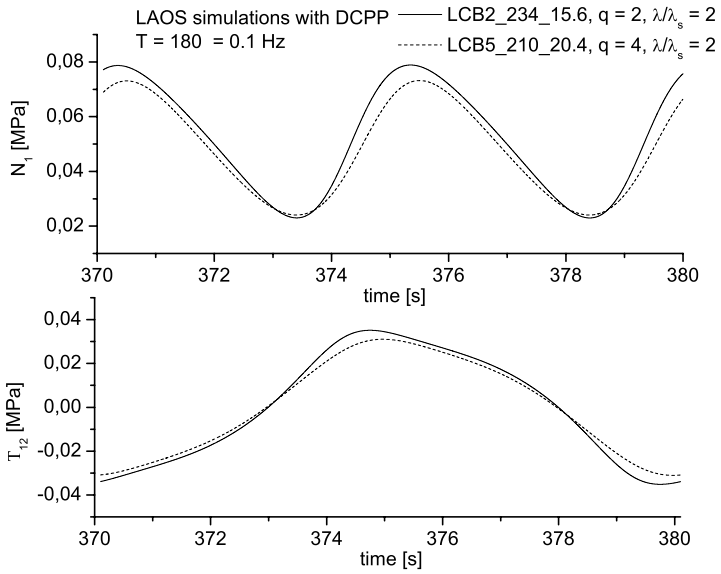

Figure 4.53: *Predicted first normal stress difference for two LCB PE with different q_i and λ_i/λ_{si} DCPP parameters. LAOS flow simulation is with $\omega_1/2\pi$ = 0.1 Hz, γ_0 = 5 and T = 180 °C. Predicted shear stress T_{12} also shown.*

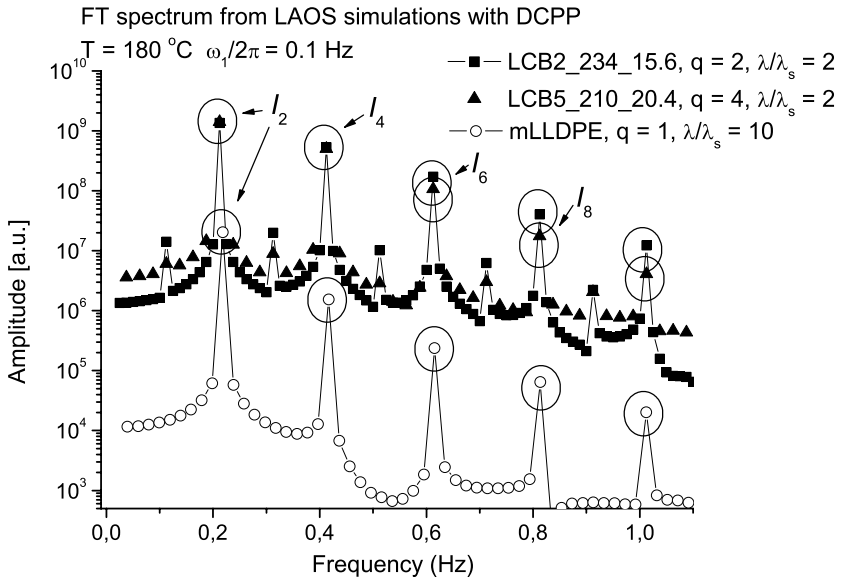

Figure 4.54: *FT-spectra for the first normal stress difference, predicted for two LCB PE with different q_i and λ_i/λ_{si} and a linear PE as modelled via the DCPP. LAOS flow simulation is for γ_0 = 10.*

as a potential parameter for discriminating linear and branched polyethylenes, in agreement with Graham et al. [Graham 01].

4.4 Summary on experimental FT-Rheology and LAOS simulations for linear and LCB industrial PE

Within this chapter, the rheological behaviour of linear and long-chain branched polyethylenes in the non-linear rheological regime is investigated for the case of pure materials and linear/LCB PE blends and for a broad range of deformations via FT-Rheology. The effects of topology, molecular weight and molecular weight distribution are correlated to the relative intensity $I_{3/1}$ and phase, Φ_3 of the resulting third harmonic obtained in LAOS experiments. Long-chain branched polyethylenes exhibit higher non-linearities than linear polyethylenes of similar molecular weight and molecular weight distribution. In the case of linear topology, $I_{3/1}$ is found to increase with increasing M_w and *PDI*. The van Gurp-Palmen method is extended by including the phase of the third harmonic, Φ_3^0, extrapolated at zero strain amplitude. The quantity Φ_3^0 is found to be sensitive to the presence of LCB. Consequently, the samples are categorized into linear and LCB using the measured Φ_3^0 in the extended van Gurp-Palmen plot. With this phase analysis a separation between the effects of LCB and molecular weight distribution in the non-linear rheological response is achieved.

Additionally, the optimum experimental conditions for differentiating linear and branched polyethylenes using LAOS and FT-Rheology are investigated. Polyethylenes have low activation energy and therefore a rather weak temperature-dependence. Thus, strain sweep is a more appropriate test method for studying the non-linear rheological behaviour of these samples, with the current experimental setup. Experimental FT-Rheology is optimized with respect to the sensitivity towards LCB. The optimum conditions are found to be around: T = 180 °C, $\omega_1/2\pi$ = 0.1 Hz, with γ_0 = 0.5 and γ_0 = 3. Polyethylenes containing LCB are found to produce higher non-linear behaviour at low frequencies and at conditions corresponding to higher tan δ values in the linear spectrum (flow region).

Although the minimum detected LCB and SCB degree via FT-Rheology is quite low, 0.1 LCB + SCB /1000 CH_2 as estimated from ^{13}C melt-state NMR, the information about the structure of the industrial PE samples is not complete. The above estimation is an average of the branching of all chains in the melt. However, one needs to know what fraction of the macromolecules are branched in a melt, which is polydisperse with respect to molecular weight and topology. Additionally, it is useful to determine at which minimum amount the LCB chains influence the rheological properties of PE. Thus, the limits and sensitivity of FT-Rheology towards presence of LCB chains in a material need to be investigated. Since no monodisperse model polyethylene sample with known LCB/1000 CH_2 and type of LCB (combs, H-shaped, pom-pom, tree-like branching) is available, well-characterized industrial

linear PE blended with LCB PE, of known branching content, at different known ratios are studied. The blended components have either similar narrow (mPEmix) or similar broad (Lmix) molecular weight distribution and a similar SCB type. Thus, by applying LAOS and FT-Rheology the effect increasing concentration of the LCB component, specifically the ratio of LCB to linear chains in the polydisperse melt, is probed.

From oscillatory shear measurements in the linear regime one can clearly detect the presence of LCB in the melt for LCB polyethylene concentrations $>$ 30 wt %. However, the goal is not only to present a more sensitive method for detecting LCB, but additionally to obtain information about the non-linear behaviour of PE with varying topology. Hence, LAOS is applied with strain sweeps in a fixed excitation frequency (0.1 Hz) and temperature (180 °C), along with frequency sweeps at low strain amplitude (γ_0 = 0.5) for studying $\Phi_3^0(\omega)$. The analysis with FT-Rheology shows that LCB PE component of a concentration as low as 5.5 wt % in a linear melt and a linear component of weight fraction as low as 5.5 wt % in a LCB polyethylene sample, can be clearly differentiated and are adequate to change effectively the non-linear rheological properties of the material.

Furthermore, the quantities used to quantify the non-linear behaviour of the polyethylenes, $I_{3/1}(\gamma_0)$, $\Phi_3(\gamma_0)$, Φ_3^0, as well as the parameters derived from fitting the sigmoidal $I_{3/1}(\gamma_0)$ (*A*, *B*, *C*, *D* in eq. 1.47 and 1.51), increase monotonically with increasing concentration of LCB species, demonstrating the dependency of the non-linearity on the topology of polymers, specifically polyethylene. Parameters *A*, *B* and *D* are found to increase monotonically with increasing LCB content, which confirms the fact that they are functions of topology and i.e. relative branching degree (per chain) as well as relative amount of branched species in a melt with linear PE, molecular weight and molecular weight distribution.

Finally, the miscibility and stability of the blends is investigated by means of rheological techniques, already presented by other authors [Kwag 00, Han 87]. The storage and loss viscosity, as well as the storage and loss moduli, as measured in the linear regime, are analyzed for the purpose of assessing the miscibility of the studied blends. Additionally the complex modulus and the non-linearity of the blends under LAOS for more than 2h are recorded. Taking into consideration the results from rheological tests of miscibility of the blends (Cole-cole plots, G'' vs. G' plots and mixing rules), we are confident that they are miscible. No phase separation takes place. The only property that varies in the blends and results in increasing non-linearity ($I_{3/1}(\gamma_0)$) with higher phases ($\Phi_3(\gamma_0)$, Φ_3^0) is the LCB/linear chains ratio.

The non-linearity change with increasing deformation is correlated to the molecular parameters of a “pom-pom” blend, specifically the number of arms and the ratio of orientation-to-stretch relaxation times. We achieve this by performing LAOS simulations with the DCPP model. In order to extend our study of LAOS flows for different polymer topologies with the DCPP, model samples such as H-shaped, combs, or tailor-made “pom-pom” polyolefines are needed in combination with blended linear and branched structures. However, FT-Rheology using a constitutive equation based on molecular architecture enables

the qualitative prediction of non-linear behaviour for LCB polymers.

Graham et al. [Graham 01] state that extensional flows are more discriminating for nonlinear stretch characteristics and a more sensitive way to determine stretch characteristic times in Pom-pom model. This difference from shear flows lies in the measured stress tensor component and the orientation way of molecules. The authors suggest that the first normal stress difference in exponential shear could be a more sensitive quantity to use for stretch and orientation of the pom-pom macromolecule determination. This motivates numerical simulations of polymers with varying topology, as quantified by the molecular structure related parameters of the DCPP model, on the resulting normal stress difference, N_1, during a modelled LAOS flow. This promising method can be extended experimentally by accurately measure the normal forces during a LAOS experiment, especially for the samples studied in chapters 3 and 4, for which normal forces are already observed to be prominent due to their high molecular weight. However, the experimental equipment needed to conduct these type of measurements are not yet available.

Chapter 5

Investigation of flow instabilities via FT-Rheology

5.1 Experimental and theoretical studies of flow instabilities in polymers-short literature review

Flow instabilities are time-dependent phenomena occuring in flows which are supposed to be in steady-state. For example, a time-dependent shear stress response of a material under application of a steady shear strain, or oscillations in pressure drop of a polymer melt during capillary flow under constat inflow rate. Instabilities in viscoelastic flows are of great practical importance and therefore a subject of significant and growing interest for rheologists in the last decades [Graham 95, Hatzikiriakos 91, Larson 92]. Industrial important materials such as polyethylene (LDPE and HDPE), present flow distortions and surface features like sharkskin (small irregular distortions on surface, roughness), or more extreme, for example gross fracture and helical extrudate distortions, during capillary flow or extrusion (see fig. 5.1). The above occurring flow distortions are not only distinguished and quantified by the appearance of the extrudate (both amplitude and periodicity of surface oscillations), but additionally by the critical conditions for the onset of these instabilities and the flow characteristics, e.g. critical shear rate for sharkskin or stick-slip during capillary flow.

The investigation of such phenomena that occur during polymer flow can lead to the development of a robust method to control the quality of extruded products. Additionally, understanding the mechanisms behind the onset and development of flow instabilities can provide us with a valuable insight in the polymer melt dynamics and allow further polymer processing optimization. Whether these flow distortions are constitutive, or driven by melt elasticity, molecular structure, surface properties, flow geometry or a combination of the above is yet to be fully understood and answered. Explanations proposed for extrudate distortions include concepts of adhesion failure of the polymer to the die wall, referred

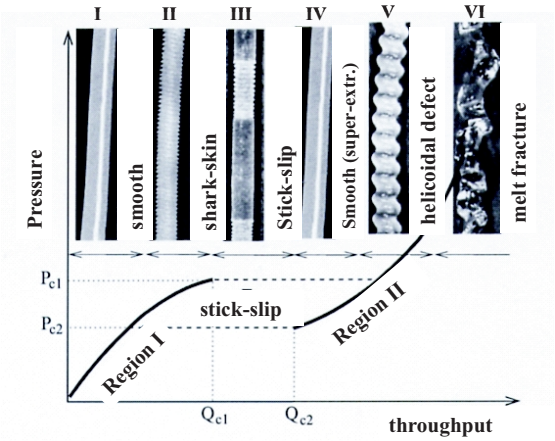

Figure 5.1: *Typical flow curve for a polyethylene melt and regions of instabilities.*

to as wall slip, and/or mechanical failure of the material itself, referred to as constitutive instabilities [Larson 92, Wang 96b]. The first phenomenon can be modeled by replacing the boundary condition of a vanishing wall velocity (no-slip condition) with a finite value that depends on wall shear stress and/or strain history of the fluid [Pearson 68]. On the other hand, a constitutive instability occurs when the relationship between shear stress and shear-rate is non-monotonic [Larson 92]. However, it is difficult to distinguish experimentally between the two origins of the instabilities, due to the fact that both result in the same macroscopically observed effects.

Capillary and extrusion flows are not the only cases where instabilities might occur. It is generally accepted that instabilities may occur in parallel plate or cone-plate shear flow [Larson 92], for example meniscus distortions as seen in fig. 5.2. This phenomenon is often observed for polymers even at low Reynolds numbers (*Re*) with negligible inertia effects. Larson actually separated the distortions into irregular non-axisymmetric “vortexes” and axisymmetric indentations of the meniscus or edge fracture [Larson 92]. One different abnormality that can possibly occur is the elastic instability, in which a meniscus distortion is not an essential feature. This instability is generally observed in Boger fluids, i.e. dilute or moderately concentrated solutions of high molecular weight polymers. There are evidence that the instability phenomena are related to a radial driving force created by the first normal stress difference (N_1) in a curvilinear shearing flow [Larson 92].

Since polymer melts subjected to LAOS may exhibit complicated nonlinear periodic responses related to meniscus distortions and wall slip [Chen 94, Larson 92], this flow presents a practical way for studying the dynamics of instabilities and the effect of rheological properties with high sensitivity. Additionally, LAOS experiments can provide predictions for the performance of the investigated melts in a capillary flow and can connect structure to processability. Henson and Mackay [Henson 95] studied slip effects of monodisperse polystyrene melts (with M_w = 49 kg/mol, 104 kg/mol, 198 kg/mol and 392 kg/mol) and found that all

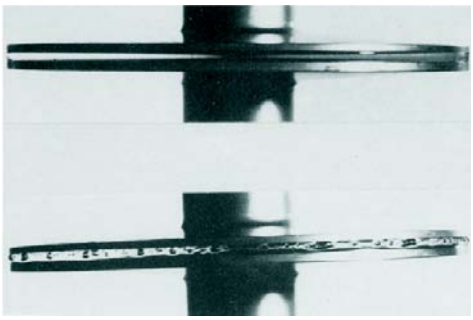

Figure 5.2: *Photographs of polymer solution at two shear rates in a cone-plate rheometer with radius = 50 mm and angle 2.3°. For $\dot{\gamma}$ = 1.58 s^{-1} the fluid surface is smooth and for $\dot{\gamma}$ = 158 s^{-1} meniscus distortions are observed. Adapted from Kulicke et al. [Kulicke 79]*

exhibit slip behaviour. They discussed three possible models to describe slipping of polymer chains: (1) the adsorbed layer, (2) the disentangled layer and (3) the true slip model, and used a parameter *b*, introduced by de Gennes [deGennes 85] to quantify the slip phenomenon. This parameter corresponds to the extrapolated distance to zero velocity in a parallel plate flow and is comparable to the average thickness of a polymer melt droplet during spreading on a smooth wall. According to this model, a liquid flowing over a smooth solid wall will display a length b comparable to the molecular size, d [deGennes 85]. The slip velocity is then given by:

$$v_s = \frac{d}{\eta_M}\sigma_w \tag{5.1}$$

where *d* is a length of molecular dimensions, η_M is the shear viscosity of a liquid of monomers (with the same interactions, but no entanglements) [deGennes 85]. The wall shear stress is given by σ_w. For the linear viscoelastic regime eq. 5.1 can be written as follows:

$$v_s = \frac{d}{\eta_M}\eta_0\ \dot{\gamma}_w \equiv b\ \dot{\gamma}_w \tag{5.2}$$

where η_0 is the zero-shear viscosity of the polymer. From the reptation theory, the relation between monomeric liquid viscosity, η_M, and polymer melt viscosity is, $\eta_0 = \eta_M \frac{N^3}{N_e^3}$, where N is the number of monomers per chain and N_e the number of monomers between two entanglements. The true wall shear rate is $\dot{\gamma}_w$. This true wall shear rate in a parallel plate geometry with a gap of *H*, and the upper plate moving with a velocity ωR is given by [Henson 95]:

$$\dot{\gamma}_w = \frac{\omega R}{H + 2b} \tag{5.3}$$

The torque for a shear flow between to parallel moving plates of radius *r* is known:

$$M = 2\pi\eta_0 \int_0^R \dot{\gamma}_w \, r^2 dr \tag{5.4}$$

where *R* is the maximum plate radius. Combining eq. 5.3 and 5.4 and integrating we obtain the nominal wall shear stresses ($2M/\pi R^3$) at the gap *H* and at infinite gap, σ_N and $\sigma_{N\infty}$, respectively. Hence the ratio of the stresses will be as follows:

$$\frac{\sigma_N}{\sigma_{N\infty}} = 1 + \frac{2b}{H} \tag{5.5}$$

Henson and Mackay [Henson 95] used eq. 5.5 to quantify slip in the monodisperse polymer melts and made the needed adjustments and approximations to import in this model the three different concepts mentioned above. All studied melts were found to exhibit slip behaviour during oscillatory shear in parallel plate geometry. In the linear regime, the slip velocity was found to be proportional to the shear rate. This proportionality was related to the molecular weight with a power index of ∼1.1. This experimental result is not consistent with the theory of de Gennes since $b \propto \eta_0 \propto M_w^3$. The authors attributed this deviation to lack of data (only three PS melts studied) which may have caused errors in determining b. A study of wall slip for concentrated high molecular weight PS (M_w = 109×10^3 kg/mol and 289×10^3 kg/mol) was presented by Reimers and Dealy [Reimers 98]. The authors quantified nonlinear viscoelasticity using step-strain experiments, LAOS, FT-Rheology and birefringence measurements. Although they state that the instable behaviour at a high shear stress is due to wall slip, it was suggested that the polymer does not loose adhesion. A more plausible hypothesis according to the authors, is a change in interaction between adsorbed molecules and bulk polymer chains of the solution above a critical stress value. Large amplitude oscillatory shear was indeed used, to reveal the dynamics of slip, since stress exceeds the critical slip value for brief periods of time. High non-linearities were observed in the LAOS response and quantified via FT-Rheology. The results demonstrated the dynamic nature of slip and the resulting intensities and phases of the higher harmonics were found to be sensitive to molecular weight. Chen et al. [Chen 94] investigated fracture and flow instabilities in a parallel plate rheometer for PS melts (with M_w = 10 kg/mol, 13 kg/mol, 32 kg/mol, 184 kg/mol and 233 kg/mol) and solutions by LAOS, and discussed three possible reasons for the recorded wave forms, namely: (1) viscous heating, (2) constitutive instability and (3) cohesive/adhesive failure. They conclude that high non-linearities in LAOS signals cannot be caused by viscous heating, however they can be attributed to a combination of both constitutive instabilities and polymer-surface adhesive failure. Graham [Graham 95] modelled the nonlinear dynamics of LAOS and suggested that both viscoelasticity and

dynamic slip are necessary to explain the instabilities of polymer melts under oscillatory shear. The author related complicated non-periodic response in LAOS with exhibited wall slip and suggested that both fluid elasticity and a dynamic slip (or a certain memory in the instability), are necessary for a non-periodic stress response to be observed.

The wall slip of HDPE melts in sliding plate and capillary geometries was extensively investigated by Hatzikiriakos and Dealy [Hatzikiriakos 91, Hatzikiriakos 92a, Hatzikiriakos 92b]. A sliding plate rheometer has the advantage of absence of pressure gradient and entrance effects from the flow, as well as the convenient modification and control of the polymer-wall interface. Utilizing capillary flow measurements, the critical shear stress for slip occurrence of the particular HDPE resin (M_w = 177.8 kg/mol, *PDI* = 9.4) was found to be 0.09 MPa. They observed a clear dependence of slip velocity on shear stress using the Mooney method [Mooney 31]. By repeating the measurements at different temperatures a dependence of the slip velocity on temperature was revealed. From the analysis of the slip velocity as a function of shear stress in a capillary flow, the following relation was extracted to describe the phenomenon:

$$\begin{aligned} v_s &= 0, \quad \sigma < \sigma_c \\ v_s &= \alpha\sigma^m, \ \sigma > \sigma_c \end{aligned} \tag{5.6}$$

where σ_c is the critical shear stress defined as the onset of melt slip. For stresses lower than σ_c, the slip velocities, as determined by extrapolating eq. 5.6 to lower stress values, were found to be approximately zero. The slip coefficient, α, was found to be a function of temperature. The derived values for the exponent *m* were ~ 3 [Hatzikiriakos 91]. The authors repeated the experiment with surfaces coated with fluorocarbon spray, used the $v_s = \alpha\sigma^m$ equation to fit the resulting stress and a dependence of α was found on the interface conditions. However, no changes were recorded for the exponent *m* (the slope of v_s versus σ in the log-log plot was not significantly changed).

The polyethylenes were additionally exposed to LAOS flow and the resulting shear stress was analyzed. The stress overcame the critical value for short periods of time in every cycle and since a relaxation time is involved in the melt slip process, several cycles were needed for the polymer to slip. Wall slip became apparent by the decrease of the stress amplitude after some cycles. Finally a quasi-steady state was reached after the gradual decrease of maximum stress. The complex stress waveforms were attributed to slip by the following interpretation: Above a critical stress, the polymer looses adhesion with the wall, slip occurs and the stress is decreasing. This nominal stress decrease causes a periodic regain of adhesion and stress increases again. The authors separated the different types of LAOS signals into four categories for increasing number of cycles: (a) non-sinusoidal due to non-linear viscoelasticity of the melt, (b) decrease in stress amplitude due to slip presence

for non-sinusoidal signals, (c) increasing non-sinusoidal and asymmetric character of the stress as for an elastic Bingham fluid in Yoshimura and Prud'homme [Yoshimura 87] and finally, (d), further distorted signals resembling chaotic systems, where stress exhibits an aperiodic deterministic behavior which is very sensitive to initial conditions [Thompson 87]. The LAOS stress waveforms were correlated also with the deformation history and rest time between experiments and a strong dependence on the initial conditions is found for the recieved waveforms. The slip phenomenon is often empirically modelled by an algebraic relationship between slip velocity, v_s (non-vanishing fluid velocity at the wall), and shear stress, σ [Graham 95, Hatzikiriakos 91, Henson 95, Larson 92]:

$$v_s = f(\sigma) \tag{5.7}$$

Equation 5.6 is valid under the assumption that the slip velocity adjusts instantaneously to the wall shear stress. However, Lim and Schowalter [Lim 89] suggested that the transition from the slip to the stick condition was gradual and showed characteristics of a relaxation process. Thus, to account for this experimental observation a "memory slip model" was introduced by Hatzikiriakos and Dealy and [Hatzikiriakos 92a]:

$$v_s + \lambda_{slip}\, \dot{v}_s = f(\sigma) \tag{5.8}$$

where λ_{slip} is a relaxation time for slip and the slip velocity is a nonlinear function f of the stress history. Combining eq. 5.8 with 5.6 one derives a phenomenological equation used to study also exponential and oscillatory shear [Hatzikiriakos 91]:

$$v_s + \lambda_{slip}\frac{dv_s}{dt} = \alpha\sigma^m \tag{5.9}$$

For steady shear the second term on the left hand of the eq. 5.9 is zero and eq. 5.6 is recovered. The validity of the above equation was examined by observing slip in exponential shear flow. In this particular study [Hatzikiriakos 91], the "slip relaxation time", λ_{slip}, was determined from exponential shear experiments between 0.20 s and 0.25 s.

Furthermore, the resulting stress time signal from LAOS experiments was compared to the one theoretically predicted via the combination of eq. 5.9 with a constitutive model, in particular a Maxwell model. For the eq. 5.9, slip parameter, α, was taken as a simple time function (assumption of a linear proportionality, α = 0.0625*t*) to cope for the time-evolution

of the slip with increasing number of deformation periods. This empirical model was found to qualitatively predict stress signals observed in LAOS experiments. Finally, a dependence of the critical shear rate for unstable LAOS flow on excitation frequency was found. In a later study [Hatzikiriakos 92b] the same authors used the following function to determine α:

$$\alpha = \xi f_1(T) f_2(\sigma_n/\sigma_w) \tag{5.10}$$

where ξ is a constant depending on polymer molecular structure. The function f_1 including the temperature dependence was found to be well approximated by the WLF equation (eq. 1.19). Finally f_2 is a function of σ_n and σ_w, which are the normal and wall stresses respectively. From modeling capillary flow of HDPE/LDPE blends, the authors concluded that the critical wall stress for slip, σ_c, depends on the average molecular weight of the polymer and the polydispersity [Hatzikiriakos 92a]. The above model for slip using eq. 5.8 can be combined with any constitutive equation relating shear stress and deformation. Graham [Graham 95] applied the Maxwell model and the White-Metzner. For the latter model, the viscosity as a function of shear-rate is given by the Carreau equation. Equation 5.8 combined with a constitutive equation for stress consist a system with two dependent variables, σ_s and v_s. If however, in eq. 5.8 the relaxation process is neglected, the above equation takes an algebraic form and periodic behaviour can be predicted. This is not the case for a Newtonian fluid, thus both fluid elasticity and dynamic slip are necessary for non-periodic response [Chen 94, Graham 95]. Graham indeed predicted LAOS signals for various combinations of *De* and parameters for the function f(σ) [Graham 95]. At high strains harmonics at even multiples of the excitation frequency ($2\omega_1$, $4\omega_1$,...etc.) were predicted in the FT-spectrum. Finally it was stated that quantitative reproducibility of particular chaotic behaviour in LAOS is impossible, due to the sensitivity towards the initial conditions, which is in agreement to the experimental findings in the present work (e.g. fig. 3.7 and 3.11).

The concept of a relation between molecular structure and sharkskin was discussed by Allal et al. [Allal 06] following the work of Wang et al. [Wang 96b]. Several models were discussed for the formation and propagation of surface flow distortions during capillary extrusion of molten polymers. Most relevant to the present work is the concept of an existing critical shear rate for the onset of sharkskin formation, which has a temperature dependence that can be described by the WLF shift factors and increase with increasing polydispersity and/or temperature. Allal et al. assumed a critical shear rate inversely proportional to a characteristic relaxation time for extrudate distortions. Wang et al. suggested that this characteristic time is of the same order of magnitude with the terminal relaxation time. Subsequently, Allal et al. suggested that this time can correspond to the tube renewal time, as determined by Graessley [Graessley 82] and using this time they derived an equation for the critical shear rate for sharkskin onset of the following type: $1/\ \dot{\gamma}_c = d[M_w/M_e]^n$, with n = 4.3 for polydisperse PE. The prefactor d was determined in terms of molecular characteristics,

however no further explanation is provided on the theoretical background of this equation.

5.2 Motivation for studying flow instabilities via FT-Rheology

From the analysis of LAOS flow for the studied PS and PE melts in chapters 3 and 4, evidence of slip and flow instabilities are observed at large strain amplitudes. The recorded stress signals at γ_0 above a critical value present a decaying amplitude or lost periodicity, where the non-linear contributions become a function of time (e.g. fig. 3.16, 3.11). Thus, it is important to detect instabilities during polymer LAOS and discriminate their effect on FT-Rheology results from the non-linearity of the material due to structural properties (e.g. LCB). In the following paragraphs the validity of the above considerations is examined for polystyrene and polyethylene melts of various molecular weights and distributions (see Tables 3.1 and 4.1). The effect of M_w, PDI and branching content on $\gamma_{0,critical}$ for slip onset in LAOS is examined and additionally, the influence of surface type and geometry on $I_{3/1}$, $I_{2/1}$ and Φ_3 is studied. The relation of topology and specifically of branching with the onset and development of extrudate distortions during capillary flow for the PE samples is also derived, along with the correlation with FT-Rheology results for the material non-linearity. Simulations are also performed for LAOS including slip boundary conditions and some preliminary results for capillary flow simulation are presented. In this numerical study of flow instabilities, the slip equation proposed by Hatzikiriakos and Dealy [Hatzikiriakos 91] as given in eq. 5.9, is incorporated in the LAOS flow model and the resulting non-linear rheological behaviour is analyzed via FT-Rheology.

5.3 Flow instabilities in LAOS for polystyrene linear melts

Experimental examples of decaying stress amplitude are already presented for a polystyrene melt (chapter 3, fig. 3.16). The majority of the studied samples present LAOS signals for γ_0 larger than $\gamma_{0,critical}$, that can belong to the four categories mentioned by Hatzikiriakos and Dealy [Hatzikiriakos 91] (decaying amplitude, loss of periodicity). However, it must be noted that for samples of low molecular weight, typically $M_w < 100$ kg/mol for monodisperse melts, the torque signal starts to decay or looses its periodicity for large strain amplitudes which are inaccessible with the ARES rheometer. In fig. 5.3 and 5.4 the regions of non-linear viscoelastic unstable behaviour are presented for two polystyrenes, as monitored via $I_{3/1}(\gamma_0)$ and $\Phi_3(\gamma_0)$.

As a result of asymmetry in the stress signal, even harmonics may occur indicating unstable flow, in agreement with Graham [Graham 95]. Specifically, the relative intensity of

the 2^{nd} harmonic, $I_{2/1}$, is well above the noise level for deformations where instabilities take place, as seen in fig. 5.5 for the two linear polystyrene melts at 180 °C.

The 2^{nd} harmonic is reproducible and its presence is attributed to the instabilities oc-

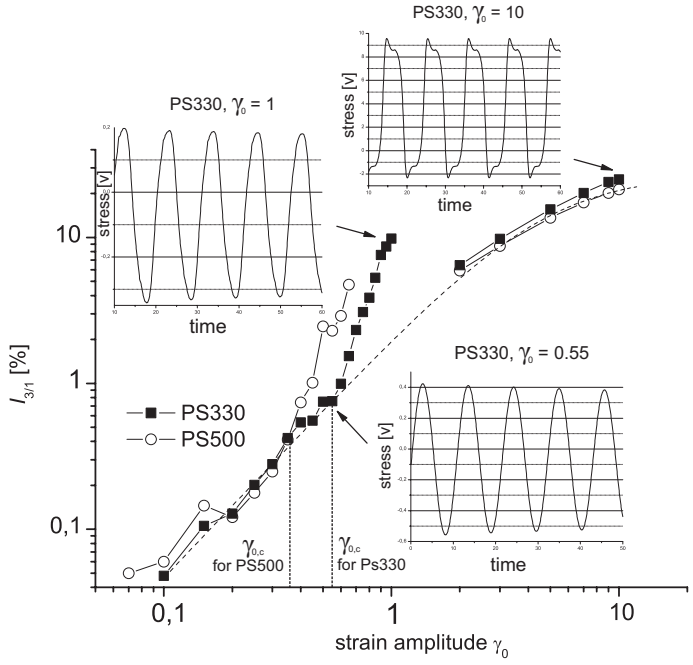

Figure 5.3: *Observed types of LAOS stress signals and $I_{3/1}(\gamma_0)$ for linear polystyrenes PS330 and PS500. Measurements with strain amplitude $\gamma_0 \geq 2$ are performed with the RPA2000. $I_{3/1}$ up to γ_0 = 1 (ARES data) shifted to correspond to cone-plate measurements of RPA2000. Dashed-line represents a fit of $I_{3/1}(\gamma_0)$ with eq. 1.47.*

curring during the LAOS flow. There is a possibility that even harmonics result from an imperfectly applied sinusoidal strain, due to inaccurate motor control. However, within this work, this factor is insignificant since FT analysis on the applied strain signal reveals no higher harmonics in the spectrum of the applied strain (intensities are below noise level).

An increased polydispersity has a significant effect in the resulting instabilities as monitored via $I_{2/1}$. The results from the linear binary blends are presented in 5.6. The relative intensity of the 2^{nd} harmonic increases dramatically with an increase in polydispersity. The presence of large macromolecules in a melt influences the even harmonics, in a way similar to $I_{3/1}$ (e.g. fig. 3.8). This outcome reinforces the argument that large macromolecules in a melt dominate the non-linear response, as demonstrated in chapters 3 and 4. The critical strain amplitude for the instabilities onset is lower and the resulting $I_{2/1}$ is larger for high molecular weight materials.

The temperature dependence of the flow instabilities is studied by repeating the experiments at higher and lower temperatures, i.e. T = 200 °C and T = 140 °C. High temperatures are already found to suppress the flow distortions in capillary flow [Allal 06, Hatzikiriakos 92a,

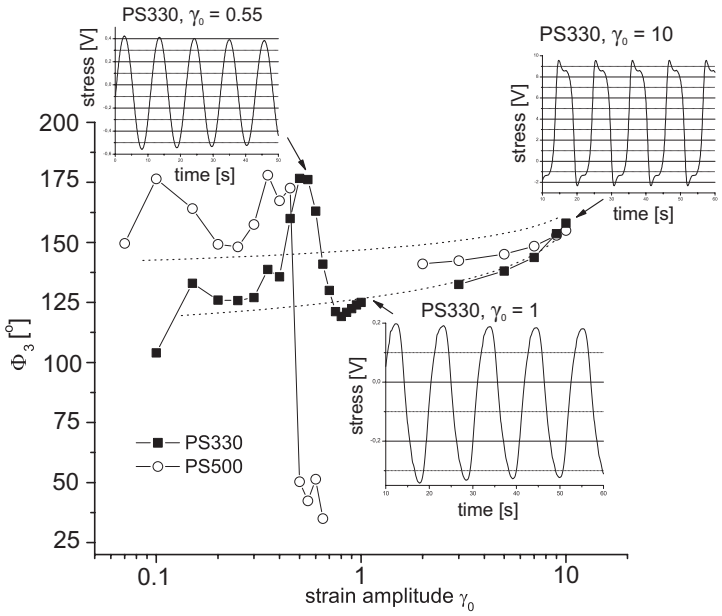

Figure 5.4: *Stress signals and $\Phi_3(\gamma_0)$ obtained for linear polystyrenes PS330 and PS500. The resulting $\Phi_3(\gamma_0)$ is sensitive to the onset of stress amplitude decay and asymmetry. Measurements at strain amplitude $\gamma_0 \geq 2$ are performed with the RPA2000. Lines are guides to the eyes.*

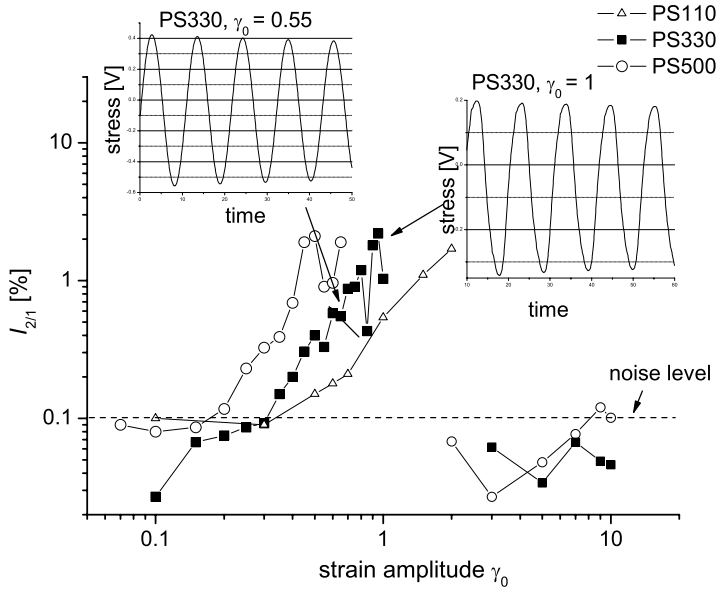

Figure 5.5: *Experimentally detected $I_{2/1}(\gamma_0)$ for PS110, PS330 and PS500, at T = 180 °C and $\omega_1/2\pi$ = 0.1 Hz. Measurements with strain amplitude $\gamma_0 \geq 2$ are performed with the RPA2000.*

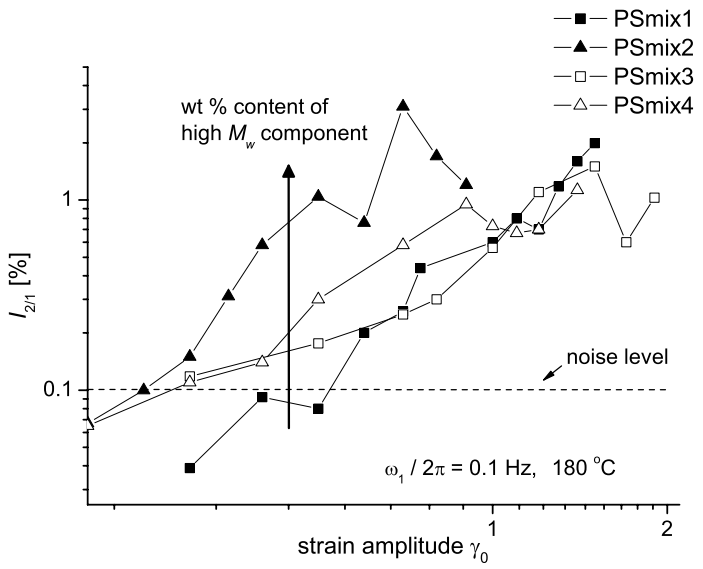

Figure 5.6: *Experimental $I_{2/1}(\gamma_0)$ for binary blends. Occurring instabilities are higher for blends with increased content of high molecular weight samples. Blend composition can be seen in Table 3.2*

Hatzikiriakos 92b]. If the argument that slip parameters have a WLF dependence on temperature is accepted, as suggested by Hatzikiriakos and Dealy [Hatzikiriakos 92b], then the recorded non-linearities in LAOS should be lower for a higher temperature. However, both the odd and even higher harmonics decrease with increasing temperature and increase with molecular weight. In fig. 5.7 the resulting intensity of the 3^{rd} harmonic is depicted for several linear polystyrene melts at 200 °C. A clear decrease of the resulting higher harmonics is indeed observed when increasing the temperature. Furthermore, if the sample is subsequently cooled down to 180 °C and the test is repeated, the material recovers its non-linear character and the resulting intensities are close to the values initially recorded. As expected, the dependence of the $I_{3/1}$ on the molecular weight distribution is conserved also at higher temperatures, where higher $I_{3/1}(\gamma_0)$ are found for linear melts of higher M_w and *PDI*.

5.3.1 Effect of flow geometry and surface type on LAOS instabilities

In this paragraph, the correlation between the onset and development of flow instabilities and the conditions of LAOS flow is examined, i.e. the surface type (steel, aluminium, fluorocarbon coated, grooved surface) and the geometry used (plate diameter and gap). The sample used is PS330, a linear polystyrene melt. Large amplitude oscillatory shear strain sweep tests are performed for PS330 using steel parallel plates with diameters of 8 mm, 13 mm and 25 mm

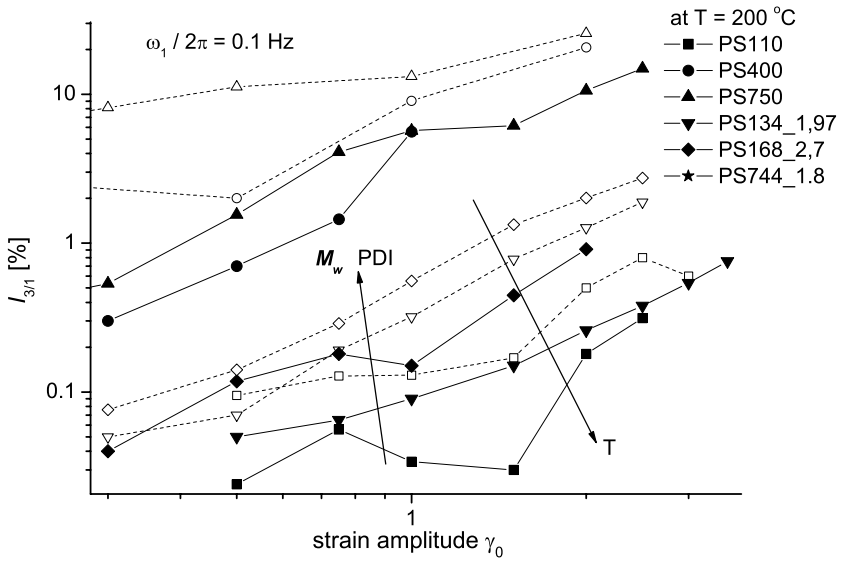

Figure 5.7: *Resulting $I_{3/1}(\gamma_0)$ for several linear polystyrene melts at T = 200 °C. Comparison with results for T = 180 °C (open-symbols with dashed lines).*

and the resulting non-linear response is analyzed with respect to the relative intensities of the 2^{nd} and 3^{rd} harmonic and the relative phase, Φ_3. As mentioned in chapter 3, all disk samples are prepared with the same procedure and no detectable degradation takes place during the measurement.

In fig. 5.8 it is shown that the plate diameter has no significant effect on the onset and development of unstable LAOS flow. However, by changing the plate material from steel to aluminium, the onset of slip is observed at lower critical strain amplitude, $I_{3/1}$ is slightly higher and $I_{2/1}$ is significantly increased. When the gap between the plates is approximately doubled, the sample behaves highly non-linear at lower strain amplitudes, in comparison with the case of a 1 mm gap. Highly asymmetric stress signals are recorded, due to the onset of secondary flows, outflow, edge fractures and generally meniscus distortions even for relatively small deformations, as indicated from the resulting FT-spectrum data (fig. 5.9).

Subsequently, the surface type is altered. In order to reinforce the slip effect, a layer of polyfluoro-1,3-dimethylcyclohexane (PFDMCH) is created on the surface of aluminium plates by chemical vapor deposition. The estimated thickness of the polymerized substance is in the order of 0.1 μm. In this altered surface the polymer melt is supposed to loose adhesion at smaller strain amplitudes, compared to a metal plate surface. Indeed, higher non-linearities are observed for strain sweeps of PS330 using these fluorocarbonated surfaces. The evidence of flow instability onset, namely a sudden slope change in $I_{3/1}(\gamma_0)$ (deviation from predicted sigmoidal curve), an increased $I_{2/1}(\gamma_0)$ above the noise level and a local maximum in the

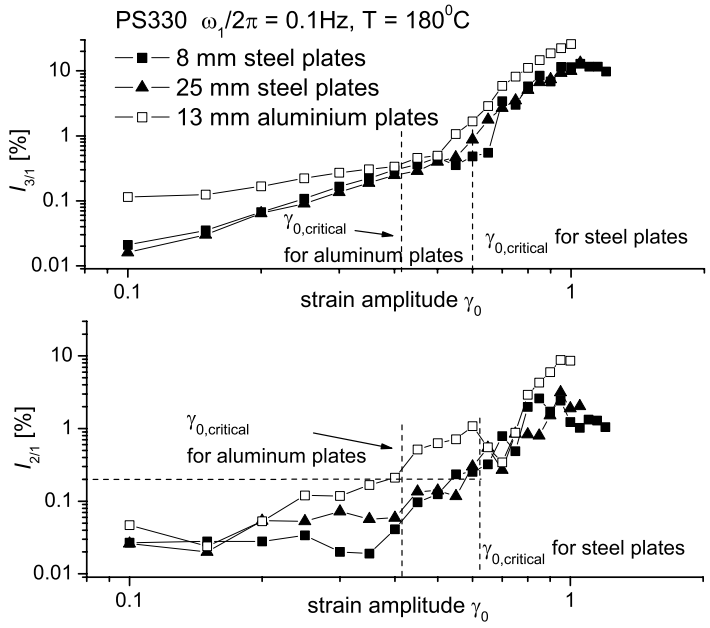

Figure 5.8: *Effect of plate diameter and material on flow instabilities as monitored via FT-Rheology at T = 180 °C, for a linear monodisperse polystyrene melt with M_w = 330 kg/mol.*

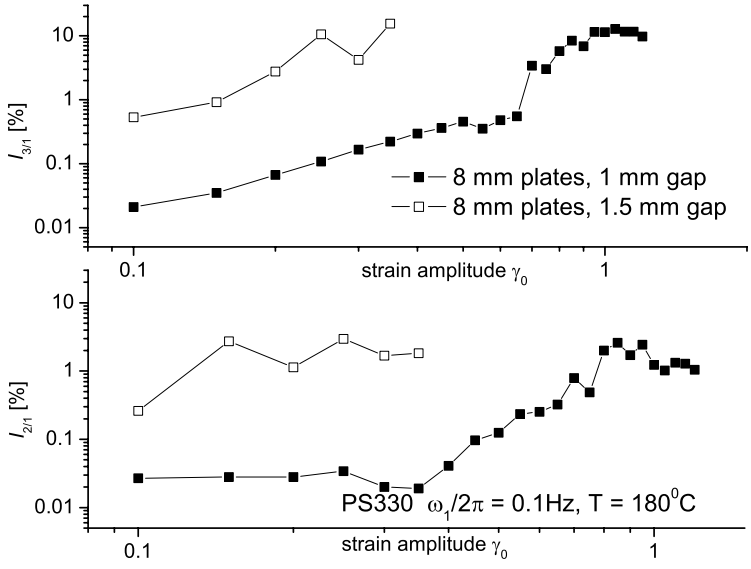

Figure 5.9: *Effect of sample thickness on flow instabilities as monitored via FT-Rheology at T = 180 °C, for a linear monodisperse polystyrene melt with M_w = 330 kg/mol, measured with steel plates.*

$\Phi_3(\gamma_0)$, are observed at lower strain amplitudes ($\gamma_{0,c} \approx 0.4$) for the specific experimental conditions. Furthermore, the resulting non-linearities for $\gamma_0 > \gamma_{0,critical}$ are higher. The measured $I_{2/1}$ for fluorocarbonated surface can be 10 times higher compared to $I_{2/1}$ recorded during strain sweep tests with normal steel surface (see fig. 5.11). One can suggest that the observed non-linear rheological behaviour is the sum of the non-linear viscoelastic character of the material (inherent non-linearity, constitutive instabilities) due to molecular characteristics and the non-linearities caused by the flow type, i.e. non-vanishing wall velocities (wall slip).

A complementary way to modify the flow pattern in order to "fingerprint" the non-linear rheological behaviour of the melts during instable flows is to create grooves, or anomalies on the metal surface, in a controlled manner. A pattern used is shown in fig. 5.10 and compared with the die design of the RPA. In the latter apparatus no decay of the stress time signal amplitude is observed, even at large amplitudes where the non-linearities are extremely high. By applying LAOS in the ARES with a grooved surface geometry it is observed that, on the contrary, the non-linear behaviour is significantly enhanced. One can conclude that grooved surfaces are not sufficient to suppress slippage. However, the flow pattern in an open-rim geometry with large grooves may contain secondary flows and the inherent complexity of the flow can be the reason for the increased $I_{3/1}(\gamma_0)$ and $I_{2/1}(\gamma_0)$, even with the absence of slip. The second factor that is different in the RPA2000 and can lead to a suppression of slippage and flow instabilities is the closed-rim feature and the high pressure applied between the biconical dies (6 MPa). White et al. indeed investigate the effect of pressure in flow instabilities and concluded that high pressure is an effective way to reduce wall slip [White 91].

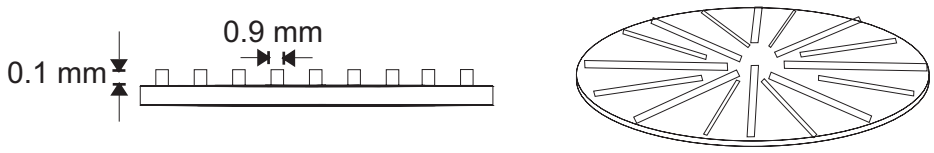

Figure 5.10: *Typical form of grooved plate open-rim geometries. Diameter can be 8 mm or 25 mm and the gap between the plates 1-1.5 mm.*

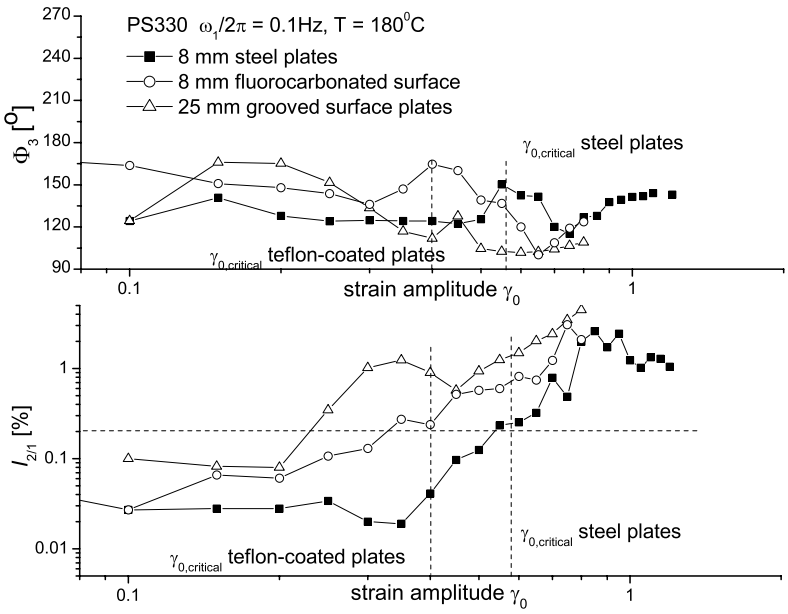

Figure 5.11: *Effect of surface treatment on flow instabilities as monitored via FT-Rheology at T = 180 °C, for a linear monodisperse polystyrene melt with M_w = 330 kg/mol.*

5.3.2 Monitoring the time evolution of slip during LAOS via FT-Rheology

Since the phenomenon of wall slip can possess a time-dependent character, the time evolution can be monitored and analyzed via FT-Rheology. The material is exposed to constant strain amplitude and frequency for a long time. Typically 100 to 200 recorded cycles are adequate. In a strain sweep at T = 180 °C, for the large γ_0, in the case of PS330 ($\gamma_0 > 0.8$), the signal is significantly distorted and extremely high non-linearities are recorded. Afterwards, the sample is subjected in a strain sweep for γ_0 = 0.01 - 2, using the fluorocarbonated surfaces, LAOS is applied with a constant γ_0 = 0.9 and excitation frequency $\omega_1/2\pi$ = 0.1 Hz for $\sim$ 30 min. The recorded $I_{3/1}$, $I_{2/1}$ and Φ_3 reveal the dynamic character of the slip and the large effect of deformation time on the flow properties. In fig. 5.12 the time signals after 100 s, 700 s and 1300 s of measurement are presented. The observed distortions of the signal result in the intensities and phases shown in fig. 5.13. One cannot deduct stringent characteristic times for slip because the flow characteristics in this case are extremely sensitive to initial conditions and deformation history. Additionally, the surface characteristics may change depending on the quality of the fluorocarbon coating (depth, surface coverage) which may be sensitive at high temperatures and increasing time under large deformations. However, it is clearly demonstrated that the non-linearities and especially the appearing 2^{nd} harmonic, can be used to monitor phenomena like slip onset and evolution. With the analysis of the FT-Rheology

spectrum one can quantify the departure of a flow from a periodic non-linear viscoelastic type to a time-dependent non-linear rheological behaviour.

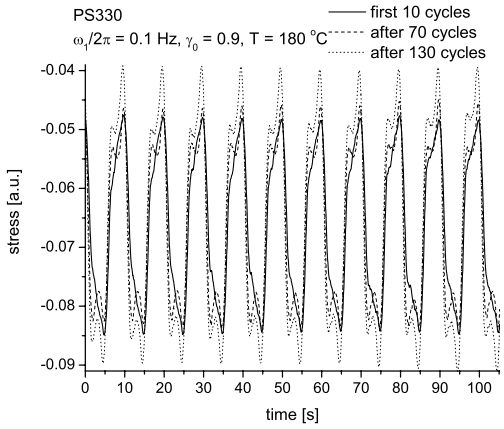

Figure 5.12: *Time signals recorded for LAOS of PS330 at different time points, at T = 180°C, using 8 mm diameter plates with fluorocarbonated surfaces and a 1 mm gap.*

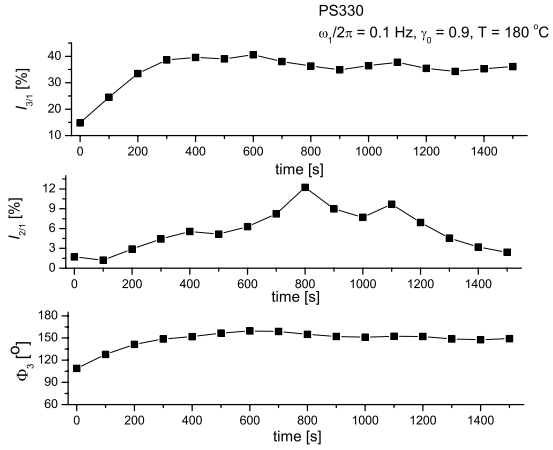

Figure 5.13: *Time evolution of slip monitored via FT-Rheology spectrum at T = 180°C for γ_0 = 0.9, with the ARES rheometer. Time t = 0 s corresponds to the initiation of LAOS after a strain sweep test and a delay time of 5 min. Plates of 8 mm diameter with a 1 mm gap and fluorocarbon-coated surfaces are used.*

5.3.3 Correlation of flow instabilities and molecular weight distribution

The critical strain amplitude for the slip onset as a function of molecular weight is presented in fig. 5.14 for linear polystyrene. For $\gamma_{0,c}$, the stress signal exhibits an amplitude decay, typically after 5 cycles the stress amplitude is 10% reduced. In literature slope values for critical shear rate for slip onset during capillary flow versus M_w/M_e of ~ 4 are reported [Allal 06]. However, for LAOS flows using steel plates the results presented in fig. 5.14 are found, where two molecular weight ranges can be distinguished. The first is of low molecular weight samples corresponding to $M_w/M_e \leq 6$, where a small dependence of the $\gamma_{0,critical}$ is found on molecular weight and $\gamma_{0,c} \propto (M_w/M_e)^{0.2}$. For an average number of entanglement per chain $N_e >$ 6-7, the power index is increased up to a value of $\sim$ 2. However, when fitting a scaling law of a $\gamma_{0,c}$ = a$(M_w/M_e)^n$ type, the determination of the exponent n can contain errors. This is demonstrated by the slight difference on the fit quality for the dashed lines in fig. 5.14, which correspond to slopes of 3 and 4. Nevertheless, a correlation of molecular weight and topological constrains (entanglements) with the onset of flow instabilities is revealed for the studied materials, wich are of linear topology and cover a wide range of molecular weight.

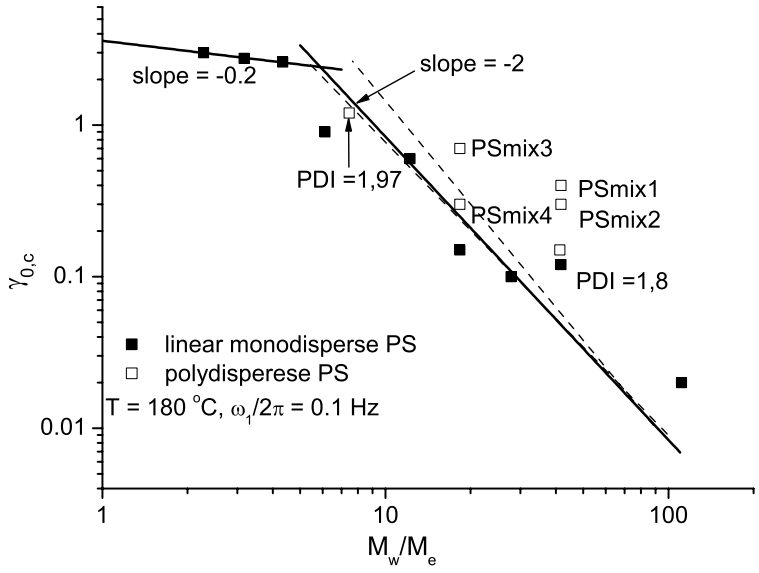

Figure 5.14: *Critical strain amplitude for stress signal amplitude decay as a function of number of entanglements per chain at T = 180°C, for LAOS with $\omega_1/2\pi$ = 0.1 Hz. Samples are linear polystyrene melts (Tables 3.1 and 3.2). Open symbols correspond to polydisperse samples. M_w for PSmix corresponds to the value of the high molecular weight component.The error in $\gamma_{0,c}$ is typically the size of the data points.*

5.3.4 Experimental procedure for determination of material inherent non-linearity with suppressed flow instabilities

It is obvious that flow instabilities are prominent when studying polymer melts via LAOS. In order to estimate the material non-linearity, especially of high molecular weight melts (typically $M_w > 100$), the contribution to the torque signal and the corresponding FT-spectrum of phenomena like wall slip must be suppressed. While the plate diameter is irrelevant, small gaps in the order of 1 mm are appropriate. The surface material is an important factor and a choice of steel plates is recommended. By using alumium as plate material, wall slip is enhanced and $I_{2/1}$ can be significantly higher (up to an order of magnitude for $\gamma_0 \approx \gamma_{0,critical}$). As expected, flow instabilities are maximized when fluorocarbon-coated plates are used, thus confirming the relation between increased non-linearities as quantified by the FT-spectrum ($I_{2/1}$, $I_{3/1}$ and Φ_3) and wall slip. Furthermore, by measuring at high temperatures, e.g. T = 200 °C for PS, the non-linearities and the occurring instabilities can be reduced. Additionally, the problem of overflow and large normal forces for an open-rim geometry (ARES) at large deformations (typically $\gamma_0 > 2$, for $\omega_1/2\pi$ = 0.1 Hz), can be controlled by using the closed-cavity geometry of the RPA2000. Since eq. 1.47 fits satisfactory the resulting $I_{3/1}$, it can be used to fit data at large γ_0 from RPA2000 ($2 < \gamma_0 < 10$), at small strain amplitudes in ARES (typically $0.1 < \gamma_0 < 0.5$) and predict the non-linearity for the range of deformations where the effect of normal forces and wall slip is prominent, $\gamma_0 > \gamma_{0,critical}$ (as demonstrated for PS330 and PS500 in fig. 5.3). With this method, the non-linear rheological behaviour of polymer melts can be quantified via $I_{3/1}(\gamma_0)$, for the whole range of applicable deformations.

5.4 Flow distortions in polyethylene melts-correlation with topology

The flow instabilities during LAOS flow are studied for the case of industrial polyethylene samples (see Table 4.1). The resulting non-linearities present a similar dependence on molecular weight as discussed for polystyrene melts. Polyethylene melts of higher molecular weight and/or higher polydispersity present higher $I_{3/1}(\gamma_0)$ and $I_{2/1}(\gamma_0)$ and the critical strain for slip onset, $\gamma_{0,critical}$ is lower. Laun has already reported lower critical shear rates for slip of HDPE of higher M_w, as detected from capillary flow, cone-plate and sandwich rheometer studies [Laun 82]. However, the specific samples have a smaller molecular weight range, namely 71 kg/mol $< M_w <$ 234 kg/mol, and they are highly polydisperse with *PDI* ranging from 1.9 to 20.4. Thus, deviations from a scaling behaviour as the one shown in fig. 5.14 are expected. The low entanglement molecular weight of polyethylene, M_e = 1.45 kg/mol [Seitz 93], results in a high N_e for the specific samples. Furthermore, the most important feature in these melts is the variation of topology, which may influence the onset and evolution of flow instabilities. The dependence of phenomena like slip on topological chain constrains is revealed through

this study. The critical strain amplitudes for the onset this decay, $\gamma_{0,c}$, is depicted in fig. 5.15 for all studied PE as a function of M_w/M_e.

From the plot of $\gamma_{0,critical}$ (critical shear rate for onset of stress time signal amplitude decay) versus entanglement number, it is obvious that no simple relation can be extracted between slip onset and molecular weight, due to the broadened molecular weight distribution and the significant difference in branching between the investigated samples. The critical deformation for slip decreases with increasing molecular weight, however no simple scaling law, $\gamma_{0,c}$ = a(M_w/M_e)^n, can be derived to describe this dependence. The difference from the case of linear monodisperse polystyrene melts (see paragraph 5.3) is the topological complexity of the samples. In the case of Wang and Drda [Wang 96a] where HDPE was studied, only three linear melts were used differing only in M_w (130.5 kg/mol, 225.6 kg/mol and 316.6 kg/mol). In Allal et al. [Allal 06] the extracted exponent from a similar plot has a value of 4.3 for three polyethylenes, however it is a fit parameter and deviations from this function are also seen in the particular work.

The critical strain amplitude for slip onset in LAOS is clearly reduced by the presence of LCB. Furthermore, for the case of the linear samples, the effect of a high polydispersity is clearly observed. Large macromolecules induce instabilities at relatively low deformations and dominate the non-linear rheological behaviour, whether the non-linearities and instabilities originate from material inherent non-linearity or due to flow characteristics. Presence of LCB increases the number of topological constrains for a polymer chain. Consequently branching affects the slip onset and development for a melt, either the latter is related to elasticity and constitutive material properties, or to an entanglement/disentanglement process of bulk chains with chains adsorbed on the wall [Barone 98, Wang 96b].

5.4.1 LAOS simulations including slip

The effect of changing the boundary conditions in a LAOS flow is studied numerically by combining the dynamic slip model from eq. 5.9 with the DCPP constitutive model, in a LAOS flow simulation performed according to chapter 2. A non-vanishing wall velocity is introduced for the lower boundary of the calculation domain (see fig. 2.3) which is time and stress dependent, according to Hatzikiriakos and Dealy [Hatzikiriakos 91, Hatzikiriakos 92a]. The introduction of a slip velocity which changes with time and is coupled with the calculated shear stress at the wall leads to LAOS signals with a decaying stress amplitude. This predicted stress time signal is in agreement with experimental LAOS results as depicted for a polydisperse LCB polyethylene in fig. 5.16. A parameter optimization is needed for an improved fitting of the stress in LAOS, however it is remarkable that this simple model can be easily coupled with a constitutive equation for the stress calculation and capture the effect of slip onset and development in a finite element simulation.

Slip parameter α is taken simply proportional to time, i.e. α= k·t and highly non-linear

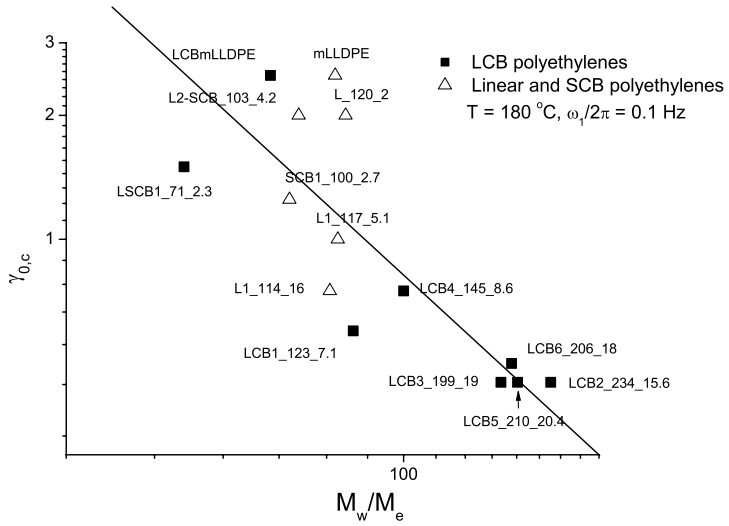

Figure 5.15: *Critical strain amplitude for stress signal amplitude decay for PE of Table refTable 1 as a function of number of entanglements per chain. T = 180°C, for LAOS with $\omega_1/2\pi$ = 0.1 Hz. Open symbols correspond to linear and SCB samples. Line of slope -2 is guide to the eyes. The error in determining $\gamma_{0,c}$ is typically the size of the data points.*

signals are calculated for a polyethylene modelled with the DCPP. When a higher slip velocity is calculated by increasing parameter *k*, the stress amplitude decay is larger, as seen in fig. 5.16. Such a highly distorted signal results from coupling wall shear stress with the non-vanishing wall velocity v_s (slip velocity). As an example, a predicted signal at theoretical extreme slip conditions is presented in fig. 5.17 and corresponds to a $I_{2/1}$ = 0.4% and a $I_{3/1}$ = 20% with a relative phase $\Phi_3 = 176°$. The calculated stress components of the DCPP model are reffered to as T_{11}, T_{12}, T_{22}, corresponding to the normal and shear stress components of the extra-stress tensor **T**, T_{xx}, T_{yy} and T_{xy}, respectively (see fig. 2.3). The FT-Rheology results from predicting a strain sweep with slip model and DCPP are shown in fig. 5.18. A change of $I_{3/1}(\gamma_0)\ \Phi_3(\gamma_0)$ is predicted in the evolution of the non-linearities with increasing strain amplitude, from the use of a slip model as a boundary condition.

The calculated velocity profile for LCB2_234_15.6 is presented in fig. 5.19 for a LAOS simulation with the DCPP model, including slip condition in the lower plate. A non-vanishing velocity in the lower wall is indeed predicted and has a value $\sim$ 10% of the maximum velocity (which corresponds to the wall velocity of the upper moving plate). One can extrapolate the velocity profile and extract the length parameter *b* (see eq. 5.3) which in this case it is caclulated to $\sim$ 0.07 mm, for a gap of 1 mm between the plates.

As demonstrated in paragraph 4.3.2, the normal stress difference can be determined for a LAOS flow simulation using the DCPP model. This quantity shows a dependence on topological parameters of the model and can further be analyzed via Fourier transformations.

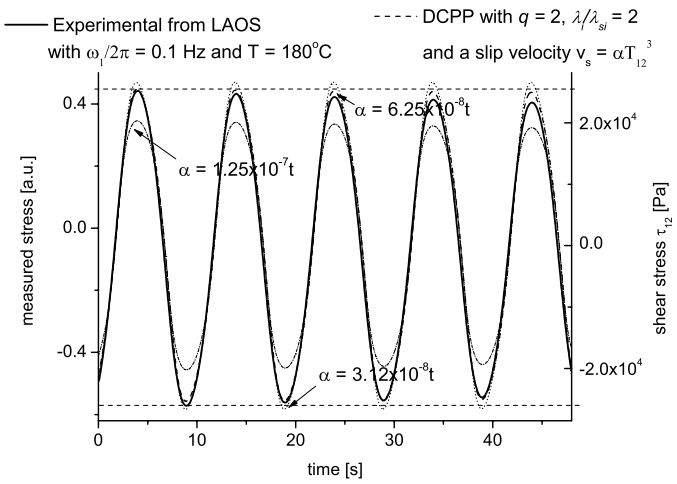

Figure 5.16: *LAOS stress time signal experimentally measured at T = 180 °C, with $\omega_1/2\pi$ = 0.1 Hz and γ_0 = 3 and predicted by DCPP model coupled with a dynamic slip model. Modelled sample is LCB2_234_15.6, LCB polydisperse polyethylene melt. The stress amplitude decay is larger for large values of α.*

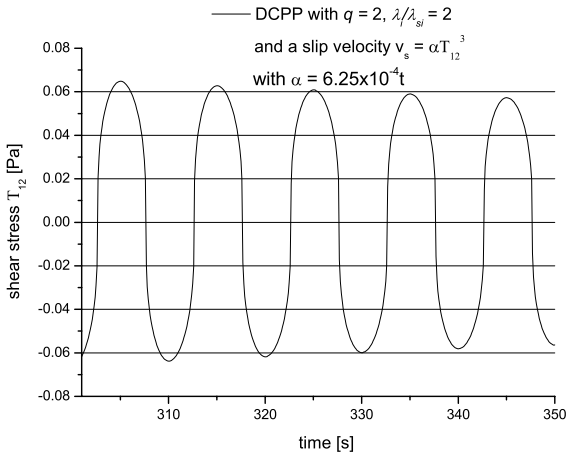

Figure 5.17: *Prediction of a LAOS stress time signal for modelled sample LCB2_234_15.6 at T = 180 °C, with $\omega_1/2\pi$ = 0.1 Hz and γ_0 = 3, increasing parameter α by 10^4, thus predicting large slip velocities.*

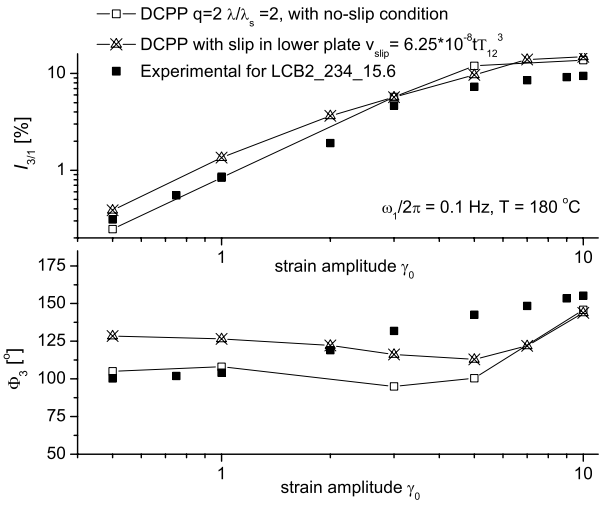

Figure 5.18: *Predicted $I_{3/1}(\gamma_0)$ and $\Phi_3(\gamma_0)$ for modelled sample LCB2_234_15.6 at T = 180 °C and $\omega_1/2\pi$ = 0.1 Hz. The DCPP model is coupled with a slip equation.*

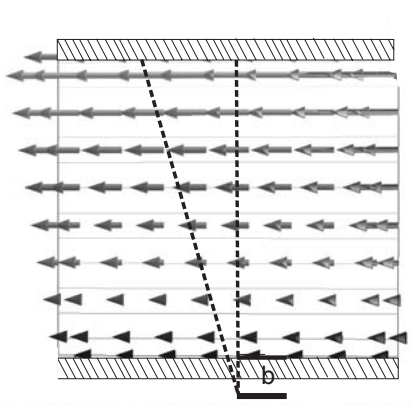

Figure 5.19: *Predicted velocity profile for a LAOS flow with $\omega_1/2\pi$ = 0.1 Hz, γ_0 = 10 and T = 180 °C for a modelled polyethylene LCB2_234_15.6. The DCPP model is coupled with a slip equation for the lower plate and a non-vanishing velocity is calculated at the lower plate.*

The resulting intensities of the higher harmonics, at odd multiples of the excitation frequency ($2\omega_1$, $4\omega_1$,...e.t.c.) can be used for the quantification of the normal forces in LAOS. Since, the normal forces are crucial to the occurrence and evolution of flow instabilities [Larson 92], one can analyze the "fingerprint" of N_1 for a simulated flow including wall slip. As an example the resulting normal stress difference for the LAOS flow with a slip law is calculated for several strain amplitudes n fig. 5.20. The resulting stress components in the normal direction can differ significantly when slip takes place from the case of non-slip condition, as depicted in fig. 5.21.

Furthermore, it is proposed that the ratio between shear and normal stresses may be the

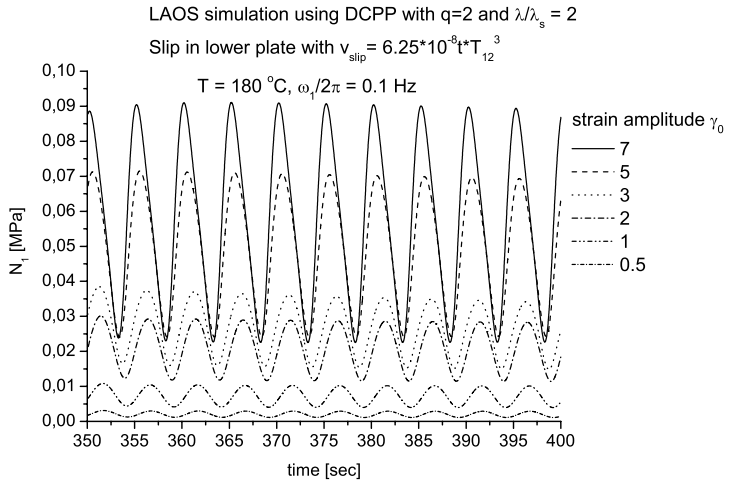

Figure 5.20: *N_1 for a simulated strain sweep with the DCPP model coupled with a slip equation for the lower plate. The modelled sample is LCB_234_15.6.*

critical quantity controlling the concurrence of flow instabilities in LAOS flows [Larson 92]. Thus, this ratio is predicted and shown in fig. 5.22 for the case of no-slip boundary conditions and for the simulation with a DCPP modelled coupled with the slip law. The existence of a critical point during the LAOS flow is evident, where the wall shear stress is close to its maximum value. The contribution of the normal forces becomes significant and increases the non-linearity of the response. This can be the onset of instabilities and flow distortions. A change in the ratio of shear to normal stresses is observed when slip takes place. In that case, the normal stress difference is smaller (as seen also in fig. 5.21) and the shear stress has a higher contribution in the predicted stress response of the polymer, which may be directly connected to the non-vanishing tagential velocity at the lower plate and the slip occurrence. Nevertheless, experimental data for N_1 are needed for deriving conclusions about the onset and development of flow instabilities in LAOS flow.

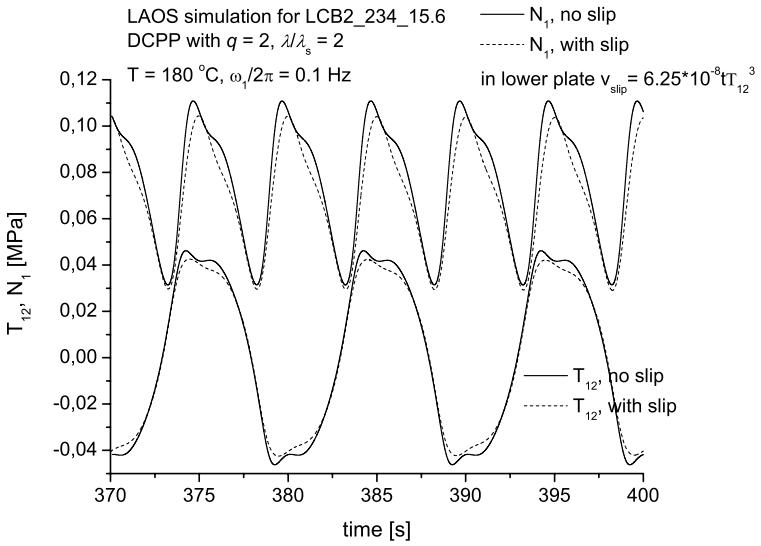

Figure 5.21: *Normal stress difference, N_1 and wall shear stress, T_{12} for LCB_234_15.6, at γ_0 = 5, for no-slip boundary conditions and for slip law imposed at the lower plate.*

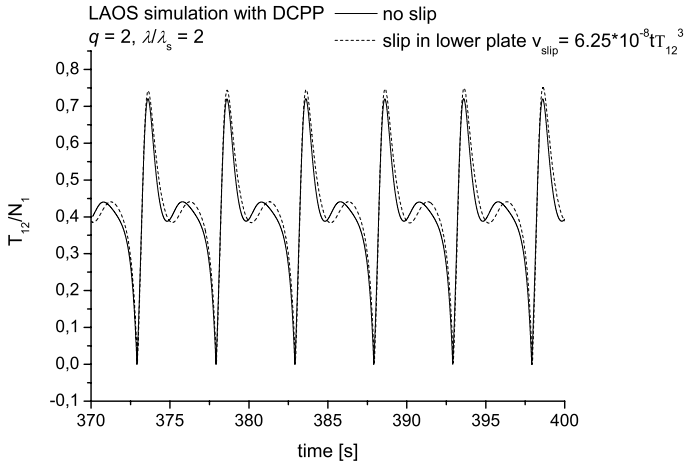

Figure 5.22: *Ratio of shear stress to normal stress difference for modelled LCB PE, at γ_0 = 5, for no-slip boundary conditions and for slip law imposed at the lower plate.*

5.4.2 Correlation between LAOS non-linearities and capillary flow distortions

The industrial polyethylene samples (see Table4.1) are tested in capillary flow. To achieve capillary flow, a piston is used to generate pressure on the test polymer melt in a reservoir, which is thus forced through a die (capillary tube) of a specific diameter, *D* and length, *L* [Macosko 94]. The shear viscosity is determined by relation between wall shear stress and wall shear rate. By measuring the pressure drop, p_c, and flow rate, Q, of the melt through the die are used to determine the viscosity, using the following equations [Macosko 94] for apparent flow (no corrections for slip):
Wall shear stress:

$$T_{12,w} = \frac{Dp_c}{4L} \tag{5.11}$$

Wall shear rate:

$$\dot{\gamma}_{a,w} = \frac{32Q}{\pi D} \tag{5.12}$$

Additionally, the pressure on the walls is recorded and the extrudate is studied with respect to its surface distortions. This process is similar to extrusion and allows access to rheological properties at high deformations. However, partial wall slip influences the results and must be taken into consideration [Laun 04]. The experimental setup is modified with the used of sensitive pressure transducers and is presented in more details by Filipe et al. [Filipe 06]. Measurements are performed under constant pressure and also under constant piston velocity using two different dies, a cylindrical with: *L* = 30 mm and *D* = 1 mm and a slit die with: *L* = 30 mm and crossection of 0.3 mm $\times$ 3 mm. During the measurement of the apparent shear stress, pressure oscillations are recorded in three different points along the die, namely: 3 mm, 15 mm and 27 mm after die entrance named tr1, tr2, tr3 respectively. A schematic representation of the capillary geometry is shown in fig. 5.23.

In fig. 5.24 and 5.25 the apparent flow results are shown for linear and LCB polyethylene melts respectively. The measurements are performed at T = 180 °C with one cylindrical die. The critical shear rate or stress for the onset of slip is of interest at this point and it can be determined by a change in the slope of shear rate plotted against stress.

For the linear polyethylene samples a proportionality between the critical stress for slippage in capillary flow and the critical strain amplitude in LAOS flow, $\gamma_{0,c}$ is determined within this work. The latter critical strain amplitude is defined (as described in paragraph 5.3 and 5.4) by the lowest strain amplitude where stress time signal decay is observed. However, this critical deformation depends on several factors, as discussed in paragraph 5.3. Within this analysis for the PE samples, steel parallel plates of 13 mm diameter with a 1 mm gap are used, for strain sweeps conducted at T = 180 °C and $\omega_1/2\pi$ = 0.1 Hz. Results are presented in fig. 5.26 and an increase of both the critical capillary wall stress and $\gamma_{0,c}$ is found for increasing SCB content. Although SCB is not considered to have a significant effect on the rheological properties, the results show that by incorporating SCB in polyethylene the

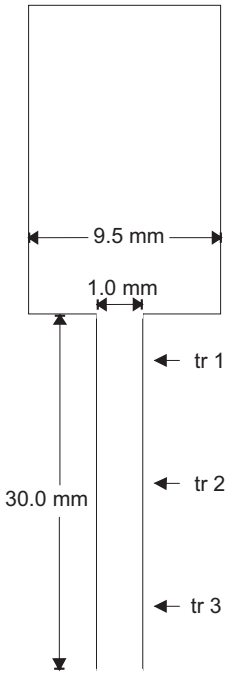

Figure 5.23: *Schematic representation of the capillary reservoir and the die. The three pressure transducers, tr1, tr2 and tr3 are at 3 mm, 15 mm and 27 mm from the die entry respectively.*

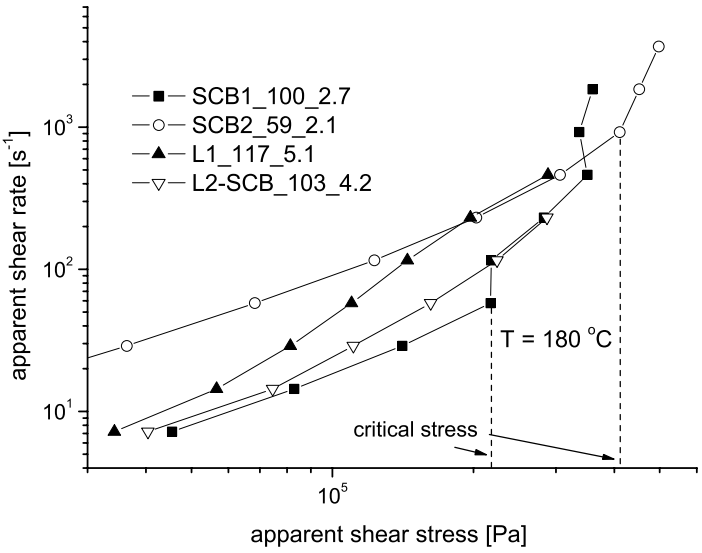

Figure 5.24: *Apparent capillary flow data for linear and SCB polyethylenes at T = 180°C. Die aspect ratio is L/D = 90. Measurements were conducted by S. Filipe. Critical stresses are indicated as determined by a change of the slope of the flow curve.*

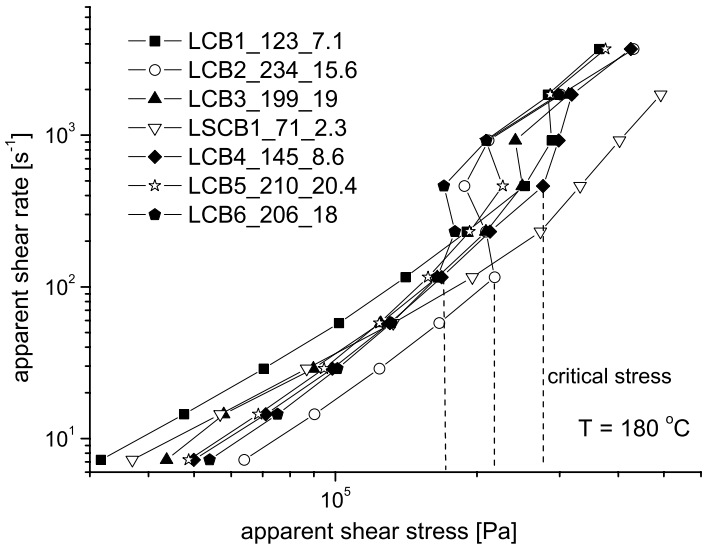

Figure 5.25: *Apparent capillary flow data for LCB polyethylenes at T = 180°C. Die aspect ratio is L/D = 90. Measurements were conducted by S. Filipe. Several critical stresses are indicated as determined by a change of the slope of the flow curve.*

flow can be more stable. In SCB materials the slippage onset is delayed and the instabilities suppressed, as shown from the slopes of the corresponding apparent shear-rate versus stress curves (see fig. 5.24). Additionally, for linear polyethylene samples with similar content of SCB, larger M_w and broad molecular weight distributions (increased *PDI*) result in an onset of slip at lower strain amplitudes and wall stresses.

Polyethylenes containing LCB chains show flow instabilities at significantly lower critical deformations, as depicted in fig. 5.27. The plateau nonlinearity in LAOS flow, as quantified by parameter A (see eq. 1.47), or in other words the maximum possible deviation from linear viscoelastic behaviour, as quantified by FT-Rheology, is generally higher for melts that tend to slip at lower critical stresses. Furthermore, these highly non-linear materials are more likely to flow in an instable manner. This is presented in fig. 5.28, nevertheless no simple $\gamma_0 = a(M_w/M_e)^b$ proportionality can be derived. An explanation about this deviation is that, A is a fitting derived parameter of the non-linear behaviour as quantified via $I_{3/1}(\gamma_0)$ and is a result of non-linear viscoelasticity . One cannot easily discriminate the factors affecting the non-linear behaviour of melts. However, results from capillary and LAOS flows for macromolecules with different topologies show that instabilities can originate from material structure, since for example for the case of RPA2000 non-linearities due to wall slip are insignificant. These material non-linearities can be suppressed or reinforced by the flow type, i.e. large deformations, flow geometry and surface type.

In order illustrate the different occurring instabilities of samples with varying topol-

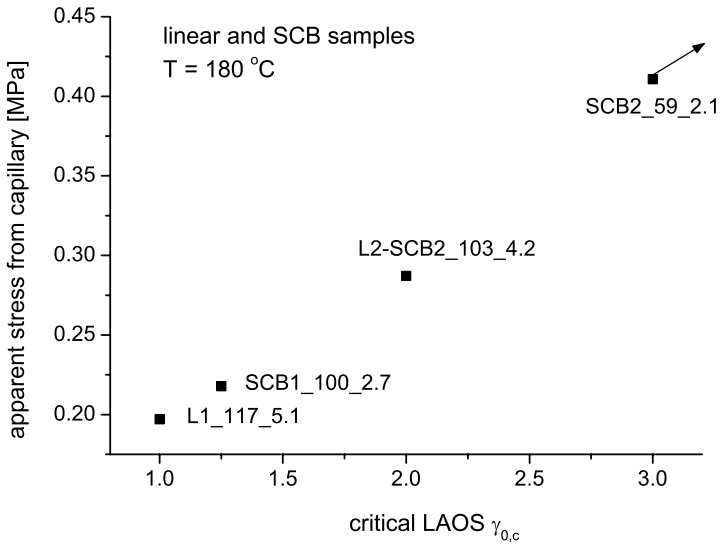

Figure 5.26: *Correlation between apparent wall capillary stress and critical strain amplitude in LAOS flows, for linear and SCB samples at T = 180 °C. Sample SCB2_59_2.1 presents instabilities for higher deformations, not experimentally reachable with ARES.*

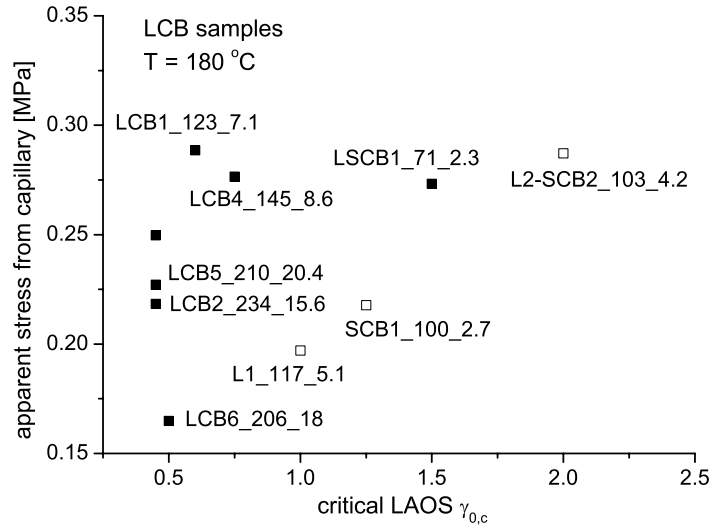

Figure 5.27: *Correlation between apparent wall capillary stress and critical strain amplitude in LAOS flows, for LCB polyethylenes at T = 180 °C (filled symbols). Results for linear PE are given in open-symbols for comparison.*

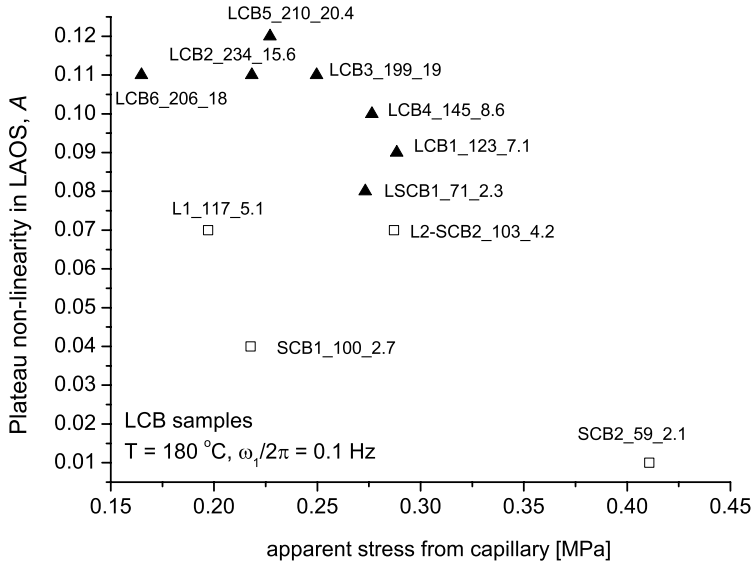

Figure 5.28: *Non-linearity plateau of LAOS flow for polyethylenes with different measured critical stresses for slip in capillary flow, as defined by slope change of apparent flow plots, at T = 180°C. Open-symbols are used for linear and SCB PE.*

ogy and non-linearity, photographs of the extrudates are presented in fig. 5.29 and 5.30. The first figure depicts two melts, LCB2_234_15.6 and LCB6_206_18, which present stick-slip instability. This is recognized by the interchanging regions of smooth extrudate and periodic surface distortions. Both samples present highly nonlinear rheological behaviour under LAOS flow with A = 0.11. On the contrary, sample SCB1_100_2.7 which is linear with 4.5 SCB / 1000 CH_2, presents low non-linearities with A = 0.04 even at higher apparent shear-rates, while exhibits only sharkskin type extrudate distortions (see fig. 5.30).

The observed extrudate distortions, such as sharkskin (see fig. 5.30) stick-slip (see fig. 5.29) and melt fracture are correlated, with respect to their periodicity and intensity, to the measured pressure deviation, σ_P and the pressure oscillation period [Filipe 06]. These distortions on the extrudate surface are of great importance and a method to predict these occurring instabilities at large deformations is needed. The measured average σ_P is subsequently correlated to the non-linearities in LAOS flow and FT-Rheology data of the studied materials.

Results reveal a strong relation between the plateau non-linearity measured in a LAOS flow via FT-Rheology and the pressure deviation measured by the pressure transducers in the capillary, as presented in fig. 5.32. The pressure oscillations are recorded for capillary flow of melts under constant piston velocity. An example of measured pressure from the three different transducers in the slit die for LCB2_234_15.6 is presented in fig. 5.31. A similar setup was used by Laun [Laun 83], however due to the low transducer sensitivity, the pressure

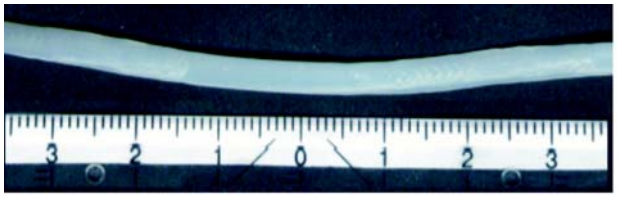

Figure 5.29: *Stick-slip instabilities for two LCB polydisperse polyethylene melts, for the slit die. Experiments were performed by S. Filipe.*

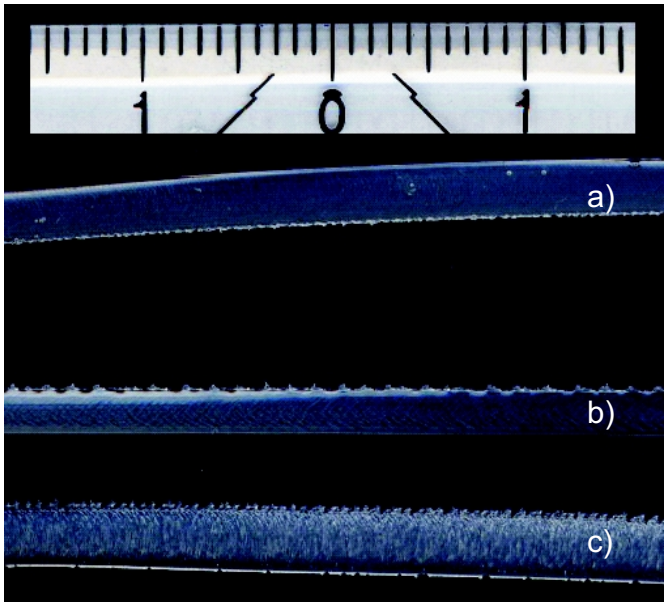

Figure 5.30: *Sharkskin surface distortion of SCB1_100_2.7, at 180 °C, for 230 s^{-1} (a), 920 s^{-1} (b) and 1420 s^{-1} (c) apparent shear rate. Measurements were performed by S. Filipe.*

oscillations could not be accurately measured.

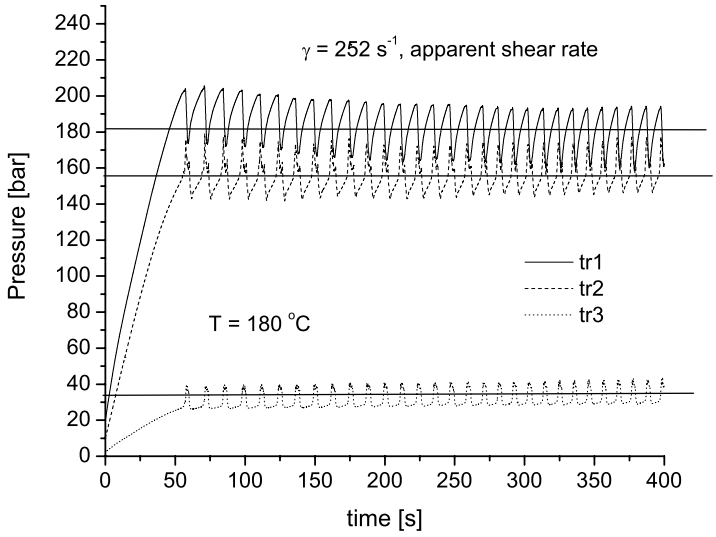

Figure 5.31: *Example of recorded pressure oscillations from the transducers in a slit die of L = 30 mm and a crossection of 0.3 mm × 3 mm. Sample is LCB2_234_15.6. The average pressure is 180 bar, 155 bar and 30 bar for tr1, tr2 and tr3, respectively. Measurements were performed by S. Filipe.*

5.4.3 Capillary flow simulations and prediction of extrudate distortions

Modelling the capillary flow of molten polyethylene and predicting the occurring flow instabilities has been a subject of interest in the past [Achilleos 02, Georgiou 94, Rutgers 01]. A numerical simulation with the capability of capturing the free surface extrudate distortions as well as predicting the experimentally measured pressure oscillations can relate instabilities with structure and predict the performance of materials during capillary flow or extrusion. In this paragraph some preliminary results are presented for the case of an LCB PE. The DCPP model is mainly used in order to capture the dependence of the instabilities on topological characteristics of the material. The model is coupled with a slip equation to describe the correlation between wall shear stress and slip velocity. In order to simplify the problem the flow is additionally modeled with a simpler shear-rate dependent viscosity equation, and specifically the Carreau-Yassuda model [Carreau 97]:

$$\eta = \eta_\infty + (\eta_0 - \eta_\infty)(1 + (\lambda\,\dot{\gamma})^{a_c})^{\frac{n-1}{a_c}} \tag{5.13}$$

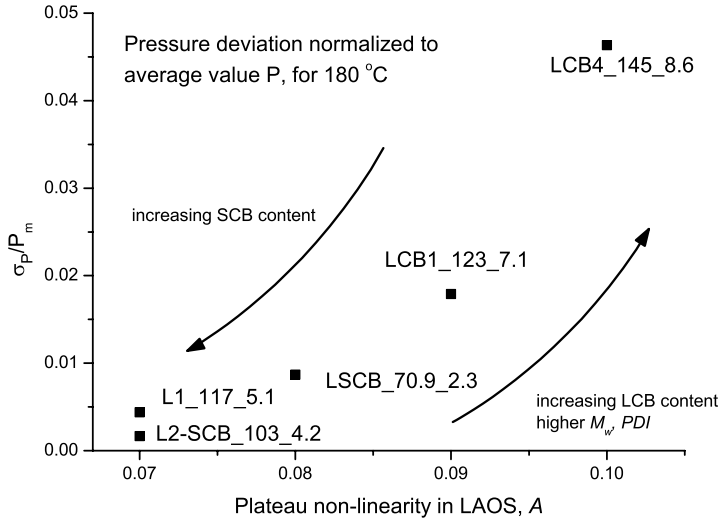

Figure 5.32: *Standard deviation of the pressure normalized to mean pressure value for polyethylenes with different non-linearity plateau of LAOS flow. All measurements are at T = 180°C and the pressure measurements correspond to an apparent shear-rate of 800 s^{-1} in a slit die.*

where η_0 is the zero-shear rate viscosity, η_∞ is the infinite shear-rate viscosity (lower Newtonian plateau), λ is the inverse of the critical shear-rate, or the pivot point, for transition from Newtonian to non-Newtonian fluid behaviour. The parameter a_c controls how abrupt this transition is. If it is lower $a_c > 1$, a longer transition regime is predicted. If $a_c > 1$ an abrupt transition is calculated for the viscosity. Finally, parameter *n* is the power-law index [Polyflow 03].

For the simulations performed using the DCPP model, the parameters are identified as mentioned in chapter 2. The flow of polyethylene in the whole capillary (reservoir and die) is simulated and also the case where only the die is considered. The calculation domains with the boundary conditions are described in fig. 5.33.

Simulations with no-slip boundary condition for the die walls predict a stress distribution for the die entry in qualitative agreement to literature [Baaijens 97, Clemeur 04]. The predicted stress distribution at the exit is also in qualitative agreement to numerical studies in literature [Rutgers 00, Rutgers 01]. A die swell is predicted for the extrudate with no surface instabilities, even at high shear rates, where experimentally sharkskin or stick-slip instabilities are observed for the specific polyethylene melt. The stress distributions for the die exit are depicted in fig. 5.34, using the DCPP model. High wall shear stresses are calculated near the exit, reflecting the absence of slip.

Additionally, the scalar stretch variable Λ (see eq. 2.16), which describes the stretching of the pom-pom backbone, can be calculated for the entry and the exit of the modelled

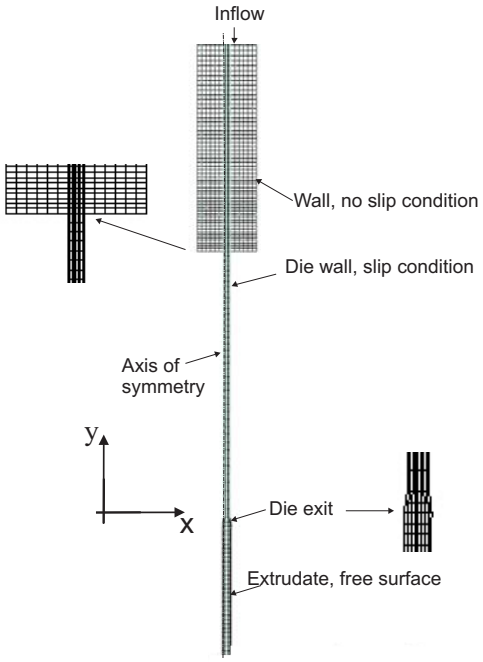

Figure 5.33: *Calculation domain for capillary flow with a cylindrical die of L = 30 mm and D = 1 mm. The contraction ratio in the die entry is 9.5. Mesh consists of 2400 elements.*

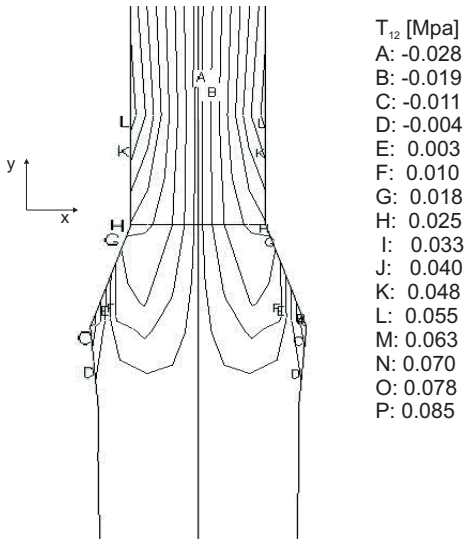

Figure 5.34: *Shear stress T_{12} for LCB2_234_15.6 at low apparent shear rate ($\sim$4 s^{-1}) in the die exit.*

melt. It represents the backbone length after the deformation normalized to the initial backbone length. The large stretching that the pom-pom molecules undergo, especially in the axis-center of the flow, is reflected in fig. 5.35. After a short distance from the entry, the distribution of Λ shows a relatively homogenous stretching of the pom-pom molecules.

Simulations are additionally performed for flow rates corresponding to experimental

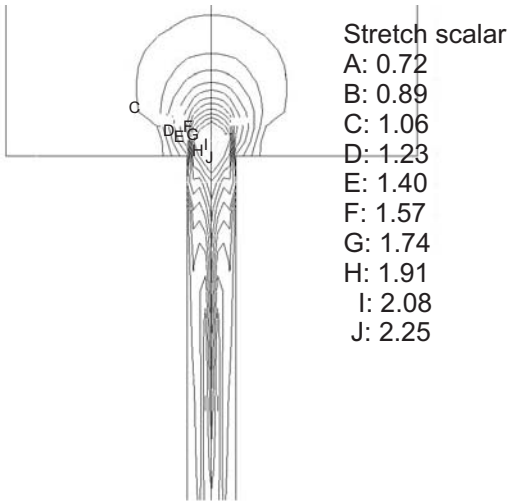

Figure 5.35: *Stretch variable Λ calculated for the DCPP model with q = 2, λ/λ_s = 2, at the die entry. Apparent shear rate $\approx$ 4 s^{-1}. Larger stretching of the pom-pom backbone is predicted near the flow axis at the die contraction.*

apparent shear rates larger than the critical shear rate for instabilities onset (which is 100 s^{-1} for LCB_234_15.6). Significantly larger stresses are predicted for both the entry and the die exit. As an example in fig. 5.36 the normal stress T_{11} is depicted which takes large values at the wall near the exit and is eventually responsible for the swelling of the polymer after the exit. The significantly larger stretching of the pom-pom molecules near the axis of the die is reflected on the higher Λ for this case, as shown in fig. 5.37.

The die is long enough for the entry effects to be insignificant with respect to the stresses at the exit and the resulting extrudate swell for this case, as shown from the stress distribution in the die entrance. Thus, the focus is to predict the flow inside the die and the phenomena taking place at the exit, considering the entrance effects irrelevant to the extrudate distortions for this specific geometry. The calculation domain is restricted to the die and the extrudate, as presented in fig. 5.38. A constant inflow rate is imposed (to model the constant piston velocity), corresponding to high apparent shear rates ($\dot{\gamma}_{apparent} >> 250^{-1}$), i.e. in the flow regime where stick slip is experimentally observed for the specific sample in the studied capillary flow.

By introducing a wall-slip condition for the die, instabilities are predicted in the extrudate surface. However, from the numerical calculation point of view, non-vanishing wall velocities reduce convergence problems since the velocity profile has no singularities at the

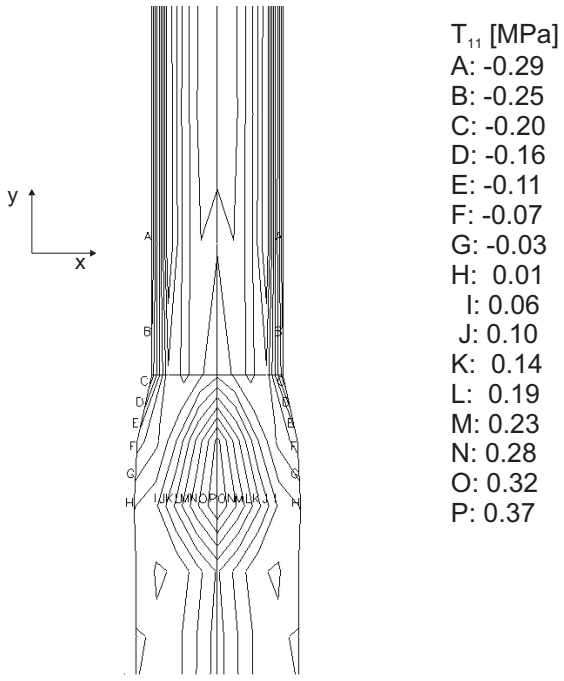

Figure 5.36: *Normal stress T_{11} for modelled LCB2_234_15.6, at flow rate corresponding to critical apparent shear rate (100 s^{-1}), for the die exit and extrudate. High normal stresses are predicted at the wall region in the die and near to the exit.*

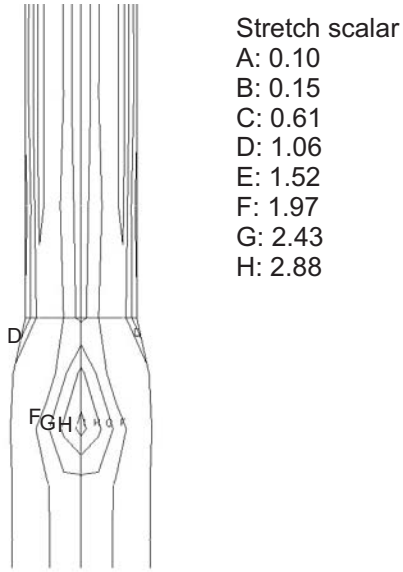

Figure 5.37: *Stretch variable Λ for modelled sample LCB2_234_15.6. Prediction with the DCPP model at the die exit. Apparent shear rate is approximately 100 s^{-1}. The predicted extrudate is highly stretched.*

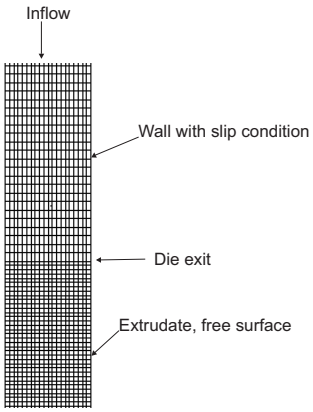

Figure 5.38: *Part of the calculation domain for simulation of polymer flow through the capillary die, including the extrudate. The set of boundary conditions is also given. The specific mesh consists of 5000 elements and the density of the mesh is increased in the extrudate.*

wall. Thus, it is possible to simulate flows of higher Weissenberg numbers, $W_i = \lambda\ \dot{\gamma}$, for which convergence difficulties are encountered when imposing a non-slip condition. The slip law used is in agreement with eq. 5.9.

A dependence is revealed for the flow instabilities on the slip parameters. Slip parameter α can be a constant or a function of time (the problem is isothermal and no temperature dependence of α is considered, as in Hatzikiriakos and Dealy [Hatzikiriakos 92b]). By coupling the slip equation with the Carreau-Yassuda model (see eq. 5.13), one can predict the developement of distortions on the extrudate free surface. In fig. 5.39 results from two time-steps are depicted. The predicted time evolution of surface distortions is presented as reflected in the normal stress distribution at the die exit. These sets of T_{11} contours correspond to time-steps of the calculation during the build-up of normal stresses and the appearance of flow distortions approximately 4 s later. The normal stress is significantly lower in comparison with flow under no-slip conditions. However, T_{11} increases periodicaly near the exit and contributes to the formation of instability effects on the free surface.

Furthermore, the pressure, P, and the first normal stress difference, N_1 as a function of time can be derived, at the same points along the die, where the pressure transducers are installed in the experimental setup. However, the predicted P and N_1 time signals are decaying, in contrast to experimental data where pressure oscillations of constant amplitude are recorded during stick slip occurrence (see fig. 5.31). This may be improved by the use of a more elaborated slip equation.

With the use of a large value for the slip velocity in the simulation a stable flow may be predicted (no extrudate surface distortions). However, for unrealistically high slip velocities a plug flow is predicted and the expected die swell phenomenon vanishes. Generally the slip law parameters are adjusted in order to result in a realistic slip velocity $v_{slip} \leq 0.1$ v_{max} [Polyflow 03]. It must also be noted that the used slip models are phenomenological

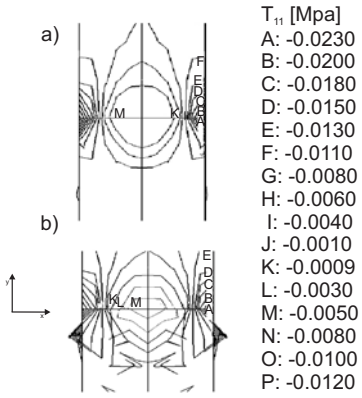

Figure 5.39: *Normal stress T_{11} for modelled sample LCB2_234_15.6 at die exit for apparent shear rate corresponding to the region of experimentally observed stick-slip. a) During stress build-up, t = 1.5 s. b) After the occurrence of flow instabilities and extrudate distortions, t = 5 s.*

and empirical with no solid physical background that correlates the slip phenomenon with structural properties of the polymer material. Nevertheless, the applicability of a slip law in combination with a simple non-linear viscosity model (like Carreau-Yassuda) or a more complicated constitutive equation (DCPP) in order to describe the capillary flow of a polymer melt and model the occurring flow instabilities is remarkable. At this stage no quantitative results can be derived. However, it is demonstrated that using slip parameters to calculate a realistic slip velocity, for example using eq. 5.9, one can predict surface distortions in qualitative agreement with the experimental observations (see fig. 5.39). These parameters are however not universal and they must be defined for each material and wall surface characteristics.

5.5 Summary on the study of flow instabilities of polymer melts via FT-Rheology

In the present chapter the occurring flow instabilities of polymers under LAOS flow are investigated via FT-Rheology and simulations. The experimental setup allows the recording of stress as a function of time with a high sensitivity. Hence, phenomena like stress signal

amplitude decay, or appearance of even harmonics in the FT-spectrum can be analyzed and correlated to the occurring flow instabilities with increased sensitivity and for samples well-characterized with respect to their topology and molecular weight distribution.

The evolution of the non-linearity in a strain sweep experiment depends strongly on molecular weight, molecular weight distributions and topology of the studied polymer. Additionally the onset of flow instabilities, as quantified by the critical strain amplitude for stress signal decay, is decreasing for increasing molecular weight and LCB content. It is possible to predict LAOS instable flow by simulations using the DCPP model coupled with a slip equation, which relates slip velocity with wall shear stress. Shear stress of decaying amplitude can be predicted and fitted to experimental time and FT data for LCB polyethylenes.

All investigated polyethylene melts are complementary measured in a capillary using a cylindrical and a slit die. The observed flow instabilities and distortions, such as sharkskin effect, stick-slip, gross fracture, are recorded along with the critical apparent shear rate for their occurrence and the oscillations of the normal pressure in the die. The results show a strong relation with the LAOS flow. This demonstrates that FT-Rheology is a promising method to investigate flow instabilities (e.g. constitutive instabilities, slip) and predict the occurring flow distortions in a capillary extrusion. The standard deviation of the pressure on the die wall is proportional to the plateau non-linearity, *A*, of the material, as measured in a parallel plate geometry by FT-Rheology. Additionally the critical strain amplitude, $\gamma_{0,critical}$ for instabilities in LAOS shows a similar dependence on molecular weight, molecular weight distribution and topology, with the critical apparent shear rate (or critical stress) for capillary flow distortions. Furthermore simulations of the capillary flow using simple viscosity models (like Carreau-Yassuda) or a more complex constitutive equation (DCPP), can predict flow instabilities and pressure oscillations in the capillary die, when coupled with an appropriate slip model.

Finally, results from both flow types, LAOS and capillary, can be used to correlate flow distortions and material non-linearity with molecular weight distribution and molecular architecture (type of branching). It is found that materials with high non-linearity plateau, *A*, as determined by FT-Rheology, present large pressure deviations in a capillary flow and consequently extrudate distortions like stick-slip, while materials of low *A* (eq. 1.47) present low instabilities and sharkskin for the same shear rates. The first is the case for LCB PE and materials of high molecular weight (as quantified by M_w, *PDI*) and the latter behaviour is observed for PE with lower non-linearity, namely linear of low M_w and SCB. However, one should also investigate more intensively the effect of the normal stress differences in the onset and evolution of flow instabilities. Specifically, the term N_1/T_{12} may be a more effective variable to be correlated to the slip velocity. Larson further suggested that the above ratio of normal stress difference to shear stress may be the critical parameter controlling the surface distortion phenomenon in cone-plate and plate-plate flows [Larson 92].

By studying the non-linear rheological behaviour of materials under LAOS with the

high sensitivity that FT-Rheology provides, one can predict occurring instabilities in capillary flows. These flow distortions are partially due to constitutive instabilities, or in this work mentioned as inherent material non-linearity, which is quantified via FT-Rheology according to chapters 3 and 4. The results from this analysis are strongly connected with structural properties of the studied melts, i.e. molecular weight, molecular weight distribution and topology (SCB, LCB), while additional factors such as temperature, pressure and deformation history have an additional influence on the non-linear behaviour in both LAOS and capillary flow.

Chapter 6

Conclusion and summary

The detection and characterization of polymer architectures is an extremely important subject for the polymer industry and especially for the polyolefine production and processing. The knowledge of the rheological properties which result from incorporated long- (LCB) and short-chain branching (SCB) on a polymer chain and the information about the effect of the permanent (branches) and non-permanent (entanglements) topological constrains, can be used to optimize the processing and end-use properties of polymer products. Large amplitude oscillatory shear (LAOS) combined with FT-Rheology is established as a method to probe structural characteristics and quantify the non-linear rheological behaviour of different polymer topologies in both solutions and melts [Höfl 06, Neidhöfer 03a, Neidhöfer 03b, Neidhöfer 04, Schlatter 05].

A systematic study of well-characterized polymers with FT-Rheology provides the "fingerprints" of linear, short-chain branched (SCB) and long-chain branched (LCB) macromolecules in the non-linear regime. This rheological regime is the most often encountered in polymer processing industry. The resulting intensity of the 3^{rd} harmonic as a function of strain amplitude, $I_{3/1}(\gamma_0)$, can be described by empirical equations (eq. 1.47 and eq. 1.51). The derived non-linear parameters, A (non-linearity plateau), B (inverse critical strain), C (slope of log$I_{3/1}$ vs. logγ_0 at low strains) and D (non-linearity at low and medium strain amplitudes), are used to quantify the material non-linear rheological behaviour.

Measurements performed for monodisperse polystyrene (PS) linear melts of a wide range of molecular weights with M_w = 41 kg/mol - 4530 kg/mol, reveal a strong correlation between molecular weight and mechanical non-linearities, as quantified via FT-Rheology with the relative intensity of the 3^{rd} harmonic, $I_{3/1}$, and the relative phase, Φ_3. Parameter D is found to be proportional to $M_w^{2.5}$. In a polydisperse melt, the non-linear rheological behaviour is dominated by the large macromolecules, however the effect of this high molecular weight can be reduced by diluting the melt with smaller chains. An increase of polydispersity index (PDI) up to 2, for a PS melt with $M_w \approx$ 100 kg/mol, can result to a 5 times larger $I_{3/1}$. Additionally, if a PS of high molecular weight (e.g. M_w = 750 kg/mol) is "diluted" to

70 wt % with a PS of low M_w (e.g. M_w = 41 kg/mol) the derived parameter D for the blend is found to be 1/6 of the value for high M_w component (e.g. M_w = 750 kg/mol). Combining the results from LAOS flow measurements of polydisperse linear polystyrene melts and binary blends, one can conclude that the non-linearities increase with increasing chain length, or equivalently with increasing number of entanglements per macromolecule. The non-linear response becomes more complicated when branches are incorporated in a linear chain. Finite element simulations are performed to predict linear and non-linear rheological properties of polystyrene comb-like architectures in melt or solution, using the Pom-pom model in the DCPP formulation (double-convected Pom-pom model [Clemeur 03]). The resulting intensities and phases of the higher harmonic contributions are in relatively good agreement with experimental data, taking into account that the rheological properties of a comb-like polymer are described by a multi-mode model for a pom-pom topology. For linear polymers the Giesekus model performs as good as the DCPP in predicting FT-Rheology data. However, when simulating LAOS flows for H-shaped and generally branched PS melts, the DCPP model is found to satisfactory capture the non-linear rheological behaviour. An increased number of relatively short branches (containing 1-2 entanglements per arm) can act as a "solvent" for the polymer backbone, thus reducing the non-linearity, as measured experimentally and predicted by the DCPP model. The effect from the presence of branches of various lengths and quantities on the non-linear rheological behaviour of polymers is demonstrated. Thus, it is experimentally and theoretically supported that FT-Rheology is sensitive towards molecular structure, i.e. branching, molecular weight and molecular weight distribution.

Samples of well-defined topology (mainly anionically synthesized) are good candidates to be used for studying the effects of branching on the polymer shear flow. However, they are mainly produced in a laboratory scale and their purity, monodispersity and stability may differ significantly from that of industrial samples. Therefore, the method of combined experimental FT-Rheology with complementary NMR spectroscopy analysis and finite element LAOS flow simulations is extended to industrial polyolefines, specifically polyethylene (PE) of varying molecular weight, molecular weight distribution, branching type and content. A dependence of the resulting non-linearities on M_w and *PDI* is also determined, in consistency with the results from model polystyrene samples. The non-linear parameters A and B can be predicted as a function of molecular weight distribution with a linear equation, $a + bM_w + cPDI$, for linear and SCB polyethylenes. Additionally, an incorporation of a small amount of LCB increases significantly the non-linearity of the stress response for the whole range of applied deformations, as well as the Φ_3. As an example, a LCB PE sample with M_w = 123 kg/mol and PDI = 7.1 contains 0.2 LCB/1000CH_2, which result in increased values for A and B (9 % and 0.3 respectively) in comparison with a linear PE of similar molecular weight distribution, with M_w = 117 kg/mol and PDI = 5.1 (with A = 7 % and B = 0.23). Hence, the FT-Rheology parameters introduced show a great potential in quantifying branching content. The correlation between LCB and resulting $I_{3/1}$ and Φ_3 is confirmed by coupling

the non-linear rheological results with melt-state NMR and LAOS simulations using the DCPP model. Large values of the branching parameter q in this model are found to decrease the non-linearity plateau the inverse critical strain, B and the slope C, hence acting as "solvents" for the backbone. Furthermore, when the pom-pom molecule relaxes mainly by orientation and less by stretching (quantified via λ/λ_s) the parameter A decreases, however the non-linearities increase at lower γ_0 (larger B values) and with a larger slope (as given by C). Additionally results from measuring blends of linear and LCB industrial polyethylenes of similar molecular weight distribution reveal a monotonic dependence of the intensities and phases of the FT-spectrum on LCB sample content and prove the high sensitivity of FT-Rheology on small concentrations of branched species in a miscible homogeneous polyethylene melt, as low as 1-5 wt % of branched PE added in linear PE, while linear rheology can detect concentrations higher than 10-30 wt % for these materials. For the specific miscible linear/LCB PE blends, the non-linear parameters A, B and D are found to increase linearly with the concentration of the LCB PE component. An additional potential quantity to discriminate LCB and linear polyethylenes is the zero-shear extrapolated phase of the 3^{rd} harmonic, Φ_3^0. At the onset of non-linearity (at relatively low strain amplitudes) this particular relative phase can be measured reproducibly and is found to be significantly large for PE containing LCB than for linear PE. Finally, the optimum conditions for probing LCB in industrial polyethylene are investigated and are found to be T = 180 °C in combination with large strain amplitudes, i.e. γ_0 = 3 in a closed-cavity geometry with grooved surfaces to avoid slippage (e.g. RPA2000) and low excitation frequencies, typically $\omega_1/2\pi$ = 0.1 Hz.

A factor of great importance in polymer industry along with molecular architecture is the occurring flow instabilities during processing of commercial products and especially in industrial polyethylene. FT-Rheology is a useful robust tool to quantify the resulting stress response in LAOS flows including instabilities. Combining results from a rheometer sensitive at low strain amplitudes (ARES) and an apparatus where large deformations can be applied with suppressed slippage (RPA2000) one can derive the "mastercurve" for the $I_{3/1}$ and Φ_3 as a function of γ_0, for a specific excitation frequency and at constant temperature, which will correspond only to the material inherent non-linearity. When flow instabilities take place at an open-rim geometry, the resulting non-linearities depart significantly from the expected non-linear response of the material, which within this work is referred to as material inherent non-linearity. The relative intensity, $I_{3/1}(\gamma_0)$, shows a sudden change in slope departing from the predicted behaviour ($A(1 - \frac{1}{1-(B\gamma_0)^C})$), the phase $\Phi_3(\gamma_0)$ exhibits a local maximum and even harmonics appear, i.e. $I_{2/1}(\gamma_0)$ larger than the noise level being typically 0.2%. Typically for the critical strain $\gamma_{0,c}$, $I_{2/1} > 0.1$ %. This additional intensity of the odd higher harmonics, as well as the appearance of even harmonics and the change in corresponding relative phases, is attributed to the wall slip of the sample in the parallel plate flow configuration.

The onset of slip can be quantified and correlated with molecular weight and polymer topology. The non-linearities quantified via FT-Rheology can be significantly changed by a

surface modification of the plates. Using fluorocarbonated coating on steel plates, four times large values for $I_{2/1}$ and $I_{3/1}$ are found and the critical strain for slip onset is reduced to 3/4 of the value for steel plates. The non-linear rheological behaviour depends generally in all factors which influence the onset and development of flow instabilities, namely surface material type, geometry of flow domain (e.g. sample thickness, grooved surfaces) and deformation history. By using a sample of double thickness, or grooved surfaces in the ARES open-rim geometry, the intensities can increase up to an order of magnitude, thus indicating the occurrence of secondary flow and instabilities, such as meniscus distortions. The test or process temperature is another important factor [Hatzikiriakos 92a, Larson 92]. An increase in the temperature from 180 °C to 200 °C, $I_{3/1}$ for the case of PS can be reduced up to 1/3 of its value and the flow is stable for a wider range of deformations (increase of $\gamma_{0,critical}$). The highly non-linear and in some cases asymmetric stress signals are qualitatively predicted via finite element LAOS simulations with the DCPP model and the slip model which couples the slip velocity with the wall shear stress. Finally, the FT-Rheology results from LAOS flow can be correlated to sample behaviour during capillary extrusion. Thus, the combination of FT-Rheology combined with capillary rheometry can be used to predict extrudate distortions like sharkskin, stick-slip, gross fracture in polyethylene. The study of a specific set of industrial polyethylenes leads to the following conclusions. Low molecular weight polyethylenes exhibit less flow instabilities and especially by increasing the amount of incorporated SCB, a shift of instabilities onset at higher critical deformations, or even a suppression of stick-slip and generally of intense extrudate distortions, is observed. On the other hand, samples containing LCB and accordingly high values of $I_{3/1}$ during LAOS flow present instabilities at lower critical stresses and of higher pressure deviations, consequently higher extrudate surface distortion amplitudes.

As already pointed out that the normal forces and especially the first normal stress difference N_1 = T $_{xx}$ - T $_{yy}$ (or N_1 = T $_{11}$ - T $_{22}$ within chapters 2 and 5) can be considered to strongly affect the onset of slip and the occurring flow non-linearities. In LAOS flow this parameter can be used for differentiating topologies in the non-linear regime. Furthermore, the potential of the stress ratio, N_1/σ_{xy} [Larson 92], to be the critical parameter controlling the onset of flow instabilities is preliminary examined. Within this work, this is evaluated in numerical simulations for LAOS and capillary flows and the results reveal a correlation between the normal stresses and topological characterization, as well as flow instabilities.

Appendix

A Dimensionless numbers

The Reynolds number, Re describes the ratio of the kinetic energy, or inertia, to the energy lost due to viscous forces in a flow.

$$Re = \frac{dv\rho}{\eta} \tag{A.1}$$

where d is a characteristic distance for the flow, e.g. capillary diameter. The characteristic velocity for the fluid is v and ρ and η are the fluid density and the absolute dynamic viscosity, respectively. The Re can be defined for a couette flow [Tanner 00]:

$$Re = \frac{\rho\omega h^2}{\eta} \tag{A.2}$$

where ω is the excitation frequency of the moving cup, η is calculated from $\sigma_{xy}/\ \dot{\gamma}$ and h is the gap between the walls.

The Deborah number corresponds to the ratio of the characteristic relaxation time, e.g. τ of the material to the characteristic observation time of the flow process, e.g. T_0 [Owens 02]. For an oscillatory shear with an excitation frequency $\omega = 1/T_0$ it can be expressed as:

$$De = \frac{\tau}{T_0} = \tau\omega \tag{A.3}$$

The Deborah number is zero for a Newtonian fluid and infinite for an ideal Hookean elastic solid. However, in general the Deborah number associated with a material takes not a single value. If the characteristic time of the flow process is small, e.g. large ω in a oscillatory shear

rheometric flow, a material with a non-zero τ will behave in a solid-like way. Conversely, a material which appears solid, will behave fluid-like if the observation time is sufficiently increased.

An alternative definition used to provide a quantitative measure for the viscoelasticity of non-Newtonian fluids is the Weissenberg number, W_i (or W_s in literature). It is defined as:

$$W_i = \tau \frac{v}{h} \tag{A.4}$$

where v and h are the characteristic process velocity and process length [Nassehi 02]. It can be used to decide whether viscoelastic effects are significant in a certain flow problem or not.

B Tensor analysis

The tensor quantities and calculus relations used in the models presented within this work are presented here.
The gradient of a scalar $\phi(x, y, z)$ is defined as:

$$\nabla(\phi) \equiv \frac{\partial \phi}{\partial x}\mathbf{i} + \frac{\partial \phi}{\partial y}\mathbf{j} + \frac{\partial \phi}{\partial z}\mathbf{k} \tag{B.1}$$

where **i**, **j**, **k** are the unit vectors in a Cartesian coordinate system. The divergence of a vector **V(**x, y, z**)** is defined as:

$$\nabla \cdot \mathbf{V} = (\frac{\partial}{\partial x}\mathbf{i} + \frac{\partial}{\partial y}\mathbf{j} + \frac{\partial}{\partial z}\mathbf{k}) \cdot (V_1\mathbf{i} + V_2\mathbf{j} + V_3\mathbf{k}) = \frac{\partial V_1}{\partial x} + \frac{\partial V_2}{\partial y} + \frac{\partial V_3}{\partial z} \tag{B.2}$$

$\overset{\triangle}{\mathbf{T}}_{\mathbf{1}}$ is the lower-convected derivative of the viscoelastic extra stress, which is defined as follows:

$$\overset{\triangle}{\mathbf{T}} = \frac{D\mathbf{T}}{Dt} + \mathbf{T} \cdot \nabla \mathbf{v}^T + \nabla \mathbf{v} \cdot \mathbf{T} \tag{B.3}$$

$\overset{\nabla}{\mathbf{T}}$ is the upper-convected derivative of a tensor **T** defined as:

$$\overset{\nabla}{\mathbf{T}} = \frac{D\mathbf{T}}{Dt} - \mathbf{T} \cdot \nabla\mathbf{v} - \nabla\mathbf{v}^T \cdot \mathbf{T} \tag{B.4}$$

where **v** is the velocity vector and $\frac{D}{Dt}$ is the material time derivative:

$$\frac{D}{Dt} = \frac{\partial}{\partial t} + \mathbf{v} \cdot \nabla \tag{B.5}$$

C Maxwell model for oscillatory shear

The Maxwell model can be used as shown below. in order to describe an oscillatory shear flow. The applied sinusoidal shear strain, $\gamma(t) = \gamma_0 sin\omega t$ can be described by the following complex expression [Tanner 00]:

$$\begin{aligned} &\gamma(t) = \gamma_0 exp(i\omega t), \\ &\dot{\gamma} = \gamma_0(i\omega)exp(i\omega t) = i\omega\gamma(t) \end{aligned} \tag{C.1}$$

In the dynamic steady-state:

$$\begin{aligned} &\sigma(t) = \sigma_0 exp(i(\omega t + \delta)), \\ &\dot{\sigma} = \sigma_0(i\omega)exp(i(\omega t + \delta)) = i\omega\sigma(t) \end{aligned} \tag{C.2}$$

In the Maxwell model, the total shear rate is the sum of the shear rate of the elastic part (spring) and the shear rate of the viscous component (dash-pot):

$$\begin{aligned} &\dot{\gamma} = \frac{\dot{\sigma}}{G} + \frac{\sigma}{\eta} \Rightarrow i\omega\gamma(t) = \frac{i\omega\sigma(t)}{G} + \frac{\sigma}{\eta}, \\ &[i\omega\gamma(t)]\frac{G}{i\omega\sigma(t)} = [\frac{i\omega\sigma(t)}{G} + \frac{\sigma}{\eta}]\frac{G}{i\omega\sigma(t)}, \\ &\frac{G\gamma(t)}{\sigma(t)} = 1 + \frac{G}{i\omega\eta} \end{aligned} \tag{C.3}$$

where the ratio of strain to stress is defined as:

$$\frac{\gamma(t)}{\sigma(t)} = \frac{1}{G^*(\omega)} \tag{C.4}$$

and η/G is the relaxation time τ. Hence, eq. C.3 is expressed as follows:

$$\frac{G}{G^*(\omega)} = 1 + \frac{1}{i\omega\tau}, G^*(\omega) = G\frac{i\omega\tau}{1+i\omega\tau} \tag{C.5}$$

The resulting expression for the complex modulus is separated into a real and an imaginary part:

$$G^*(\omega) = G'(\omega) + iG''(\omega) = G(\frac{\omega^2\tau^2}{1+\omega^2\tau^2} + i\frac{\omega\tau}{1+\omega^2\tau^2}) \tag{C.6}$$

thus, from the above equations one can derive the expression for the storage and the loss modulus as a function of frequency:

$$\begin{aligned} G'(\omega) &= G\frac{\omega^2\tau^2}{1+\omega^2\tau^2} \\ G''(\omega) &= G\frac{\omega\tau}{1+\omega^2\tau^2} \end{aligned} \tag{C.7}$$

From the above equation one can easily observe that for low excitation frequencies ($\omega \to 0$), $G' \propto \omega^2$ and $G'' \propto \omega$.

D Calculation of plateau modulus, G_N^0

Below are presented different ways to derive the plateau modulus, G_N^0, from a measurement of $G'(\omega)$, $G''(\omega)$ and tan δ.

G_N^0 can be determined from the value of $G'(\omega)$ at the lower frequency where tan δ is minimum:

$$G_N^0 = [G']_{tan\delta \to minimum} \tag{D.1}$$

Another method is by integrating G'' in the flow transition region [Fetters 94].

$$G_N^0 = \frac{2}{\pi} \int_{-\infty}^{+\infty} G''_{FT}(\omega) dln\omega \tag{D.2}$$

E ^{13}C melt-state NMR spectrum and carbon site assignments

A schematic representation of a polyethylene chain with LCB is presented in fig. E.1, with the several carbon cites detected by ^{13}C. Below a typical NMR melt-state spectrum is shown with the peaks assigned to the specific carbons in the polyethylene branched chain.

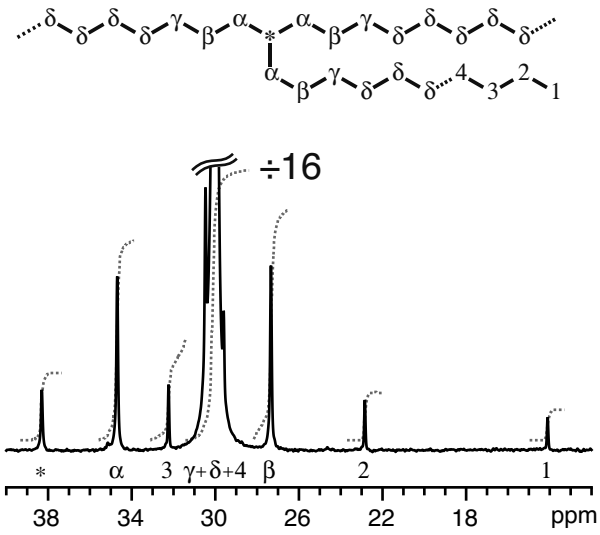

Figure E.1: *Typical melt-state ^{13}C NMR spectrum of a polyethylene containing branches of seven carbons in length or longer [Klimke 06].*

F Pom-pom model

The Pom-pom model is described below at its initial configuration [McLeish 98]. The approximation of the model to a differential form is additionally provided [Inkson 99] and the transformation to its DCPP formulation is given by Rutgers et al. [Rutgers 02], which is the formulation used in the present thesis. For a polymer molecule with a pom-pom topology (see fig. 2.4), M_b, M_a and q are the backbone molecular weight, the arms molecular weight and the number of arms attached to each backbone end, respectively. The dimensionless

partial molecular weights are defined as $s_a = M_a/M_e$ and $s_b = M_b/M_e$, where M_e is the entanglement molecular weight. The relaxation process of a pom-pom molecule cannot be fully described by the Doi-Edwards tube theory. This is due to the existence of branch points at the backbone ends, which act as topological constrains for the reptation of the backbone.

F.1 Branch point withdrawal

The resistance to the reptation of the backbone due to the branch points cannot be unlimited. The Doi-Edwards type tube, in which the backbone is reptating to relax, has a diameter a. Taking a linear chain into account, in order to maintain Gaussian chain statistics in equilibrium, a net Brownian force on every free chain end of magnitude kT/a would tend to maintain the curvilinear path of the chain segment within the tube. Hence, the pom-pom backbone may be stretched by the q free ends until it sustains a curvilinear tension of qkT/a. Beyond this tension, the free ends are withdrawn into the tube. The path length of an arm forced to adopt a configuration set by backbone orientation due to arm withdrawal is in units of tube diameter, s_c with $0 < s_c < M_a/M_e$.

F.2 Linear stress relaxation

The free arms in a pom-pom melt relax as if they were in a star polymer melt, except for one aspect, the backbones remain effective network parts throughout the relaxation process and exhibit a spectrum of relaxation times. The relaxation time spectrum for an arm, $\tau_a(x)$ is given by [Milner 97]:

$$\tau_a(x) = \tau_0 exp[\frac{15}{4} s_a \frac{(1-x)^2}{2} - (1-\phi_b)\frac{(1-x)^3}{3}] \tag{F.1}$$

where ϕ_b is the effectively fixed backbone material and x is a fraction of the tube segment from the branch point to the free end (retracted chain part). The constant τ_0 is an attempt time for deep retractions of the entangled dangling arm [McLeish 98]. The modulus has a quadratic dependence on concentration of oriented polymer segments and for these timescales [McLeish 98]:

$$G(t) = G_0(\phi_b + (1-\phi_b)\int_0^1 e^{-t/\tau_a(x)} dx)^2 \tag{F.2}$$

The effective friction for the reptation of the backbone with a curvilinear motion is found at the branch points. A branch point moved within the tube for a distance equal to the tube diameter, a after a time $\tau_a(0)$ has a diffusion constant $D_c = a^2/2\tau_a(0)$. Thus, using Einstein's equation and requiring that the drag on a branch point increases linearly with q, the branch point friction constant, ζ_b is given by:

$$\zeta_b = \frac{kT}{D_c} = 2kT\frac{\tau_a(0)}{a^2}q \tag{F.3}$$

The characteristic time for orientational relaxation of the backbone, τ_b, is the diffusion time of a one-dimensional walker with a diffusion constant, $D_c/2$, to move along a mean square distance of the dilated primitive path between the branch points, L^2. Assuming $M_e \propto 1/\phi_b$ (ϕ_b in this case is the concentration of entangled segments), the dilated tube diameter has an effective value $a_{eff} = a\phi_b^{-1/2}$ and $s_{b,eff} = s_b\phi_b$. Thus, $L^2 = s_{b,eff}^2 a_{eff}^2 = a^2\phi_b s_b^2$. Finally, the backbone relaxation time via orientation is given:

$$\tau_b = \frac{4}{\pi^2}s_b^2\phi_b\tau_a(0)q \tag{F.4}$$

By assigning a single relaxation time to the backbone material, the full relaxation modulus becomes:

$$G(t) = G_0(\phi_b e^{-t/\tau_b} + (1-\phi_b)\int_0^1 e^{-t/\tau_a(x)}dx)^2 \tag{F.5}$$

The stress is assumed to be calculated as a function of molecular orientation, and that in turn as in the tube-model theory [Doi 86], may be calculated by the orientation distribution of occupied tube segments, **u**. For linear polymers with known **u**, when are not stretched beyond equilibrium contour length of chain per tube segment, the stress tensor may be written:

$$\sigma = \frac{15}{4}G_0\langle\mathbf{uu}\rangle \tag{F.6}$$

Hence, a modified stress expression in terms of the high-frequency plateau modulus, arising from the backbone alone (the arms relax in a much faster timescale) is:

$$\sigma = \frac{15}{4} G_0 \phi_b^2 \langle \mathbf{uu} \rangle \tag{F.7}$$
$$\phi_b = \frac{s_b}{s_b + 2qs_a}$$

The factor ϕ_b is accounting for the number of elastically active segments and multiplied by another ϕ_b factor accounting for the dependence of the tube diameter, a, on concentration. Assuming that the orientation distribution is a weak function of position along the backbone, the unique measure of orientation also imposed upon the withdrawn material is the tensor **S** = $\langle \mathbf{uu} \rangle$. Finally, the stress can be expressed as:

$$\sigma = \frac{15}{4} G_0 \phi_b (\phi_b \Lambda^2(t) + \frac{2qs_c(t)}{2qs_a + s_b}) \mathbf{S}(\mathbf{t}) \tag{F.8}$$
$$\phi_b = \frac{s_b}{s_b + 2qs_a}$$

where Λ is the dimensionless stretch ratio of the backbone path length to its equilibrium length.

F.3 Dynamic equations

The orientation tensor **S** measures the distribution of the unit vectors describing the orientation of tube segments in the deforming melt. A dynamical system of evolution equations is used for **S**(t), Λ(t) and $s_c(t)$, which are used to construct the stress. For a flow with $s_c > 0$, the orientation characteristic time can be generalized as follows:

$$\tau_b = \frac{4}{\pi^2} s_b^2 \phi_b \tau_a(x_c(t)) q \tag{F.9}$$

where $x_c(t) = s_c/s_a$. Tube segments are created at a rate t_b^{-1} and afterwards extended during the flow. A segment created with orientation **u** at time t', has an orientation $\mathbf{E}(t,t') \cdot \mathbf{u}/|\mathbf{E}(t,t') \cdot \mathbf{u}|$ at time t, where $\mathbf{E}(t,t')$ is the local deformation gradient tensor between these times [McLeish 98]. Segments created at time t' with orientation **u** carry a relative weight of $|\mathbf{E}(t,t') \cdot \mathbf{u}|/\langle|\mathbf{E}(t,t') \cdot \mathbf{u}|\rangle$ in the distribution at time t, since a segment will increase in length and therefore in the amount of chain it carries by $|\mathbf{E}(t,t') \cdot \mathbf{u}|$. The surviving probability itself is the exponential of the time integral of destruction rates $\tau_b^{-1}(t'')$ in the interval $t' < t < t''$. The resulting expression for **S**(t) is then:

$$\mathbf{S}(t) = \int_{-\infty}^{t} \frac{dt'}{\tau_b(t')} exp(-\int_{t'}^{t} \frac{dt''}{\tau_b(t'')}) \frac{1}{\langle|\mathbf{E}(t,t')\cdot\mathbf{u}|\rangle} \langle \frac{\mathbf{E}(t,t')\cdot\mathbf{u}\mathbf{E}(t,t')\cdot\mathbf{u}}{|\mathbf{E}(t,t')\cdot\mathbf{u}|} \rangle \tag{F.10}$$

If we define the deformation rate tensor **K** such that $\partial\mathbf{E}(t,t')/\partial t$=**K.E**$(t,t')$ then the average increase in backbone length per unit length of tube is **K:S** and the relative curvilinear tube velocity is L**K.S**, where $L(t)$ is the curvilinear distance of separation between two branch points along the tube. By setting the frictional drag force from the relative velocity equal to the elastic force restoring L to its equilibrium length, we obtain:

$$\zeta_b(\mathbf{K}.\mathbf{S} - \frac{\partial L}{\partial t}) = \frac{kT}{s_b a^2}(L - s_b a) \tag{F.11}$$

for ζ_b in eq. F.3 and introducing Λ we obtain:

$$\frac{\partial \Lambda}{\partial t} = \Lambda(\mathbf{K} : \mathbf{S}) - \frac{1}{\tau_s}(\Lambda - 1) \tag{F.12}$$

where $\Lambda < q$.

The stretch relaxation timescale, τ_s, which appears only in non-linear deformations is given by:

$$\tau_s = s_b \tau_a(0) q \tag{F.13}$$

For the branch point withdrawal dynamic equation, we balance the drag and elastic tension and cancel the dimensional factors of the tube diameter obtaining the following for s_c:

$$\frac{\partial s_c}{\partial t} = (q\frac{s_b}{2} + s_c)\mathbf{K} : \mathbf{S} - \frac{1}{2\tau_a(s_c)} \tag{F.14}$$

For the above equation, Λ= q.

The eq. F.10, F.12 and F.14, with the expressions for the variable timescales, eq. F.9 and F.13, along with the equation for stress F.8 construct the simplified constitutive formulation for the pom-pom material [Inkson 99, McLeish 98].

F.4 Approximate differential model

For the evolution of a tensor of unit trace in a flow, we can have the following differential equation:

$$\frac{\partial \mathbf{S}(t)}{\partial t} = \mathbf{K}.\mathbf{S} + \mathbf{S}.\mathbf{K}^T - 2(\mathbf{S} : \mathbf{K})\mathbf{S} - \frac{1}{\tau_b}(\mathbf{S} - \frac{1}{3}\mathbf{I}) \tag{F.15}$$

In order to retain the simplicity of the above equation and obtain stable solutions, the calculation of **S**(t) is performed as:

$$\begin{aligned} \frac{\partial \mathbf{A}(t)}{\partial t} &= \mathbf{K} \cdot \mathbf{A} + \mathbf{A} \cdot \mathbf{K}^T - \frac{1}{\tau_b}(\mathbf{A} - \frac{1}{3}\mathbf{I}), \\ \mathbf{S}(t) &= \frac{\mathbf{A}(t)}{trace[\mathbf{A}(t)]} \end{aligned} \tag{F.16}$$

In a later paper for the Pom-pom model [Inkson 99] the evolution of **A**(t) is expressed as:

$$\frac{\partial \mathbf{A}(t)}{\partial t} + \mathbf{u} \cdot \nabla \mathbf{A} = \mathbf{K} \cdot \mathbf{A} + \mathbf{A} \cdot \mathbf{K}^T - \frac{1}{\tau_b}(\mathbf{A} - \mathbf{I}) \tag{F.17}$$

where $\mathbf{K} = \nabla \mathbf{u}$. The multi-mode model is introduced by adding the stress contribution of all n modes (from eq. F.8. Equation F.17 can be rewritten using the definition of the upper-convective derivative :

$$\overset{\nabla}{\mathbf{A}}_i\,(t) + \frac{1}{\tau_{bi}}(\mathbf{A}_i(t) - \mathbf{I}) = \mathbf{0} \tag{F.18}$$

where i is the number of each individual mode. A correction is introduced in the equation for the stretch [Rutgers 02], eq. F.12 which is given by:

$$\frac{D\Lambda_i(t)}{Dt} = \Lambda_i(t)(\nabla \mathbf{u} : \mathbf{S}_i(t)) - \frac{1}{\tau_{si}}(\Lambda_i(t) - 1)e^{\frac{2}{q_i}(\Lambda_i(t)-1)} \tag{F.19}$$

which is strictly for $\Lambda_i(t) < q$, otherwise $\Lambda_i(t) = q$. In this multi-mode version of the model the total stress is given by:

$$\sigma(t) = \sum_i 3G_i\Lambda_i^2(t)\mathbf{S}_i(t) \tag{F.20}$$

In the extended and the double-convected (DCPP) formulation, the relaxation time for orientation is denoted as λ and the stretching characteristic time, λ_s, refers to the above mention τ_b and τ_s, respectively. In order to introduce a non-vanishing second normal stress difference and derive a constitutive equation in terms of a viscoelastic extra-stress tensor, $\mathbf{T}$ a closure approximation is introduced [Clemeur 03]:

$$trace[\mathbf{A}(t)] = \Lambda^2 \tag{F.21}$$

The extended Pom-pom model (SXPP) can be written as follows:

$$\overset{\nabla}{\mathbf{T}} + \lambda(\mathbf{T})^{-1} \cdot \mathbf{T} = 2G\mathbf{D} \tag{F.22}$$

$$\lambda(\mathbf{T})^{-1} = \frac{1}{\lambda}[\frac{\alpha}{G}\mathbf{T} + f(\mathbf{T})^{-1}\mathbf{I} + G(f(\mathbf{T})^{-1} - 1)\mathbf{T}^{-1}] \tag{F.23}$$

$$\frac{1}{\lambda}f(\mathbf{T})^{-1} = \frac{2}{\lambda_s}e^{\frac{2}{q}(\Lambda_B - 1)}(1 - \frac{1}{\Lambda_B}) + \frac{1}{\lambda\Lambda_B^2}(1 - \frac{atrace(\mathbf{T}\cdot\mathbf{T}}{3G^2}) \tag{F.24}$$

$$\Lambda_B = \sqrt{}(1 + \frac{trace\mathbf{T}}{3G}) \tag{F.25}$$

where a is a "Giesekus-like" non-linear parameter. The above model is referred to as DXPP. To circumvent singularity problems that occur the model is further modified [Clemeur 03]. An additional parameter is introduced, ξ, which controls the ratio of the second to the first normal stress difference.

$$\mathbf{A} + \lambda[(1 - \frac{\xi}{2})\overset{\nabla}{\mathbf{A}} + \frac{\xi}{2}\overset{\triangle}{\mathbf{A}}] - \frac{\mathbf{I}}{3} = \mathbf{0} \tag{F.26}$$

Thus, the orientation equation in the DCPP formulation is given by:

$$\lambda[(1 - \frac{\xi}{2})\overset{\nabla}{\mathbf{S}} + \frac{\xi}{2}\overset{\triangle}{\mathbf{S}}] + \lambda(1 - \xi)[2\mathbf{D} : \mathbf{S}]\mathbf{S} + \frac{1}{\Lambda^2}[\mathbf{S} - \frac{\mathbf{I}}{3}] = \mathbf{0} \tag{F.27}$$

The unknowns $\mathbf{S}$ and Λ obey also the equation:

$$\lambda_s \frac{D\Lambda}{Dt} - \lambda_s(\mathbf{D} : \mathbf{S})\Lambda + (\Lambda - 1)e^{2(\Lambda-1)/q} = \mathbf{0} \tag{F.28}$$

Finally, the viscoelastic extra stress tensor in a single-mode DCPP (for a multi-mode the stress contributions are simply added) is given by the following equation:

$$\mathbf{T} = \frac{G}{1-\xi}(3\Lambda^2\mathbf{S} - \mathbf{I}) \tag{F.29}$$

Bibliography

[Achilleos 02] E. Achilleos, G. C. Georgiou, S. G. Hatzikiriakos. On numerical simulations of polymer extrusion instabilities. *App. Rheol.* **12**, 88–104 (2002).

[Allal 06] A. Allal, A. Lavernhe, B. Vergnes, G. Martin. Relationships between molecular structure and sharkskin defect for linear polymers. *J. Non-Newton. Fluid Mech.* **134**, 127–135 (2006).

[Baaijens 97] F. P. T. Baaijens, S. H. A. Selen, H. P. W. Baaijens, G. W. M. Peters, H. E. H. Meijer. Viscoelastic flow past a confined cylinder of a low density polyethylene melt. *J. Non-Newton. Fluid Mech.* **68**, 173–203 (1997).

[Barone 98] J. R. Barone, N. Plucktaveesak, S. Q. Wang. Interfacial molecular instability mechanism for sharkskin phenomenon in capillary extrusion of linear polyethylenes. *J. Rheol.* **42**, 813–832 (1998).

[Bartsch 74] H. J. Bartsch. Handbook of mathematical formulas. Academic Press New York, New York (1974).

[Bersted 85] B. H. Bersted. On the effects of very low long chain branching in rheological behaviour of polyethylene. *J. App. Polym. Sci.* **30**, 3751–3765 (1985).

[Bicerano 02] J. Bicerano. Prediction of polymer properties. Marcel Dekker Inc., New York (2002).

[Briedis 76] I. P. Briedis, L. A. Faitel'son. Rheology and molecular structure of a polyethylene melt. 3. Relaxation spectra and characteristic relaxation time. *Mekh. Polim.* **2**, 322–330 (1976).

[Carreau 97] P. J. Carreau, D. De Kee, R. P. Chhabra. Rheology of Polymeric Systems: Principle and Application. Hanser Publishers, Munich (1997).

[Chen 94] Y. L. Chen, R. G. Larson, S. S. Patel. On Shear fracture of polystyrene melts and solutions. *Rheol. Acta* **33**, 243–256 (1994).

[Cho 05] K. S. Cho, K. Hyn, K. H. Ahn, S. J. Lee. A geometrical interpretation of large amplitude oscillatory shear response. *J. Rheol.* **49**, 747–758 (2005).

[Clemeur 03] N. Clemeur, R. P. G. Rutgers, B. Debbaut. On the evaluation of some differential formulations for the pom-pom constitutive model. *Rheol. Acta* **42**, 217–231 (2003).

[Clemeur 04] N. Clemeur, R. P. G. Rutgers, B. Debbaut. Numerical simulation of abrupt contraction flows using the double convected pom-pom model. *J. Non-Newton. Fluid. Mech.* **117**, 193–209 (2004).

[Cox 58] W. P. Cox, E. H. Merz. Correlation of Dynamic and Steady Flow Viscosities. *J. Polym. Sci.* **28**, 619–622 (1958).

[Crochet 92] M. J. Crochet, B. Debbaut, R. Keunings, J. M. Marchal. POLYFLOW, a multipurpose finite element program for continuous polymer flows. Applications of CAE in extrusion and other continuous processes. Carl Hanser Verlag, München (1992).

[Daniels 01] D. R. Daniels, T. C. B. McLeish, B. J. Crosby, R. N. Young, C. M. Fernyhough. Molecular Rheology of Comb Polymer Melts. 1. Linear Viscoelastic Response. *Macromolecules* **34**, 7025–7033 (2001).

[Debbaut 02] B. Debbaut, H. Burhin. Large amplitude oscillatory shear and Fourier-transform rheology for a high-density polyethylene: Experiments and numerical simulation. *J. Rheol.* **46**, 1155–1176 (2002).

[deGennes 71] P. G. deGennes. Reptation of a polymer chain in the presence of fixed obstacles. *J. Chem. Phys.* **55**, 572–579 (1971).

[deGennes 85] P. G. deGennes. Wetting: statics and dynamics. *Rev. Modern Phys.* **57**, 827–863 (1985).

[Doi 78a] M. Doi, S. F. Edwards. Dynamics of concentrated polymer systems. 1. Brownian-motion in equilibrium state. *J. Chem. Soc., Faraday Transactions II* **74**, 1789–1801 (1978).

[Doi 78b] M. Doi, S. F. Edwards. Dynamics of concentrated polymer systems. 2. Molecular-motion under flow. *J. Chem. Soc., Faraday Transactions II* **74**, 1802–1817 (1978).

[Doi 78c] M. Doi, S. F. Edwards. Dynamics of concentrated polymer systems. 3. Constitutive equation. *J. Chem. Soc., Faraday Transactions II* **74**, 1818–1832 (1978).

[Doi 79] M. Doi, S. F. Edwards. Dynamics of concentrated polymer systems. 4. Rheological properties. *J. Chem. Soc., Faraday Transactions II* **75**, 38–54 (1979).

[Doi 86] M. Doi, S. F. Edwards. The theory of polymer dynamics. Oxford University Press, Oxford (1986).

[Dusschoten 01] D. van Dusschoten, M. Wilhelm. Increased torque transducer sensitivity via oversampling. *Rheol. Acta* **40**, 395–399 (2001).

[Ernst 90] R. R. Ernst, G. Bodenhausen, A. Wokaun. Principles of nuclear magnetic resonance in one and two dimensions. Clarendon Press, Oxford (1990).

[Fang 05] Y. Fang, P. J. Carreau, P. G. Lafleur. Thermal and rheological properties of mLLDPE/LDPE blends. *Polym. Eng. Sci.* **45**, 1254–1264 (2005).

[Fetters 94] L. J. Fetters, D. J. Lohse, D. Richter, T. A. Witten, A. Zirkel. Connection between polymer molecular weight, density, chain dimensions, and melt viscoelastic properties. *Macromolecules* **27**, 4639–4647 (1994).

[Fetters 99] L. J. Fetters, D. J. Lohse, S. T. Milner, W. W. Graessley. Packing length influence in linear polymer melts on the entanglement, critical and reptation molecular weights. *Macromolecules* **32**, 6847 (1999).

[Filipe 06] S. Filipe, A. Becker, M. Wilhelm. Optimized pressure detection and analysis of melt flow instabilities in polymer melts using capillary rheometry. *J. Rheol.* **50**, 1–30 (2006).

[Fleury 04] G. Fleury, G. Schlatter, R. Muller. Non linear rheology for long chain branching characterization, comparison of two methodologies: Fourier transform rheology and relaxation. *Rheol. Acta* **44**, 174–187 (2004).

[Gabriel 98] C. Gabriel, J. Kaschta, H. Münstedt. Influence of molecular structure on rheological properties of polyethylenes I. Creep recovery measurements in shear. *Rheol. Acta* **37**, 7–20 (1998).

[Gabriel 99] C. Gabriel, H. Münstedt. Creep recovery behaviour of metallocene linear low-density polyethylenes. *Rheol. Acta* **38**, 393–403 (1999).

[Gabriel 02] C. Gabriel, H. Münstedt. Analytical and rheological characterization of long-chain branched metallocene-catalyzed ethylene homopolymers. *Polymer* **43**, 6383–6390 (2002).

[Gahleitner 01] M. Gahleitner. Melt rheology of polyolefines. *Prog. Polym. Sci.* **26**, 895–944 (2001).

[Gamota 93] D. R. Gamota, A. S. Wineman, F. E. Filisko. Fourier transform analysis: Nonlinear dynamic response of an electrorheological material. *J. Rheol.* **37**, 919–933 (1993).

[Georgiou 94] G. C. Georgiou, M. J. Crochet. Time-dependent compressible extrudate-swell problem with slip at the wall. *J. Rheol.* **38**, 1745–1755 (1994).

[Giacomin 98] A. J. Giacomin, J. M. Dealy. Large amplitude oscillatory shear. In A. A. Collyer, D. W. Clegg (eds.), Rheological measurements. Chapman Hall, London (1998).

[Graessley 82] W. W. Graessley. Entangled linear, branched and network polymer systems-Molecular theories. *Adv. Polym. Sci.* **47**, 67–117 (1982).

[Graham 95] M. D. Graham. Wall slip and the nonlinear dynamics of large amplitude oscillatory shear flows. *J. Rheol.* **39**, 697–712 (1995).

[Graham 01] R. S. Graham, T. C. B. McLeish, O. G. Harlen. Using the pom-pom equations to analyze polymer melts in exponential shear. *J. Rheol.* **45**, 275–290 (2001).

[Griskey 95] R. Griskey. Polymer process engineering. Chapman and Hall, New York (1995).

[Gröhn 06] F. Gröhn, H. Frey, A. Kilbinger. Makromolekulare Chemie 2005. *Nachrichten aus der Chemie* **3**, 292–300 (2006).

[Hadjichristid 00] N. Hadjichristidis, H. Iatrou, S. Pispas, M. Pitsikalis. Anionic polymerization: High vacuum techniques. *J. Polym. Sci. Polym. Chem.* **38**, 3211–3234 (2000).

[Hameed 02] T. Hameed, I. A. Hussein. Rheological study of the influence of M_w and comonomer type on the miscibility of mLLDPE and LDPE blends. *Polymer* **43**, 6911–6929 (2002).

[Hamielec 96] A. E. Hamielec, J.P.B. Soares. Polymer reaction engineering-Metallocene catalysts. *Prog. Polym. Sci.* **21**, 651–706 (1996).

[Han 87] C. D. Han, J. Kim. Rheological technique for determining the order-disorder transition of block-copolymers. *J. Polym. Sci., Polym. Phys.* **25**, 1741–1764 (1987).

[Hatzikiriakos 91] S. G. Hatzikiriakos, J. M. Dealy. Wall slip of molten high density polyethylenes. I. Sliding plate rheometer studies. *J. Rheol.* **35**, 497–523 (1991).

[Hatzikiriakos 92a] S. G. Hatzikiriakos, J. M. Dealy. Role of slip and fracture in oscillating flow of HDPE in a capillary. *J. Rheol.* **36**, 845–884 (1992).

[Hatzikiriakos 92b] S. G. Hatzikiriakos, J. M. Dealy. Wall slip of molten high density polyethylenes. II. Capillary rheometer studies. *J. Rheol.* **36**, 703–740 (1992).

[Helfland 82] E. Helfland, D. S. Pearson. Calculation of the non-linear stress of polymers in oscillatory shear fields. *J. Polym. Sci. Polym. Phys.* **20**, 1249–1258 (1982).

[Henson 95] D. J. Henson, M. E. Mackay. Effect of gap on the viscosity of monodisperse polystyrene melts: Slip effects. *J. Rheol.* **39**, 359–373 (1995).

[Hilliou 04] L. Hilliou, D. van Dusschoten, M. Wilhelm. Increasing the force torque transducer sensitivity of an RPA2000 by a factor of 5-10 via advanced data acquisition. *Rubber. Chem. Technol.* **77**, 192–200 (2004).

[Höfl 06] S. Höfl. Einfluss von Topologie und Verscherung auf Dynamik und mechanische Parameter bei Homopolymeren. Johannes Gutenberg-Universtität Mainz (2006).

[Hussein 03] I. A. Hussein, T. Hameed, B. F. A. Sharkh, K. Mezghani. Miscibility of hexene-LLDPE and LDPE blends: Influence of branch content and composition distribution. *Polymer* **44**, 4665–4672 (2003).

[Hussein 04] I. A. Hussein, M. C. Williams. Rheological study of the influence of branch content on the miscibility of octene-mLLDPE and Zn-LLDPE in LDPE. *Polym. Eng. Sci.* **44**, 660–672 (2004).

[Hyun 02] K. Hyun, S. H. Kim, K. H. Ahn, S. J. Lee. Large amplitude oscillatory shear as a way to classify complex fluids. *J. Non-Newton. Fluid Mech.* **107**, 51–65 (2002).

[Inkson 99] N. J. Inkson, T. C. B. McLeish, O. G.Harlen, D. J. Groves. Predicting low density polyethylene melt rheology in elongational and shear flows with "pom-pom" constitutive equations. *J. Rheol.* **43**, 873–896 (1999).

[Janzen 99] J. Janzen, R. H. Colby. Diagnosing long chain branching in polyethylenes. *J. Mol. Struct.* **485**, 569–584 (1999).

[Kallus 01] S. Kallus, N. Willenbacher, S. Kirsch, D. Distler, T. Neidhöfer, M. Wilhelm, H.-W. Spiess. Characterization of polymer dispersion by Fourier transform rheology. *Rheol. Acta* **40**, 552–559 (2001).

[Kauppinen 01] J. Kauppinen, J. Partanen. Fourier Transforms in Spectroscopy. Wiley-VCH, Berlin (2001).

[Klein 05] C. Klein. Rheology and Fourier-Transform Rheology on water-based systems. Johannes Gutenberg-Universität Mainz (2005).

[Klimke 06] K. Klimke, M. Parkinson, C. Piel, W. Kaminsky, H. W. Spiess, M. Wilhelm. Optimized polyolefin branch quantification by melt-state ^{13}C NMR spectroscopy. *Macrom. Chem. Phys.* **207**, 382–395 (2006).

[Krieger 73] I. M. Krieger, T. F. Niu. A rheometer for oscillatory studies of nonlinear fluids. *Rheol. Acta* **12**, 567–571 (1973).

[Kulicke 79] W. M. Kulicke, H. E. Jeberien, H. Kiss, R. S. Porter. Visual observation of flow irregularities in polymer solutions at theta-conditions. *Rheol. Acta* **18**, 711–716 (1979).

[Kwag 00] H. Kwag, D. Rana, K. Cho, J. Rhee, T. Woo, B. H. Lee. Binary blends of metallocene polyethylene with conventional polyolefines: Rheological and morphological properties. *Polym. Eng. Sci.* **40**, 1672–1681 (2000).

[Larson 92] R. G. Larson. Instabilities in viscoelastic flows. *Rheol. Acta* **31**, 213–263 (1992).

[Larson 99] R. G. Larson. The structure and rheology of complex fluids. Oxford University Press, Inc., Oxford (1999).

[Laun 78] H. M. Laun, H. Münstedt. Elongational behaviour of a low density polyethylene melt. *Rheol. Acta* **17**, 415–425 (1978).

[Laun 82] H. M. Laun. Elastic properties of polyethylene melts at high shear rates with respect to extrusion. *Rheol. Acta* **21**, 464–469 (1982).

[Laun 83] H. M. Laun. Polymer melt rheology with a slit die. *Rheol. Acta* **22**, 171–185 (1983).

[Laun 04] H. M. Laun. Capillary rheometry for polymer melts revisited. *Rheol. Acta* **43**, 509–528 (2004).

[Leblanc 03] J. L. Leblanc. Fourier transform rheology on gum elastomers. *J. App. Polym. Sci.* **89**, 1101–1115 (2003).

[Lim 89] F. J. Lim, W. R. Schowalter. Wall slip of narrow molecular weight distribution polybutadienes. *J. Rheol.* **33**, 1359–1382 (1989).

[Liu 00] S. Liu, A. Sen. Synthesis of syndiotactic-polystyrene-graft-poly(methyl methacrylate), syndiotactic-polystyrene-graft-poly(methyl acrylate) and syndiotactic-polystyrene-graft-atactic-polystyrene with defined structures by atom transfer radical polymerization. *Macromolecules* **33**, 5106–5110 (2000).

[Lohse 02] D. J. Lohse, S. T. Milner, L. J. Fetters, M. Xenidou, N. Hadjichristidis, R. A. Mendelson, C. A. Garca-Franco, M. K. Lyon. Well-defined, model long chain branched polyethylene. 2. Melt rheological behaviour. *Macromolecules* **35**, 3066–3075 (2002).

[Macosko 94] C. W. Macosko. Rheology, principles, measurements, and applications. Wiley-VCH, Inc., New York (1994).

[Malmberg 02] A. Malmberg, C. Gabriel, T. Stefl, H. Münstedt, B. Löfgren. Long-chain branching in metallocene-catalyzed polyethylenes investigated by low oscillatory shear and uniaxial extensional rheometry. *Macromolecules* **35**, 1038–1048 (2002).

[Marrucci 93] G. Marrucci, F. Greco. Flow behavior of liquid crystalline polymers. *Adv. Chem. Phys.* **86**, 331–404 (1993).

[Marrucci 94] G. Marrucci. Non-linearities in polymer rheology. *J. Phys. Condens. Matter* **6**, A305–A309 (1994).

[Mavridis 92] H. Mavridis, R. N. Schroff. Temperature dependence of polyolefin melt rheology. *Polym. Eng. Sci.* **32**, 1778–1791 (1992).

[McLeish 97] T. C. B. McLeish. Polymer architecture influence on rheology. *Curr. Op. Solid State Mater. Sci.* **2**, 678–682 (1997).

[McLeish 98] T. C. B. McLeish, R. G. Larson. Molecular constitutive equations for a class of branched polymers: The pom-pom polymer. *J. Rheol.* **42**, 81–110 (1998).

[Milner 97] S. T. Milner, T. C. B. McLeish. Parameter-free theory for stress relaxation in star polymer melts. *Macromolecules* **30**, 2159–2166 (1997).

[Mooney 31] M. J. Mooney. Explicit formulas for slip and fluidity. *J. Rheol.* **2**, 210–222 (1931).

[Morawetz 85] H. Morawetz. Polymers, the origin and growth of a science. Courier Dover Pub., New York (1985).

[Münstedt 81] H. Münstedt, H. M. Laun. Elongational properties and molecular structure of polyethylene melts. *Rheol. Acta* **17**, 415–425 (1981).

[Münstedt 98] H. Münstedt, S. Kurzbeck, L. Egersdörfer. Influence of molecular structure on rheological properties of polyethylenes. Part II: Elongational behaviour. *Rheol. Acta* **37**, 21–29 (1998).

[Nassehi 02] V. Nassehi. Practical Aspects of Finite Element Modelling of Polymer Processing. Wiley & Sons, West Sassex (2002).

[Natta 60] G. Natta. Stereospecific polymerizations. *J. Polym. Sci.* **48**, 219–239 (1960).

[Neidhöfer 01] T. Neidhöfer, M. Wilhelm, H. W. Spiess. Fourier-transform rheology on linear polystyrene melts. *Appl. Rheol.* **11**, 126–133 (2001).

[Neidhöfer 03a] T. Neidhöfer. Fourier-transform rheology on anionically synthesised polymer melts and solutions of various topology. Johannes Gutenberg-Universität Mainz (2003).

[Neidhöfer 03b] T. Neidhöfer, M. Wilhelm, B. Debbaut. Fourier-transform rheology experiments and finite-element simulations on linear polystyrene solutions. *J. Rheol.* **47**, 1351–1371 (2003).

[Neidhöfer 04] T. Neidhöfer, S. Sioula, N. Hadjichristidis, M. Wilhelm. Distinguishing linear from star-branched polystyrene solutions with Fourier-transform rheology. *Macromol. Rapid Commun.* **25**, 1921–1926 (2004).

[Owens 02] R.G. Owens, T.N. Phillips. Computational rheology. Imperial college press, London (2002).

[Peacock 00] A. J. Peacock. Handbook of polyethylene. Structures, properties and applications. Marcel Dekker, New York (2000).

[Pearson 68] J. R. A. Pearson, C. J. S. Petrie. On melt flow instability of extrudated polymers. In R. E. Wetton, R. H. Whorlow (eds.), Polymer systems: Deformation and flow, pp. 163–187. Macmillian, London (1968).

[Pearson 82] D. S. Pearson, W. E. Rochefort. Behaviour of concentrated polystyrene solutions in large amplitude oscillatory shear fields. *J. Polym. Sci.* **20**, 83–98 (1982).

[Pérez 05] R. Pérez, E. Rojo, M. Fernadez, V. Leal, P. Lafuente, A. Santamaria. Basic and applied rheology of mLLDPE/LDPE blends: Miscibility and processing features. *Polymer* **46**, 8045–8053 (2005).

[Pino 80] P. Pino, R. Mühlhaupt. Stereospecific polymerization of propylene: An outlook 25 years after its discovery. *Angew. Chem. Inter.* **19**, 857–875 (1980).

[Pollard 04] M. Pollard, K. Klimke, R. Graf, H. W. Spiess, M. Wilhelm, O. Sperber, C. Piel, W. Kaminsky. Observation of chain branching in polyethylene in the solid state and melt via ^{13}C NMR spectroscopy and melt NMR relaxation time measurements. *Macromolecules* **37**, 813–825 (2004).

[Polyflow 03] Benelux Polyflow. POLYFLOW User Guide. Fluent Inc., Lebanon, NH (2003).

[Ramirez 85] R. W. Ramirez. The FFT fundamentals and concepts. PH PTR, Enlewood Cliffs, New Jersey (1985).

[Read 01] D. J. Read, T. C. B. McLeish. Molecular rheology and statistics of long-chain branched metallocene-catalyzed polyolefines. *Macromolecules* **34**, 1928–1945 (2001).

[Reimers 98] M. J. Reimers, J. M. Dealy. Sliding plate rheometer studies of concentrated polystyrene solutions: Non-linear viscoelasticity and wall slip of two high molecular weight polymers in tricresyl phosphate. *J. Rheol.* **42**, 527–548 (1998).

[Roovers 79a] J. Roovers. Melt rheology of model branched polystyrenes. *Polym. Prepr. (Am. Chem. Soc., Div. Polym. Chem.)* **20**, 144–148 (1979).

[Roovers 79b] J. Roovers. Synthesis and dilute characterization of comb polystyrenes. *Polymer* **20**, 843–849 (1979).

[Roovers 81] J. Roovers, W. W. Graessley. Melt rheology of some model comb polystyrenes. *Macromolecules* **14**, 766–773 (1981).

[Roovers 87] J. Roovers, P. M. Poporowski. Relaxation by constraint release in combs and star-combs. *Macromolecules* **20**, 2300–2306 (1987).

[Rubinstein 03] M. Rubinstein, R. H. Colby. Polymer physics. Oxford University Press, New York (2003).

[Rutgers 00] R. P. G. Rutgers, M. R. Mackley. The correlation of experimental extrusion surface instabilities with numerically predicted exit surface stress concentrations and melt strength for linear low density polyethylene. *J. Rheol.* **44**, 1319–1334 (2000).

[Rutgers 01] R. P. G. Rutgers, M. R. Mackley. The effect of channel geometry and boundary conditions on the formation of extrusion surface instabilities for LLDPE. *J. Non-Newton. Fluid Mech.* **98**, 185–199 (2001).

[Rutgers 02] R. P. G. Rutgers, N. Clemeur, S. Muke, B. Debbaut. Polyethylene flow prediction with a differential multi-mode pom-pom model. *Korea-Australia Rheology Journal* **14**, 25–32 (2002).

[Schlatter 05] G. Schlatter, G. Fleury, R. Muller. Fourier transform rheology of branched polyethylene: experiments and models for assessing the macromolecular architecture. *Macromolecules* **38**, 6492–6503 (2005).

[Schmidt-Rohr 94] K. Schmidt-Rohr, H. W. Spiess. Multi-dimensional solid-state NMR and polymers. Academic press, London (1994).

[Schulze 05] D. Schulze, T. Roths, C. Friedrich. Classification of model topologies using the δ versus G^* plot. *Rheol. Acta* **44**, 485–494 (2005).

[Seitz 93] J. T. Seitz. The estimation of mechanical properties of polymers from molecular structure. *J. App. Polym. Sci.* **49**, 1331–1351 (1993).

[Skoog 96] D. A. Skoog, J. J. Leary. Principles of instrumental analysis. Saunders College Publications, New York (1996).

[Sperling 92] L. H. Sperling. Introduction to physical polymer science. Wiley-Interscience, New York (1992).

[Stadler 05] F. J. Stadler, C. Piel, K. Klimke, J. Kaschta, M. Parkinson, M. Wilhelm, W. Kaminsky, H. Münstedt. Influence of type and content of very long comonomers on long-chain branching of ethane-/α-olefine copolymers. *Macromolecules* (2005).

[Stange 05] J. Stange, C. Uhl, H. Münstedt. Rheological behaviour of blends from a linear and a long chain branched polypropylene. *J. Rheol.* **49**, 1059–1079 (2005).

[Strunglinski 88] M. J. Strunglinski, W. W. Graessley, L.J. Fetters. Effects of polydispersity on the linear viscoelastic properties of entangled polymers. 3. Experimental observations on binary mixtures of linear and star polybutadienes. *Macromolecules* **21**, 783–789 (1988).

[Tanner 00] R. I. Tanner. Engineering Rheology. Oxford University Press, Inc., Oxford (2000).

[Thompson 87] J. M. T. Thompson, H. B. Stewart. Nonlinear dynamics and chaos. Wiley, New York (1987).

[Trinkle 01] S. Trinkle, C. Friedrich. Van Gurp-Palmen Plot: a way to characterize polydispersity of linear polymers. *Rheol. Acta* **40**, 322–328 (2001).

[Trinkle 02] S. Trinkle, P. Walter, C. Friedrich. VanGurp-Palmen-plot II - classification of long chain branched polymers by their topology. *Rheol. Acta* **41**, 103–113 (2002).

[Vega 98] J. F. Vega, A. Santamaria, A. Munoz-Escalona, P. Lafuente. Small amplitude oscillatory shear flow measurements as a tool to detect very low amounts of long-chain branching in polyethylene. *Macromolecules* **31**, 3639–3647 (1998).

[Vega 99] J. F. Vega, A. Santamaria, A. Munoz-Escalona, P. Lafuente. Rheological criteria to characterize metallocene catalyzed polyethylenes. *Macromol. Chem. Phys.* **200**, 2257–2268 (1999).

[Verbeeten 04] W. M. H. Verbeeten, G. W. M. Peters, F. P. T. Baajens. Numerical simulations of the planar contraction flow for a polymer melt using the XPP model. *J. Non-Newton. Fluid Mech.* **117**, 73–84 (2004).

[Vittorias 06] I. Vittorias, M. Parkinson, K. Klimke, B. Debbaut, M. Wilhelm. Detection and quantification of polyethylene branching topologies via Fourier-transform rheology, NMR, and finite element simulation, using the pom-pom model. *Rheol. Acta* (2006). Online.

[Wang 96a] S. Q. Wang, P. A. Drda. Stick-slip transition in capillary flow of polyethylene. 2. A molecular weight dependence and low-temperature anomaly. *Macromolecules* **29**, 4115–4119 (1996).

[Wang 96b] S. Q. Wang, P. A. Drda, Y. W. Inn. Exploring molecular origins of sharkskin, partial slip and slope change in flow curves of linear low-density polyethylene. *J. Rheol.* **40**, 875–898 (1996).

[Ward 04] I. M. Ward, J. Sweeney. An introduction to the mechanical properties of solid polymers. Wiley, West Sussex (2004).

[White 91] J. L. White, M. H. Han, N. Nakajima, R. Brzoskowski. The influence of materials of construction on biconical rotor and capillary measurements of shear viscosity of rubber and its compounds and consideration of slippage. *J. Rheol.* **35**, 167–189 (1991).

[Wilhelm 98] M. Wilhelm, D. Maring, H. W. Spiess. Fourier-transform rheology. *Rheol. Acta* **37**, 399–405 (1998).

[Wilhelm 99] M. Wilhelm, P. Reinheimer, M. Ortseifer. High sensitivity Fourier-transform rheology. *Rheol. Acta* **38**, 349–356 (1999).

[Wilhelm 00] M. Wilhelm, P. Reinheimer, M. Ortseifer, T. Neidhöfer, H. W. Spiess. The crossover between linear and non-linear mechanical behaviour in polymer solutions as detected by Fourier-transform rheology. *Rheol. Acta* **39**, 241–246 (2000).

[Wilhelm 02] M. Wilhelm. Fourier-Transform Rheology. *Macromol. Mater. Eng.* **287**, 83–105 (2002).

[Williams 55] M. L. Williams, R. F. Landel, J. D. Ferry. The temperature dependence of relaxation mechanisms in amorphous polymers and other glass-forming liquids. *J. Am. Chem. Soc.* **77**, 3701–3707 (1855).

[Wood-Adams 00] P. M. Wood-Adams, J. M. Dealy. Using rheological data to determine the branching level in metallocene polyethylenes). *Macromolecules* **33**, 7481–7488 (2000).

[Xu 01] J. Xu, X. Xu, L. Chen, L. Feng, W. Chen. Effect of composition distribution on miscibility and co-crystallization phenomena in the blends of low density polyethylene with conventional and metallocene-based ethylene-butene copolymers. *Polymer* **42**, 3867–3874 (2001).

[Yamaguchi 99] M. Yamaguchi, S. Abe. LLDPE/LDPE blends. I. Rheological, thermal and mechanical properties. *J. App. Polym. Sci.* **74**, 3153–3159 (1999).

[Yan 99] D. Yan, W.-J. Wang, S. Zhu. Effect of long-chain branching on rheological properties of metallocene polyethylene. *Polymer* **40**, 1737–1744 (1999).

[Yoshimura 87] A. S. Yoshimura, R. K. Prud'homme. Response of an elastic Bingham fluid to oscillatory shear. *Rheol. Acta* **26**, 428–436 (1987).

[Young 91] R. J. Young. Introduction to Polymers. Chapman and Hall, London (1991).

[Zachmann 94] H. G. Zachmann. Mathematik für Chemiker. VCH, Weinheim (1994).

[Ziegler 55] K. Ziegler, E. Holzkamp, H. Breil, H. Martin. The Mühlheim low-pressure polyethylene process. *Angew. Chem. Internat. Ed.* **67**, 541–547 (1955).

Acknowledgments

I would like to thank:

- Prof. M. Wilhelm for the chance he gave me to work for my Ph.D. at the MPI-P, the direct supervision of my work all these years, the guidelines and helpful comments always kindly provided and the whole fruitful and friendly cooperation. I am also grateful to him, for providing the opportunity and organising my visit in MacDiarmid Institute, in Wellington New Zealand.
- Prof. H. W. Spiess for accepting me in his group and contributing to my work with his helpful and always valuable suggestions.
- Prof. P. Callaghan for giving me the opportunity to work in his group at MacDiarmid Institute in Wellington New Zealand and for his helpful comments and suggestions.
- Prof. H. Münstedt, F. Stadler, Dr. D. Auhl, and J. Kaschta from the Institute of Polymer Materials, Friedrich-Alexander-University of Erlangen-Nurmberg, Erlangen, Germany, for supplying with polyethylene samples, associated analytical data and for fruitful discussions.
- Dr. Debbaut for sharing his valuable experience in the field of viscoelastic flow simulations and C. Gomez, both from Polyflow s.a./Fluent Benelux, for continuous support and assistance with anything concerning the simulation part of the thesis.
- Dr. C. Lamotte and Dr. J. Michel from TOTAL, Feluy Belgium, for providing with polyethylene samples and corresponding analytical data.
- Dr. K. Knoll from BASF AG, Ludwigshafen Germany, for kindly providing us with several polystyrene samples.
- T. Wagner and J. Thiel from MPI-P for providing me with polystyrene samples.
- Dr. V. Maus and M. Drechsler from MPI-P, for providing polystyrene samples and blends, as well as demanded analytical measurements, anytime and for any sample. Additionally, the help of S. Seywald from Polymeranalytik group in MPIP with the GPC measurements on all studied materials is deeply acknowledged.
- Dr. R. Wäber, G. Vulpius and H. Dörr for preparing the polyethylene blends at the Deutsches Kunstoff Institut, Darmstadt, Germany.

- The whole group of Prof. Spiess, for the friendly atmosphere during my three years in MPIP, the nice cooperation and the help, always provided to me whenever I needed it.
- Especially the FT-Rheology group: Dr. V. Barroso, A. Becker, Dr. S. Filipe, Dr. S. Höfl, Dr. K. Hyun, Dr. C. Klein, Dr. K. Klimke, Dr. P. Minkin, R. Musampa, Dr. T. Neidhöfer, Dr. C. Oelschlaeger and Dr. M. Parkinson, for introducing me to the mysteries of polymers and FT-Rheology, the wonderful cooperation all these years, the kind knowledge exchange and generally the warm group working atmosphere in the office and for being the best lab partners. From these people, I am especially tankful to Dr. S. Höfl for helping me integrate in Germany (secretarial-bureaucratic duties undertaken), for providing with experimental results for the PS combs and correcting my thesis and any manuscript I wrote during the last years. Furthermore, I am grateful to Dr. S. Filipe for the capillary measurements on my polyethylene samples and the promising fruitful cooperation. Special thanks also to Dr. M. Parkinson and Dr. K. Klimke for the NMR measurements on the polyethylenes, the helpful suggestions and their valuable corrections on my manuscripts. To all my colleagues, special thanks for tolerating my comments and annoying jokes all this time (like football related photos, comments and videos to my Portuguese and French friends).
- I. Naue and K. Riazi, students at the TU Darmstadt, for keeping up with me as their supervisor during their practice in MPIP. Their measurements were extremely valuable to the well-timed completion of the present thesis (although Ingo never learnt to make me a decent coffee!!).
- The group of Prof. Callaghan in Wellington New Zealand, especially my office and lab colleagues: B. Douglas, S. Rogers, A. Lutti, Dr. M. Hunter, Dr. P. Hubbard, Dr. P. Galvosas and Dr. R. Lopez, for helping me integrate in the institute and also getting to know the life “down under”.
- My family for their continuous support all these years in any possible way. Without them I wouldn’t have achieved anything.
- My Ewa for being my partner in every aspect of my life. For helping me with small arrangements at work up to checking my manuscript and from psychologically supporting me up to tolerating my temper the last years. Above all, for giving me the best and most important of all, my son.

CV

Personal

Iakovos Vittorias

born in 13. September 1980 in Rhodos, Greece

School education

Elementary school in Rhodos, Greece

Gymnasium in Rhodos, Greece

1995-1998	Lyceum in Rhodos, Greece

Studies

10.1998-07.2003	Diploma in Chemical engineering, Engineering school, Aristotle University in Thessaloniki, Greece
10.2002-07.2003	Diploma thesis in Chemical engineering, Engineering school, Aristotle University in Thessaloniki, in group of Prof. K. Kiparissides, LPRE Institute (Thesis title: Dynamic simulation of styrene polymerization)

Postgraduate studies

Since 11.2003	Ph.D. studies in Max-Planck Institute for Polymer Research in Mainz, Germany, in the group of Prof. Spiess and in Mechanical Engineering department, TU Darmstadt, Germany, in the group of Prof. M. Wilhelm.
11.2003-10.2005	Marie Curie research fellow in Max-Planck Institute for Polymer Research in Mainz, Germany.
05.2004-07.2004	Visiting scientist in MacDiarmid Institute for Advanced Materials and Nanotechnology in Wellington, New Zealand, in the group of Prof. P. Callaghan.

Occupation

Since 11.2004	Scientific staff in Max-Planck Institute for Polymer Research in Mainz, Germany.
07.2002-08.2002	Practice in BASF AG in Ludwigshafen, Germany, Polymer Reaction Engineering department.